Distribution Agreement

Signature:

______________________________ _______________
Michael J. Reddish Date

Role of Loop Motions in Enzyme Catalysis

By

Michael J. Reddish

Doctor of Philosophy

Chemistry

R. Brian Dyer

Advisor

Vincent Conticello

Committee Member

Tim Lian

Committee Member

Accepted:

Lisa A. Tedesco, Ph.D.

Dean of the James T. Laney School of Graduate Studies

Date

Role of Loop Motions in Enzyme Catalysis

By

Michael J. Reddish

B.S., Furman University, 2009

Advisor: R. Brian Dyer, PhD

An abstract of

A dissertation submitted to the Faculty

of the James T. Laney School of Graduate Studies of Emory University

in partial fulfillment of the requirements for the degree of

Doctor of Philosophy

in Chemistry

2015

Abstract

Role of Loop Motions in Enzyme Catalysis

By Michael J. Reddish

Enzymes are important paradigms for studying catalysis. They are highly effective at increasing reaction rates with strong substrate specificity while operating at moderate conditions. Despite extensive characterization over the last century, the actual process of enzyme catalysis is not well understood. Simple investigations relating protein structure to function fail. These investigations tend to fail because they consider the enzyme as a static structure, ignoring the fact that proteins are known to exist as dynamic structures. Protein dynamics can occur on the order of small vibrations or large conformational rearrangements. One such dynamic feature common to many enzymes is the movement of loops throughout the catalytic cycle. Loop motion has typically been ill-studied due to experimental limitations in studying the microsecond to millisecond timescale of these motions. In this dissertation, we develop two complimentary approaches to studying this timescale, temperature-jump spectroscopy and microfluidic fast-mixing. We then apply these methods to study three different model enzyme systems: lactate dehydrogenase, dihydrofolate reductase, and purine nucleoside phosphorylase. By studying these enzymes we are able to establish that loop motions contribute a significant amount of heterogeneity to enzyme reactions requiring a reaction landscape, as opposed to the traditional reaction pathway, to fully describe the system. We then briefly discuss the implications of this approach for understanding enzymes in general.

Role of Loop Motions in Enzyme Catalysis

By

Michael J. Reddish

B.S., Furman University, 2009

Advisor: R. Brian Dyer, PhD

A dissertation submitted to the Faculty
of the James T. Laney School of Graduate Studies of Emory University
in partial fulfillment of the requirements for the degree of
Doctor of Philosophy
in Chemistry
2015

Acknowledgements

To Sarah, who supported and sustained me throughout this entire process.

To Caitlin and Drew, who kept me sane when the lab attempted otherwise.

To Brian Dyer, who taught me more about the nature of science and research than I thought possible in graduate school.

Contents

Figures

Tables

Chapter 1. Introduction to Enzyme Catalysis

Enzymes are a class of biological molecules that act as catalysts. Like all catalysts, enzymes' function is to increase the rate of a chemical reaction. Unlike many synthetic catalysts that operate in extreme environments, such as very high or low pH, high temperatures, and high concentrations, most enzymes must operate in the biologically relevant environment of neutral pH with moderate temperature and concentration. These moderate conditions do not favor reaction rate enhancement and therefore make the dramatic increases in rates that enzymes achieve all the more impressive. It has previously been estimated that, depending on the enzyme, catalytic rate enhancement is 10^7-10^{19} times faster with the enzyme than the corresponding uncatalyzed reaction in water.[1] This range of enhancement is due to the fact that there is a range of rates for the corresponding reactions in water and because not all enzymes are optimized for rate enhancement.[1-2] While some enzymes are so optimized that they operate at or near the limit of substrate diffusion to the enzyme ($k_{cat}/K_m \geq 10^8$),[3-4] the common enzyme catalytic rate has been estimated to be around 1000 s^{-1}.[1] Even still, the common enzyme rate is impressive in moderate conditions compared to most synthetic catalysts; therefore, enzymes serve as a sort of catalytic standard or goal for synthetic catalysts. The optimization of designed or synthetic catalysts has many important applications. Novel catalysts are required for the cost-effective synthesis of natural compounds[5], to improve the efficiency and specificity of industrial reactions[6], and to design methods for disposal of xenobiotic compounds[7] among other applications. Despite extensive characterization of several enzymes, there does not exist a molecular understanding of how enzymes function, especially with regard to the role of dynamics.

One example that demonstrates the limits of our understanding of enzyme design is the effort to produce a non-natural *de novo* enzyme. The idea is simple. Scientists have learned a lot about protein structure and its relationship to catalytic mechanisms, so if we really understand the relationship, we should be able to design an enzyme to perform a particular function. This has been attempted for several common organic reactions including a Kemp elimination, a retro-aldol reaction, and a Diels-Alder reaction.[8-10] The attempts to generate and maximize a Diels-Alderase represent the progress in this field well. In some ways the initial work on this problem was very successful. Siegel and coworkers were able to computationally design an enzyme that could perform their desired Diels-Alder reaction and did so with high selectivity for the desired stereoisomer, >97% selective versus 47% selective in the uncatalyzed reaction.[10] However, the process was anything but straightforward. Of the approximately 10^6 designed active sites that could fit into a protein backbone, only 2 of the 50 most promising candidates showed measurable activity. Furthermore, the k_{cat} of the best of these two enzymes was 2.13 hr^{-1} with a catalytic efficiency (k_{cat}/K_M) of 0.455 s^{-1} M^{-1}.[10] Even with refinement from human-assisted backbone refinement[11] and directed evolution[12] approaches the enzyme was only able to be enhanced to a k_{cat} of 10.8 hr^{-1} with a catalytic efficiency of 103 s^{-1} M^{-1}.[12] These numbers pale in comparison to those of even modest natural enzymes.[2]

So, what are we missing? The *de novo* design researchers used the most up-to-date structural algorithms to design their enzymes. In the most recent of these publications, the authors provide insight into the missing parameter: protein backbone dynamics.[12] Calculations estimating the interactions between enzymes and their substrates assume a fixed and rigid peptide backbone; these calculations do not take into consideration that proteins are known to be dynamic molecules with motions on a wide array of timescales that can affect the catalytic mechanism. Therefore, any complete model of enzyme catalysis must include both static and dynamic structural elements. The work described herein is focused on these dynamic components, but first the variety of current models used to explain enzyme function will be discussed.

Different models exist to describe the various components of the enzyme catalytic cycle. The most important of these models is rate theory. Rate theory applied to chemical reactions describes the time-dependent interconversion of various chemical states through chemical reactions.[13] This theory is associated with the early work of Arrhenius[14] and van’t Hoff[15] who described the relationship between temperature and reaction rate as shown in equation (1.1).

$$Rate \propto e^{-A/T} \tag{1.1}$$

Where T is the absolute temperature and A is some sort of “activated” state that must be achieved prior to the reaction occurring. The energy of this activated state determines the effect of temperature on reaction rate. While an exact definition of the activated state was unclear early in development, chemists have generally accepted the activated state as describing the energy of a high-energy transiently populated reaction state that separates reactant-like states from product-like states. This is known as the transition state, and its application to understanding reaction rates is called transition state theory. The work of Pelzer, Wigner, and Eyring was fundamental in the development of this description.[16-19] Mathematically, the exponential term in equation (1.1) ranges from 0-1 and acts like a scaling factor for a maximal rate determined by concentration of the reactant molecules present and the number of approaches to the reaction barrier. Number of approaches to the reaction barrier can be understood as collisions between reactants or as the likelihood of reaction-active states to be populated.[13, 20] The concentration-independent terms are normally summarized into a temperature-dependent rate constant (*k*) for a given reaction in the so-called Arrhenius equation. This expression is given in its molecular form by equation (1.2) where R is the ideal gas constant, E_a is the energy of the transition-state or activated-state, T is the absolute temperature, and A (Arrhenius prefactor) is the rate of approaches to the reaction barrier.

$$k = Ae^{-E_a/RT} \tag{1.2}$$

As noted above, enzymes function by increasing the rate of a specified reaction. Since enzymes do not increase the physiologically relevant reactant concentrations, according to transition state theory they must be acting by increasing the rate constant for a given reaction. Two possibilities exist for how enzymes can increase a rate constant: by decreasing the activation energy (and therefore increasing the exponential term at all temperatures) or by increasing the rate of approaches to the activation barrier. The former approach has driven our understanding of enzyme catalysis for decades and dates back to Linus Pauling in the 1940s.[21] The driving force for lowering the activation barrier is believed to be the enzyme being structured to stabilize the transition state. This understanding has led to several advances in the fields of pharmacology and enzyme design.[22-25] A similar model, known as the Circe effect, lowers the activation barrier by destabilizing the reactant state thereby increasing its energy and decreasing the difference in energy between reactants and the transition state.[26] Although the idea of enzymes altering the Arrhenius prefactor has historically been ignored as significant, some increase in reaction rate on enzymes come from the increase in likelihood for interaction of reactants by being sequestered near each other on an enzyme molecule.[27] The energetic barrier between products and reactants and the effect of enzymes is generally illustrated as in figure 1.1.

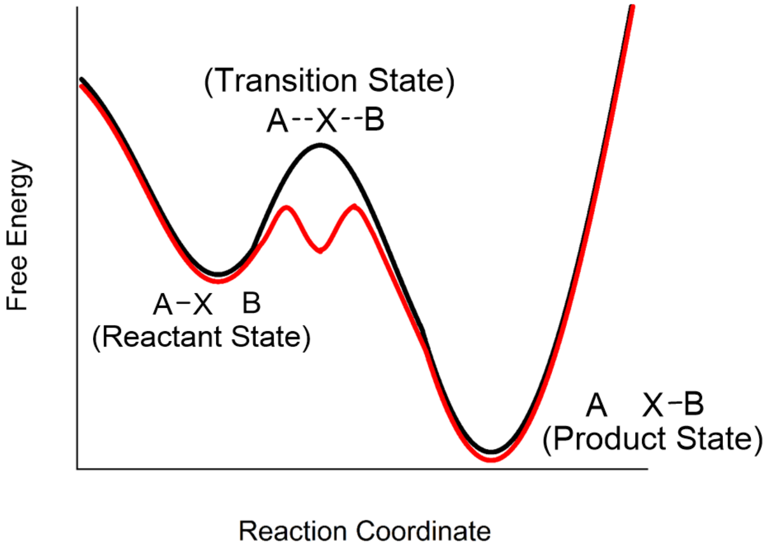

Figure 1.1: Two-dimensional reaction coordinate. A high-energy barrier exists between the transformation from reactants and products in a chemical reaction. This energy of this barrier is often considered to be the energy of the midpoint between a reactant-like state and a product-like state (black line). The reaction rate enhancement of enzymes is mostly attributed to stabilizing the transition-state and lowering the activation barrier (red line). An enzyme-catalyzed reaction follows a different mechanism which normally has additional steps; the additional local minimum in the red line is indicative of an additional step.

One problem with applying the simple transition state theory to enzymes is that it implies a very limited set of states for the enzyme to populate between reactants and products; however, enzymes, like all proteins, are known to exist in more than one conformation.[28-29] Therefore, the phase space of the reaction coordinate cannot be accurately represented by a simple two-dimensional perspective. A more appropriate representation also includes all the possible conformers of the protein in a three-dimensional landscape (fig. 1.2).[30] In reality, the landscape requires more than three dimensions to be fully described, but a three-dimensional approximation is useful for illustration. The various conformations in the landscape can be separated by low barriers representing small-scale atomic level motions or vibrations, by high barriers representing large-scale protein domain rearrangements, or anything in-between.[31-32] A central issue in understanding enzyme function is how a reaction proceeds through this landscape. Evidence from single-molecule enzymes studies suggest that there is a distribution of reaction rates possible in a catalytic ensemble, but it is unclear what causes this distribution.[33-34] Are enzymes trapped along off-progress states during the one possible reaction pathway? Or, perhaps are there multiple pathways that exist through the landscape with varied reactivity? These question are addressed by the work presented herein.

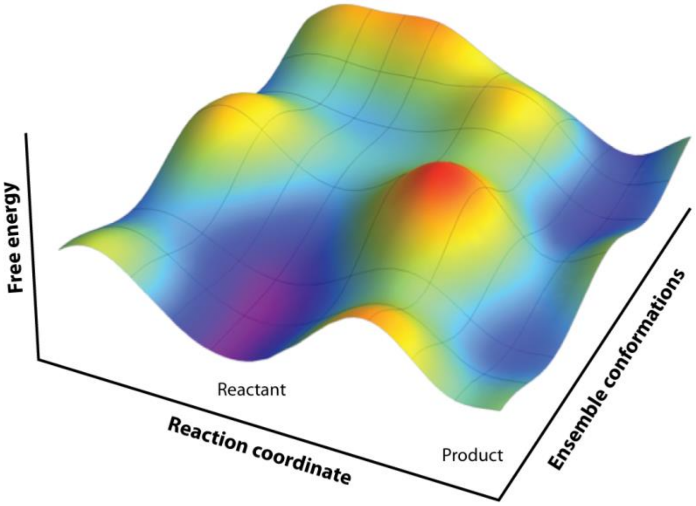

Figure 1.2: Three-dimensional reaction coordinate. Enzyme reaction coordinates are not well-described in a traditional two-dimensional scheme involving only free energy and the reaction coordinate. Enzymes, like all proteins, can exist in large array of energetically similar conformations. A more accurate energy scheme is a landscape which includes these conformations as an additional third axis. The figure is reproduced from reference [30] with permission of Annual Reviews.

A well-studied conformational change that occurs in many enzymatic reactions is a substrate binding-induced rearrangement of the protein structure. This structural change is known as an induced fit. Generally, the enzyme is considered to exist in a state with the active site fairly open and accessible to solvent; however, upon substrate binding, the protein structure changes to lock-down around the substrate before the catalytic reaction proceeds.[35] A good example of this process is visible in the substrate-free crystal structure of hexokinase as compared to the substrate-bound crystal structure as shown in figure 1.3. This simple, introductory approach to protein motion is limited because it implies that only substrate binding and the analogous product release will induce changes in the protein structure. Instead, we know that enzymes continue to change structure throughout the reaction. The conformational change is not a one-time event but rather a conformational search for the appropriate substate to continue reaction progress.[30] This search is due to normal fluctuations caused by thermal energy movement and equilibration.[36-37] Since this search and the corresponding motions are slow, it is clear that these motions slow down enzymatic catalysis. Diffusion-limited enzymes described above tend to minimize these motions and the requisite search for them.[31] Therefore, another question arises – why would enzymes, generally considered a model of efficiency, evolve to include these motions in the reaction coordinate?

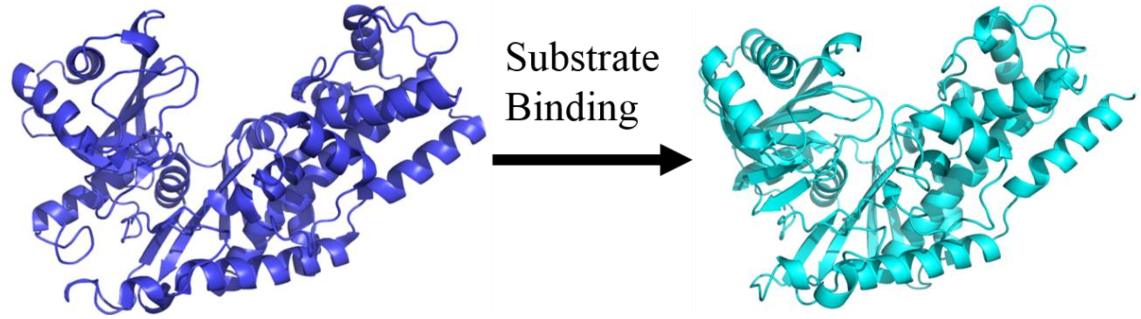

Figure 1.3: Induced fit in hexokinase. Hexokinase is an example of the induced fit model of protein structural rearrangement. Upon binding of substrate to its active site, the open V-shaped protein structure (left image, PDB: 1IG8) locks down into a more compact structure (right image, PDB: 1BDG).

To learn more about the role of conformational changes in enzymatic reactions, we chose to investigate a particular class of motions: loop motions. Loops are small sections of proteins that join consecutive secondary structures within a protein. Loops can be classified by the different types of secondary structures they connect and by the geometric arrangement they form.[38] The loop sections of three different enzymes we studied are shown in figure 1.4. Loops have been extensively studied computationally to be able to predict their structure from the primary sequence of a protein.[38-39] Additionally, some loops are known to serve essential functions in proteins by serving as binding domains for ligands.[38] Our interest in loops is for their known flexibility. Loops tend to generally be more mobile regions of protein structures and these motions can be critical to protein function. There has been a lot of interest in predicting the various configurations a loop structure will take and on what timescale.[40-41] It is necessary to understand both the functions and the timescales of loop motions to fully describe the conformational phase space available to enzymes during their reaction cycle. We are contributing to this work by experimentally studying the rates of loop motion in enzymes.

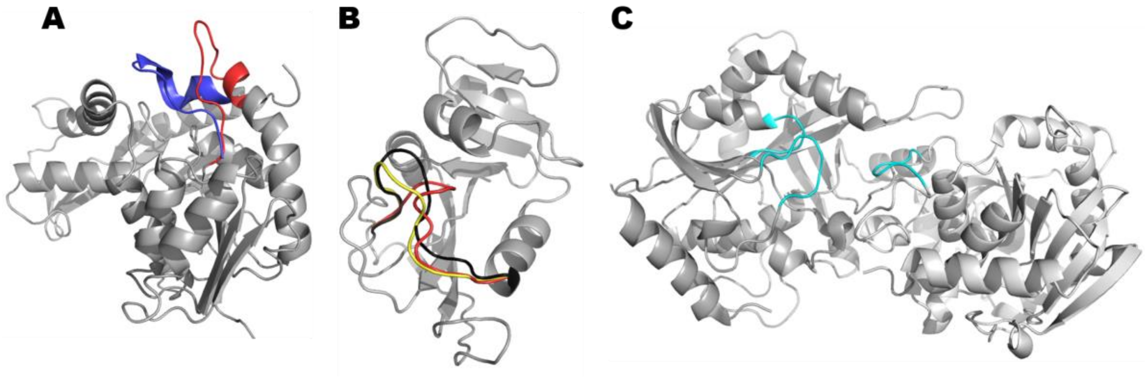

Figure 1.4: Loop sections of the three enzymes studied in this report. Image A shows the loop structure of lactate dehydrogenase in its open (red, PDB: 6LDH) and closed (blue, PDB: 1LDM) forms. Image B shows the Met20 loop of dihydrofolate reductase in its open (yellow, PDB: 1RA9), closed (black, PDB: 1RX2), and occluded (red, PDB: 1RX7) forms. Image C shows the three loop structures of purine nucleoside phosphorylase that close down over the active site upon substrate binding (PDB: 4EAR).

The majority of the work detailing loop structure timescales has been computational due to the difficultly of studying the relevant timescales. Loop motions in enzymes tend to occur on timescales of microseconds to milliseconds.[31] Common instrumentation for studying these reactions using mixing techniques tends to be limited to the millisecond and slower timescale. Therefore, the development of easy to use methods with quicker observation windows is a must for the development of this field. In chapter 2 of this writing we describe two very different, but complimentary techniques to study the microsecond-millisecond timescale: laser-induced temperature jump spectroscopy and microfluidic fast mixing. We subsequently describe the application of these methods to three loop-containing enzyme model systems. Chapter 3 discusses a very simple loop system in lactate dehydrogenase (LDH). This loop is known to close over the active site upon substrate binding to protect the active site from solution and provide essential structural support; however, our work indicates that this process is not full-proof. We will show how the substate that the loop closes into has important ramifications for catalytic rates. Chapter 4 displays our work with dihydrofolate reductase (DHFR). DHFR has several loop structures, but one in particular, the Met20 loop can exist in several distinct states. The movement of the Met20 loop is critical for reaction progress. We display here a system for studying the rates of the loop motion which will allow for studying the differences in stability between the loop conformers. Chapter 5 applies our fast mixing methods to purine nucleoside phosphorylase and its three loops that must open and close during the reaction cycle. We are able to probe the loop motions directly to better understand the inhibition mechanism of a novel transition-state mimic. By investigating the function of these loops in the three different proteins we are able to give insight into why loops are important for enzyme function and the effects that they have on observed bulk solution properties.

Chapter 2. Measuring Biomolecular Dynamics on the Submillisecond Timescale

Section 2.1 Introduction to Common Submillisecond Techniques

A critical issue for studying time-dependent processes is how to initiate the process. If all reaction conditions are met for a given favored reaction, the reaction will occur spontaneously as governed by the kinetics of the reaction. This is problematic for the experimentalist because they are unable to predict when to observe a reaction. The solution to this problem is to have control over the initiation of the reaction and therefore be able to align observation with initiation. Several methods exist to initiate reactions and their applicability depends on the desired observation timescale and the reaction conditions. The methods commonly applied to biophysical systems can generally be divided into two classes: photo-initiated and rapid-mixing.[42]

Photo-initiated methods work by using light to induce a significant change in a reaction solution. For the sake of explanation, we can divide these topics into those that change the environment around the reaction and those that change the concentration of reactants. Environmental changes can include changing the temperature or the pH. To change the temperature of a reaction a strong photoabsorber must be present in the solution, an intense light pulse is focused on the sample, and the absorber absorbs a significant amount of light energy and converts it to heat that is locally dispersed in the solution. Example absorber systems include water/D_2O, gold nanoparticles, and organic dye molecules.[43-45] See section 2.2 for an expanded discussion of this technique applied to temperature-jump relaxation spectroscopy.

The pH of the reaction environment can also be quickly changed by laser pulses. This procedure depends on a change in the acidity of a molecule when moved from its ground state to an electronic excited state. Molecules that exhibit this property are called photoacids. Upon excitation from a laser pulse, a proton can be released from the photoacid into solution and have enough time to alter the reactants as if they were in a lower pH solution. pH jumps of several pH units can be achieved by this method.[46-48]

Intense light can also be used to rapidly change the concentration of the reactants in a given sample. A method for quickly introducing more reactants with light is by the use of photocages. A photocage is a molecule that is made up of a reagent of interest molecularly attached to another trapping molecule. When the photocage is excited by an intense laser pulse the stability of the attachment between the reagent molecule and the trapping molecule is disrupted allowing for the release of the reagent into the solution. Photocaged reagents can be small ions, like Ca^{2+}, or large biological substrates like ATP.[49] The photoacids described above can also be thought of as acting like photocaged reactants, especially if the released proton is used directly in a reaction and is not just used to modify a biological structure. The distinction made here between the two is purely for ease of explanation. Flash photolysis is a similar, but different, process to the use of photocages where light is used to dissociate a ligand from a studied reaction system. The ligand will shortly recombine with the reactant. The kinetics of dissociation and reassociation can be studied. One well studied biological example of flash photolysis is the photodissociation of carbon monoxide (CO) from hemoglobin and other heme proteins.[50-52] A final related technique is the stepwise photoexcitation of a protein system where each excitation event moves the reaction system stepwise through its mechanism. This is a very useful technique because it allows for each step in the reaction mechanism to be studied independently. An example of this approach is the investigation of the mechanism of photosystem II by a series of four sequential photooxidation steps of the protein itself.[53]

The observation window of photo-initiated approaches are limited by the temporal width of the light pulse or by the timescale of the process it is exciting. While these limits are generally orders of magnitude faster than the physical limitations of mixing methods, see below, the photo-induced methods are not without limitations. Photo-induced methods are limited by whether the reaction contains a photo-inducible trigger or whether one can be introduced. The introduction of a photo-trigger is not always trivial. Considerations include making sure the trigger light does not disturb the probing method, making sure the introduction of a non-natural trigger does not disturb the reaction mechanism, and, as in the case of photocaged compounds, making sure it is even possible to produce a photocaged reactant of interest in a time and cost-efficient manner. Often these considerations can be overcome, but not in all circumstances. Rapid mixing methods, in contrast, are more broadly applicable because they work with just about any soluble reaction.

Rapid mixing involves quickly combining reaction components; however, rapid does not mean instant. The observable timescale of rapid mixing is limited by how fast reactants are mixed to a homogenous, or homogenous enough, solution. Common instrumentation for standard methods like stopped-flow and quenched-flow tend to complete the mixing process around a 1 millisecond timescale or slower.[42, 54-56] That means that only kinetic events slower than a millisecond can be resolved. Due to this limitation, improving rapid mixing devices is an active area of research.[57-64] The most common approach for improvement of mixers is to decrease the scale of the mixer.

Generally speaking, it is easier to mix two volumes quickly if the two volumes are smaller. These so called microfluidic fast mixing devices have been developed with experimentally-verified mixing times of around 50 µs[58, 65-66] and theoretical mixing times mixing times as low as 1 µs.[62] In fact, improvements in the traditional stopped-flow approach have also come by decreasing the volume of the reaction vessel, reaching sub-millisecond mixing times in specialized systems.[56]

These advancements in mixing times have come with significant drawbacks. Smaller size mixers are more prone to clogging and necessitate more frequent replacement. Although this is a common problem for all microfluidic devices due to solution contaminants, experiments using biological samples suffer additional clogs due to enhanced sample aggregation in tight spaces.[67-70] Advancements in microfluidic mixers have also come with increasingly more complex designs often requiring specialized fabrication techniques that are unavailable to most users. Furthermore, the polymer materials normally used to fabricate these small mixers, such as polydimethylsiloxane (PDMS), have limited optical transmission. This is problematic because it limits the available methods for observing the reactions. PDMS is not transmissive for UV or mid-infrared light; however, both types of light are important probes for biological samples.[71-73] This issue can be somewhat avoided if an optically transparent window is used on one face to allow for observation; however, this limits the observation techniques to emissive or scattering-based probing techniques, like fluorescence and Raman spectroscopies, or very strong transmission signals.[74] Examples of some of these designs can be seen in figure 2.1. In section 2.3 we report the design and application of a new microfluidic device. The device is demonstrated to allow for observation below the millisecond timescale, is relatively simple to manufacture, and can be quickly/cheaply cleaned or replaced when clogged.

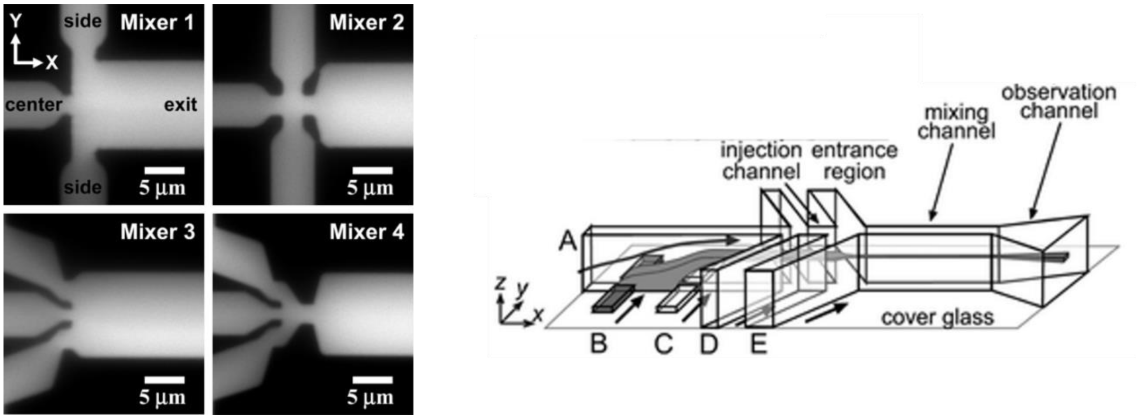

Figure 2.1: Examples of complex mixing devices. The collection of four images on the left display the mixing region of four different mixers. All of the mixers are modifications of a classic T-style mixer where two solutions (one in the center and one in the sides) are rapidly mixed at a T-junction before flowing out an exit channel. The modified geometries decrease the mixing time but increase the complexity. The image on the right shows a design for a three-dimensional mixing device made out of molded polydimethylsiloxane attached to a glass slide. The manufacturing of three-dimensional microfluidic devices out of curable polymers is not trivial. The left image is reprinted with permission from reference [64]. Copyright 2007 American Chemical Society. The image on the right is adapted from reference [58] with permission of The Royal Society of Chemistry.

The combination of mixing methods and photo-induced methods presented here has allowed for significant advancements in the study of biophysical kinetics; however, as described above, they are not without their limitations. It is typically useful to study a biophysical reaction with multiple techniques because different techniques probe the reaction from different parts of the reaction landscape. For example, while mixing methods will generally capture rate-limiting protein dynamics, the photo-induced temperature-jump method can frequently allow for observation of fast not rate-limiting steps. Together the recognition of limitations of current methods and the desire to investigate as much of the reaction landscape as possible drives our development process for new experimental techniques. In the following sections, we will describe our developments with two complimentary techniques: laser-induced temperature-jump (T-jump) spectroscopy and microfluidic fast mixing. The T-jump method investigates reaction systems close to their equilibrated state, and while the technique has been around for several decades, our introduction of new approaches to this method has made it even more functional than before. We will also describe the construction and evaluation of a microfluidic mixer that focus on enhancing the ease and flexibility of using the mixer without sacrificing its improvement in mixing time. The development of these methods was critical to the analysis of the enzyme systems described in later chapters.

Section 2.2 Laser-Induced Temperature-Jump

Temperature-Jump (T-jump) spectroscopy is an example of a wider class of kinetic methods that are driven by relaxation kinetics. Relaxation kinetics refers to following the relaxation of a system at equilibrium to a new equilibrium after a perturbation that changes its environment. The perturbation generally only changes the equilibrium a small amount; therefore, the kinetics observed are of systems in an equilibrated state similar to the final equilibrated state that will be observed. An equilibrium distribution of reactants and products is already achieved prior to the perturbation.[75] This is different than many traditional kinetic methods, like mixing methods, because the equilibrium before all necessary reactants are mixed is very different than the equilibrium reached after the reaction has occurred. Prior to mixing, the reagents are more reactant like, and then after the mixing, the reagents are more product like. One of the advantages of using relaxation techniques is that because the starting point of the reaction is so different than the starting point of other kinetic techniques, it can allow for exploring other parts of the reaction landscape not usually observed.

The perturbation used in a relaxation method is what differentiates the various methods from each other. Two classes or perturbations exist. The first class includes so called “jump” methods. The perturbation in this class occurs as a fast change to some parameter like temperature, pressure, or electric field. The perturbation can then be repeated at later time when the system has had time to fully return to the non-perturbed state. In terms of a temperature-jump, the system is heated from a low temperature to a higher temperature, then after the heat is fully dissipated through the sample and returned to the initial temperature, the jump can be repeated. The observation window for this class of methods is limited by the time it takes for the perturbation to be created and the duration of the perturbation, see discussion below of the T-jump method for more detail. The second class includes stationary relaxation methods such as ultrasonic techniques or stationary electric field methods. This class of relaxation methods relies on the same temperature, volume, and electric field-dependence of the previous methods but instead of a one-time perturbation that can be repeated, the perturbation is due to an oscillating field, such as a sound wave or electric field, which periodically modulates the perturbation. While this second class of methods is often technically more difficult to use, variations on these approaches can measure relaxation times in the range of 10^{-5} – 10^{-11} seconds. Realistically, however, a single instrument of the second class of methods can generally only cover about one order of magnitude of time. A single instrument of the first class of methods does not have the same limitation and can be used to observe the entire observation window from perturbation onset to conclusion which can often cover several orders of magnitude in time.[75]

The kinetics of the relaxation process are more complicated than those observed with many other techniques. In many traditional kinetic techniques, like mixing or flash photolysis, where the reaction is initiated far from equilibrium the chemical potential drives the reaction forward predominantly in one direction such that only the kinetics of the forward processes are normally observed. In the case of relaxation methods, however, because the system is at equilibrium and the typical change in the system is small, both the forward and reverse reactions are occurring while equilibrium is being reestablished. The complexity of the observed rate is normally notated by describing the observed rate as a relaxation rate instead of as the reaction rate.[75] The relaxation rates $\left({}^{1}/_{\tau}\right)$ of the jump class of methods for a simple unimolecular two-state system, equation (2.1) and for a simple bimolecular two-state system, equation (2.3), are shown in equations (2.2) and (2.4) in terms of the rate constants and equilibrium concentrations of the system at the elevated or jump state.

$$\underset{k_{-1}}{\overset{k_1}{A \leftrightarrow B}} \tag{2.1}$$

$$ {}^{1}/_{\tau} = k_1 + k_{-1} \tag{2.2}$$

$$\underset{k_{-1}}{\overset{k_1}{A + B \leftrightarrow C}} \tag{2.3}$$

$$ {}^{1}/_{\tau} = k_1\left(A_{eq} + B_{eq}\right) + k_{-1} \tag{2.4}$$

Two observations are worth noting about equations (2.1)-(2.4). First, both the first-order and second-order system have only one relaxation rate. The number of relaxation rates is related to the number of reaction steps and states in the equilibrium as a whole. While this can get complicated for cyclic or branching pathways with interconnectivity, a general rule is that the number of relaxation times for a system is equal to the number of states in the system minus one. In the case of equation (2.1), A defines one state and B defines another state, so we would expect one relaxation time. In the case of equation (2.3), A + B defines one state and C defines another state, so we would expect one relaxation time here as well. The second observation is that even though the observed relaxation times are dependent on both the forward and reverse reaction rate constants, through careful experimental design one can force the relaxation rate to be dominated by only one rate constant. For example, in a unimolecular two-state transformation, like equation (2.1), if the final temperature is chosen so that one state is significantly dominant over the other, then one rate constant will be much larger than the other and the relaxation rate will essentially be equal to the dominant rate constant.[76] Or, in the case of a bimolecular reaction, like equation (2.3), where simply choosing an appropriate temperature maybe insufficient, careful selection of reactant concentrations or a range of concentrations often allows for determination of the rate constants from the observed relaxation rate.[77] While these simplification techniques are useful and work for simple systems, they are often not enough to sort out rate constants of more complex systems. As the number of states grows large, the complexity and number of expressions for the relaxation rates grows as well. This can make it hard to even identify the appropriate model in the most complex systems.

The relaxation method that we focus on in our work is temperature-jump. T-jump is one of the oldest and most used of the relaxation methods.[78] This approach relies on the shift in equilibrium of a reaction system with temperature. Such a shift is present for any equilibrium that has an enthalpic dependence.[75] The relationship between temperature (T), enthalpy ($\Delta H°$), and equilibrium constant (K) is normally expressed in the van't Hoff equation as shown in equation (2.5).

$$\ln\left(\frac{K_2}{K_1}\right) = \frac{-\Delta H°}{R}\left(\frac{1}{T_2} - \frac{1}{T_1}\right) \tag{2.5}$$

The requirement for an enthalpy change in a reaction equilibrium is not a problem for studying most enzymes. The two major steps in enzyme reaction, the substrate binding and the chemical transformation, generally involve the making and breaking of bonds and therefore frequently include a change in enthalpy. However, not all enthalpically driven processes will be visible due to being present only at small populations, limitations on the probing method, or only small equilibrium shifts being achieved by a certain temperature-jump at a given initial temperature.

To better describe the effect of the temperature-jump it is instructive to describe the entire process. While enzyme systems at equilibrium will typically have more than two states populated, it greatly simplifies the description to think about the equilibrium shift between only two states. Initially, the system is at an equilibrium, K_1, and defined by the temperature T_1. Then temperature of the system is rapidly raised to a new temperature, T_2, by the introduction of energy through electricity or light. Next, the reaction system, which is still at the initial equilibrium, K_1, shifts to minimize the disturbance and increased chemical potential by relaxing to establish a new equilibrium,

K_2 that is more stable at T_2. Eventually, the heat that was deposited into the system equilibrates with its surroundings and both T_1 and K_1 are reestablished. The system can then be cycled through another temperature-jump as required for signal averaging. The temperature-jump process can be expressed pictorially as shown in figure 2.2 using the labels described above.

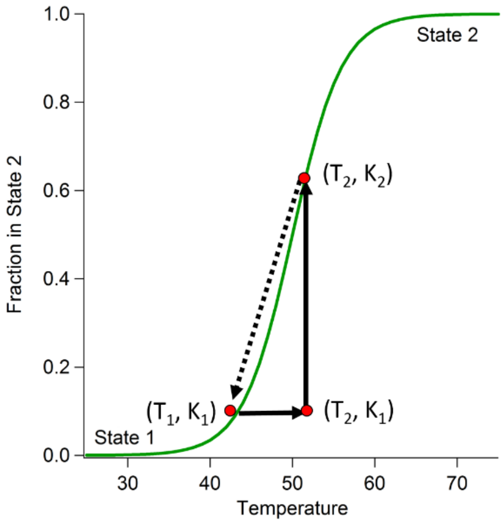

Figure 2.2: Visual representation of the temperature-jump process. The system is at an initial temperature (T_1) and the corresponding equilibrium (K_1). The temperature is then raised (T_2) rapidly enough that the system cannot immediately respond and then has increased chemical potential. The system relaxes by shifting to an equilibrium (K_2) that matches the current temperature (T_2). At some later time, the heat dissipates out of the system so the temperature and the equilibrium shift back to their initial values (T_1, K_1).

The oldest methods for generating the transient change in temperature, the temperature-jump itself, rely on electric discharge.[78] This approach works by immersing a high-voltage capacitor and ground in the sample solution. The capacitor is charged by a high-voltage generator, and then discharged by a triggering spark gap between the capacitor and the ground. Some of the discharged energy excites the sample solution which is then dissipated as heat.[75] The heating timescale is limited by the discharge timescale of the circuit as shown in equation (2.6) where τ_d is the discharge time, R is the resistance of the circuit, and C is the capacitance of the capacitor.

$$\tau_d = 0.5RC \tag{2.6}$$

Since the resistance of the circuit includes the resistance of the sample solution, lowering R often becomes the limit to minimizing the heating time. Increasing the conductivity of the solution by increasing the electrolyte concentration of the solution is usually the most effective method for decreasing R. This approach does have a practical limit due to the solubility limit of electrolytes in the solvent and the compatibility of biological samples with salts.[75] A more flexible approach to heating the solution comes from the absorption of electromagnetic radiation. While this has been accomplished with microwave pulses, which is useful on a wide range of solvents,[79] a better alternative for the study of biological systems takes advantage of the infrared absorbance of water. Water and its heavy isotopic variant D_2O both have significant infrared absorbance bands throughout the near and mid-infrared spectrum allowing them to be excited by a wide-range of light pulses.[80-81] Various pump laser wavelengths have been employed in this regard, such as the 1064 nm fundamental of a Nd:YAG laser,[82] the Raman shifted pulse of the Nd:YAG at 1410 nm,[83] the 1315 nm wavelength of an atomic iodine laser,[84] and the 2065 nm output of a Ho:YLF laser.[85] These laser-based methods all significantly decrease the heating time of the T-Jump system and do not require any additional additives in the solution; however, they are limited by only producing temperature changes of a few degrees.

A more powerful variation of the laser-induced T-Jump utilizes the Raman shifted output of the Nd:YAG fundamental passed through methane or hydrogen gas at wavelengths of 1540 nm for an H_2O solution or 1910 nm for an D_2O solution respectively. This variation can be used to routinely generate temperature-jumps of 10 – 30 °C from a 10-70 mJ pulse and has been used successively in a number of biophysical studies.[76-77, 86-91] This is the approach we take to studying lactate dehydrogenase by temperature-jump as shown in chapter 3. A similar, but more straight-forward approach has recently become available with the commercial introduction of Ho:YAG lasers. The fundamental wavelength of these lasers is 2090 nm and therefore requires no Raman shifting prior to use in a temperature-jump experiment.[92] We are routinely able to utilize this approach to generate 10 – 20 °C temperature-jumps with an approximately 7 mJ pulse with samples in D_2O. We use this approach in our studies of dihydrofolate reductase described in chapter 4. Together these two approaches to laser-induced temperature-jump allow us to produce larger increases in temperature on a fast, 10-20 ns timescale. Due to these significant increases in usability of the temperature-jump approach we are able to observe some enzymatic events that would have not been accessible with older methodology.

Section 2.3 Three-Dimensional Capillary Flow Fast Mixer

The work presented in this section is adapted from reference [93] with permission from The Royal Society of Chemistry. The presentation below is a modified version of the publication reproduced here to give context for experimental results shown in later chapters.

The utility of mixing devices to study chemicals reactions and the shift toward the use of microfluidic mixing devices to decrease mixing times has already been discussed in section 2.1. We have also pointed out that in their attempts to decrease mixing times, researchers have made mixing devices increasingly complicated and spectroscopically inflexible. These two drawbacks were the focus of our efforts to develop a novel microfluidic fast mixer. The main drawback of complexity in our view is a lack of accessibility which is problematic for two reasons. First, when these mixers clog irreparably, as they often do on this scale, it makes it difficult and costly to acquire a replacement device. Second, a lack of accessibility inhibits progress for the field as a whole because only a select group of researchers can use and improve the technique. To this end, our goal was to design a mixer constructed only of commercially available parts. The viewing window of most mixers is constructed out of glass or polydimethylsiloxane (PDMS), these materials have limited transmission in the ultraviolet region of the light spectrum which is important for intrinsic protein and nucleic acid absorbance and fluorescence. Furthermore, mixers will often be constructed with only one side accessible for light transmission. This prevents mixers from being able to be used with light absorbance as the spectroscopic probe. Therefore, we designed our mixer so that the viewing window of the mixer was made of fused silica, which is highly transparent from around 200 nm and to about 2100 nm, and was transmissive from all sides.

We also chose to develop our mixer in a three-dimensional geometry and to operate under conditions that would generate a laminar, as opposed to turbulent, flow. Laminar flow conditions means that diffusion will be the process that drives mixing. To achieve small mixing times the diffusion length will have to be as small as possible; therefore, hydrodynamic focusing, as developed by Knight et al., will be necessary.[66] The main drawback to turbulent flow on this size would be the high flow rates required which would lead to high sample consumption.[64] A three-dimensionally hydrodynamically focused sample stream has two advantages for our mixer. The first is that we expected faster diffusion times since mixing occurs from all sides of the sample stream. The second advantage is that, as opposed to two-dimensional mixers that have significant drag along the mixer walls and therefore a velocity distribution perpendicular to the walls of the mixer, a three-dimensional mixer has symmetric velocity throughout the entire sample stream because the sample stream is completely isolated from the walls of the mixer. This symmetry simplifies data interpretation. It was with these guiding principles in mind that we developed the mixer described below that was first published in the journal *Lab on a Chip*.[93]

Mixer Construction

The mixer is constructed from two concentric cylindrical capillaries and achieves uniform 3D focusing by completely surrounding a sample stream held in the inner capillary with a flowing sheath solution held in the outer capillary. The inner capillary ends part of the way through the outer capillary which allows the two solutions to mix. The sheath solution focuses the sample solution hydrodynamically into a narrow jet so that rapid diffusional mixing between the solutions occurs. Since the protein diffusion is slow, it remains in the central sample stream, whereas substrates within the sheath solution diffuse into the protein stream, initiating the reaction. Our design is related to that developed by Pabit and Hagen for fluorescence kinetics studies.[61] However, our mixer produces better focusing of the sample stream and therefore shortens mixing times through the use of a tapered inner capillary and a cylindrical, rather than rectangular, outer capillary. While Pabit and Hagen report a mixing time of approximately 425 μs, we observed complete mixing in under 100 μs.

The mixer is made with standard plastic parts and PEEK tubing supplied by Idex (Oak Harbor, WA) and fused silica capillaries from Polymicro Technologies (Phoenix, AZ) (fig. 2.3A). The mixer contains an inner and outer capillary that carry the sample and sheath solutions, respectively. The outer capillary has a 350 μm outer diameter (OD) and 200 μm inner diameter (ID), and the inner capillary has a 90 μm OD and 20 μm ID before its narrowed tip. The outer and inner diameters at the tip of the inner capillary were reduced at the outlet to 20 μm and 8 μm, respectively (fig. 2.3B). This tapered tip was produced by a simple flame pulling method. First, the capillary was attached to a plastic 50 mL cylindrical tube filled with 45 mL of water, approximately 57 g total mass. Second, the capillary was suspended from a support stand with the tube hanging off the stand to provide a pulling force on the capillary. Finally, the suspended capillary was melted with a propane pencil flame burner torch until the force of the suspended tube separated the capillary into two segments, each having a narrowed tip where the flame had been applied. The characteristics of the tapered outlet are easily tuned by adjusting the weight of the "puller", i.e. by changing the volume of water in the suspended tube, decreasing the volume of water produces smaller outlet diameters and *vice versa*. The pulled inner capillary was placed in an Idex MicroTight tubing sleeve to maintain its position within the mixing system. The inner capillary was then inserted into a MicroCross, which directed the inner capillary through the center of the outer capillary (fig. 2.3C). Both capillaries were secured to the MicroCross via 0.025" diameter MicroFerrules and fitting nuts.

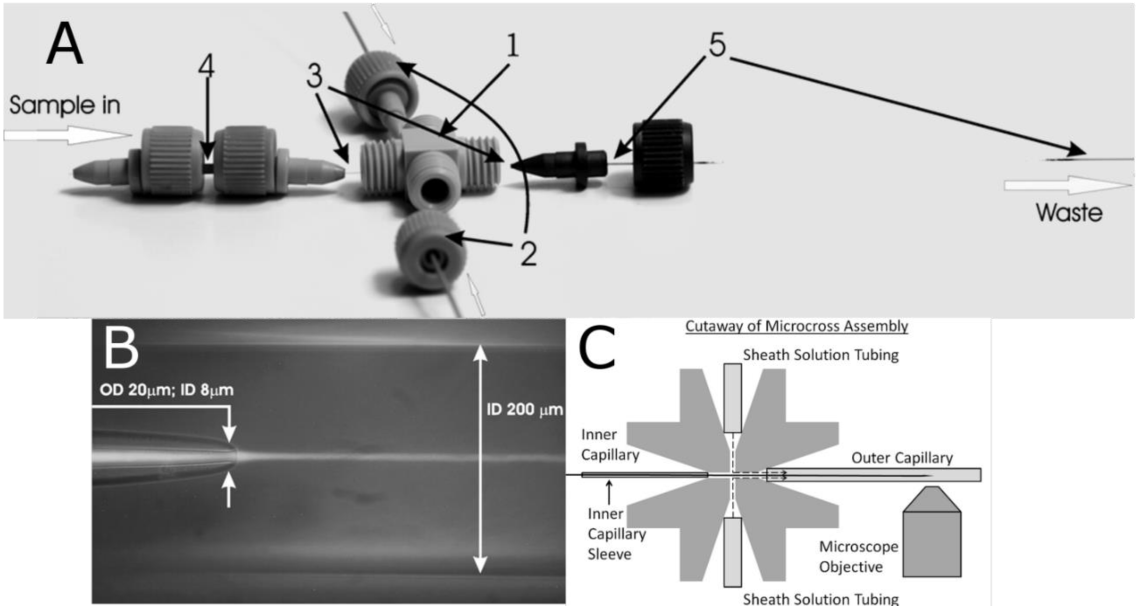

Figure 2.3: Our microfluidic mixer design. (A) The components include: (1) MicroCross that holds 360 μm outer diameter tubing and has a 150 μm through-hole (2) 1/32” PEEK tubing that has a 250 μm inner diameter and carries sheath flow from HPLC pumps (3) Fused silica capillary for sample flow: outer diameter = 90μm; inner diameter = 20μm (4) MicroTight tubing sleeve (5) Fused silica capillary for sheath flow: outer diameter = 350 μm; inner diameter = 200 μm. All parts are connected via fitting nuts and MicroFerrules with 0.025” diameters. (B) Overlay of bright field and fluorescence images of capillary flow system. The sample flows from left to right through the inner capillary, and the sheath solution flows from left to right through the outer capillary, with dimensions as indicated. The tapered capillary tip and 3D focusing by the sheath solution create a narrow sample jet that is 2-5 μm in diameter. A laminar flow of the sample is established and rapid mixing occurs via diffusion. The sample appears as a bright stream due to fluorescence of Eu beads. The sample flow rate is 0.025 μL/min, and the sheath flow rate is 100 μL/min. (C) Cutaway of MicroCross assembly showing how solutions are kept separate (not to scale). Ferrules (not shown) hold each tube or capillary in place. The sheath solution can only flow out through the outer capillary, whereas the inner capillary outlet is outside of the cross and therefore the mixing region is outside of the cross, in the vicinity of the microscope objective.

The sample and sheath solutions were delivered separately to the inner and outer capillaries, respectively. The sample solution was held in a 1 mL Tuberculin (Franklin Lakes, NJ) plastic syringe and was flowed by a KD Scientific (Holliston, MA) continuous cycle syringe pump through 1/32” PEEK tubing to reach the inner capillary. The sample was filtered with a 0.5 μm stainless steel frit in-line syringe filter from Idex.

The sheath solution was flowed by two HPLC pumps, Rainin SD-200 (Oakland, CA), through 1/32” PEEK tubing channels that were directed into opposite sides of the MicroCross to bring the sheath solution into the outer capillary. The two pumps were operated in asynchronous cycles to minimize pulsing of the flow due to the nonuniform pumping cycles of each pump.

The mixer was mounted onto an Applied Scientific Instrumentation (Eugene, OR) MS-2000 automated stage using Newport (Irvine, CA) miniature optical rails and lens mounts. A 3” rail and a 6” rail were attached at their ends. The 3” rail was fixed to the stage, while the 6” rail was placed over the objectives. Two fixed-position lens mounts were attached to the 6” rail, and the capillary system was secured within these lens mounts. The stage was attached to an Olympus (Center Valley, PA) IX81 microscope, and the capillary system was rotated around the connection between the 3” and 6” rails to place the mixer directly into the microscope objective’s image plane.

Microscope images were collected on a Hamamatsu (Bridgewater, NJ) C9100-14 ImageM-1k EM-CCD Camera. Integration time of the camera was varied from 100 to 1000 ms with a gain setting of 1 and an intensification setting of 255 depending on the intensity of the sample fluorescence. The CCD array was actively cooled to -57 °C. The microscope and camera were controlled by Slidebook 5.0 software from Intelligent Imaging Innovations, Inc. (Denver, CO). Images were exported as TIFF files into Igor Pro software from WaveMetrics (Portland, OR) for analysis. For every image collected in one of the experimental procedures, the sample fluorescence intensity was plotted against pixels along the length of the image. To make this plot, the sample fluorescence intensity and the background signal intensity were integrated over a specific number of pixels across the width of the image at each pixel along the length of the image. The background signal was subtracted from the sample signal, which was then plotted against pixels along the length of the image. The data were fit to appropriate functions in Igor Pro (WaveMetrics).

Flow Rate Calibration

The amount of time represented by each pixel in fluorescence images of the sample flow was determined by observing the fluorescence decay of Eu nanospheres within the mixer. Europium (Eu) carboxylate-modified nanospheres 40 nm in size were purchased from Invitrogen (Grand Island, NY) and used without further modification. The fluorescence lifetime of the Eu nanospheres was measured separately using a time-resolved fluorescence instrument. Dividing the measured lifetime of the Eu nanosphere fluorescence by the observed decay in pixels along an image collected under the microscope gave a pixel-to-time conversion factor for the mixer at a given sample and sheath flow rate. We consider this conversion factor to be the time resolution of the mixer.

The fluorescence decay time of the Eu nanospheres was measured using a pulsed laser based fluorescence lifetime instrument. A sample of Eu nanospheres in a 1 cm path length quartz fluorescence cuvette, Model 29F-Q-10, from Starna Cells (Atascadero, CA) was excited with a 2 ns pulse at 351 nm from a diode-pumped, Q-switched Nd:YLF laser, Model: QUV-351-100, from CrystaLaser (Reno, NV) with a repetition rate of 1 kHz. The Eu fluorescence was collected perpendicular to the incident beam and focused onto a SPEX 1681A monochromator (Spex Industries, Edison, NJ) set to pass 610 nm light with an input slit width of 0.58 mm and output slit width of 0.62 mm. A Hamamatsu R7518 photomultiplier tube (PMT) was attached to the monochromator output slit for detection of the fluorescence signal. The PMT signal was terminated at 50 Ω into a Lecroy (Chesnut Ridge, NY) WaveSurfer 62 Xs-A digital oscilloscope. The incident light that passed through the sample was collected on a ThorLabs (Newton, NJ) DET10A photodiode, terminated at 50 Ω into the same oscilloscope, and used as the trigger source for data collection. The recorded transients had a time resolution of 2 ns. Signal averaging of 1000 transients produced the fluorescence decay used for the lifetime analysis. This lifetime data is shown in figure 2.4. This signal was fit to a single exponential function, which yielded a lifetime of 548 μs that is comparable to the approximate 600-μs lifetime reported by the manufacturer.

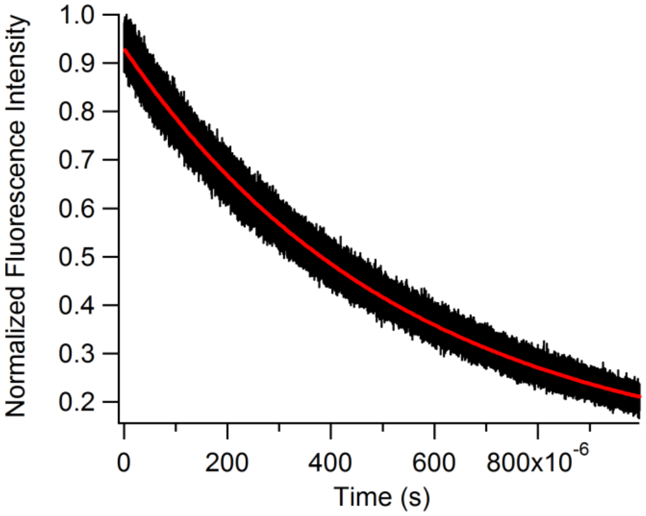

Figure 2.4: Fluorescence decay signal of Eu microspheres. Data was fit to a single exponential of the form: $y = y_0 + Ae^{-x \cdot invtau}$. invtau is the decay rate of Eu microsphere fluorescence. invtau was fit to 548.2 ± 0.3 μs.

The mixer was calibrated by flowing a sample of Eu nanospheres through a sheath solution of DI water. The Eu nanospheres were flowed at a constant rate of 0.1 μL/min, while the DI water sheath was flowed at rates ranging from 0.2 to 1.0 mL/min.

A cw UV diode laser emitting at 375 nm (Newport, Irvine, CA Model LQC375-16C) was used to excite the sample of flowing Eu nanospheres with less than 1 mW average power. The beam was shaped into a narrow line with a cylindrical lens and a slit and then directed into a side port of the microscope to ultimately illuminate the objective. The laser beam is focused by the objective into the central sample stream after it exits the inner capillary, and the laser excites the Eu nanospheres flowing through the mixer at a single point along their trajectory (fig. 2.5A). Downstream of this excitation point, the fluorescence of the Eu nanospheres decays with the established lifetime of 548 µs. The fluorescence of the excited nanospheres is collected back through the objective 100X oil objective (UPlanSApo, Olympus, Center Valley, PA), filtered for Eu emission at 610 nm, and directed to the camera. Images of this decay were collected for 16 different sheath volumetric flow rates.

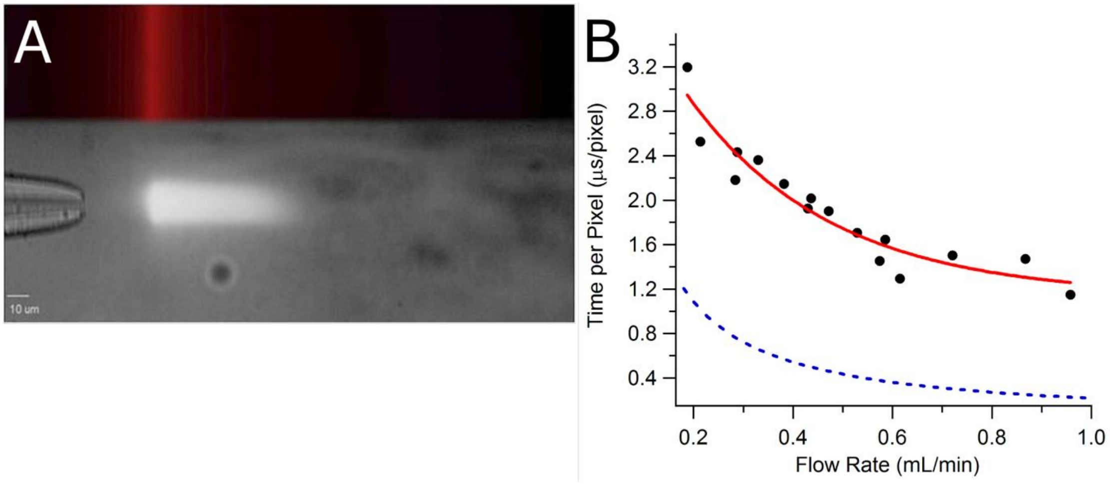

Figure 2.5: Time-per-pixel calibration. (A) Single-point laser excitation of Eu nanospheres flowing through the mixer. The top part of the image shows the excitation laser position and profile. The laser is focused to a narrow line perpendicular to the axis of sample flow. The bottom part of the image shows the nanosphere fluorescence as a white streak downstream of the line-focused laser. The nanospheres exit the inner capillary and are excited at the position of the focused laser, then as they move away from the excitation point, the intensity of their fluorescence decays at a known rate. (B) Mixer time resolution at various sheath flow rates. Experimental data (black circles) were fit to a single exponential function (red line): $\tau = 1.1 + 3.5e^{-3.5v}$. Also shown is the theoretical time resolution (blue dashes) based on equation (2.8).

For each image, a plot of Eu fluorescence intensity against pixels along the length of that image was fit with a single-exponential function from the point of laser excitation to the point at which fluorescence signal was no longer detected above background. The decay in pixels of each single exponential fit was then determined. Dividing the Eu fluorescence decay time of 548 μs by the Eu fluorescence decay in pixels for an image collected at a specific sheath flow rate gave the time resolution (time per pixel in μs/pixel) at that sheath volumetric flow rate. The linear flow velocity of the sample stream is then given by the pixel size (1.15×10^{-5} cm/pixel at 100X magnification) divided by the time per pixel. These time resolution values were plotted against their corresponding sheath volumetric flow rates in order to model the dependence of the linear flow velocity on the volumetric flow rate (fig. 2.5B). The calibration data were fit to a single-exponential function ($\tau = 1.1 + 3.5e^{-3.5v}$) where τ is the time per pixel in μs/pixel and v is the sheath flow rate in mL/min. Using this calibration, we calculate for the flow rate of 1.17 mL/min, used in the apoMb experiment described below, a time/pixel ratio of 1.2 μs/pixel. This value is near the limit of 1.1 μs/pixel predicted for high flow rates.

All time calibration values used to analyze the following results are derived from this equation. Note that the time calibration fit function is calculated for when the mixer is viewed at 100X magnification. For data collected at 40X and 60X magnification, τ is multiplied by 2.5 and 1.5, respectively, to adjust for the difference in magnification. These different magnification factors were verified using the resolution target RES-1 from Newport Corporation (Irvine, CA). The magnification factors were determined by comparing the number of image pixels spanning a given distance on the target and then calculating the pixel count ratio for each objective relative to the 100X objective.

The theoretical time calibration was calculated by assuming that the fluid flow in the mixer equals the rate of the sheath solution flow, since the sheath comprises greater than 99.9% of the total volumetric flow. The volumetric sheath flow rate is converted into a linear flow velocity using the dimensions of the flow cell and assuming a uniform flow velocity in the center of the cell. Equation (2.7) below gives the explicit expression for the time calibration, TC, in terms of the volumetric flow rate, FR (mL/min), the cross-sectional area of the outer capillary, A (cm^2), and the distance/pixel ratio, D/P (cm/pixel), which is a function of the objective being used. Equation (2.8) gives the numerical evaluation of this expression for the 200-µm diameter capillary and the 100X objective. Figure 2.5 B also displays this theoretical time calibration as a dashed line.

$$TC(\mu s/pixel) = \left(\frac{A}{FR}\right) \cdot {}^{D}/_{P} \tag{2.7}$$

$$TC(\mu s/pixel) = \left(\frac{3.14 \times 10^{-4} cm^{2}}{FR}\right) \cdot 1.15 \times 10^{-5} {}^{cm}/_{pixel} \cdot \frac{6.00 \times 10^{7} \mu s}{min} \tag{2.8}$$

This theoretical expression predicts that the µs/pixel resolution of the mixer is enhanced by using higher sheath flow rates, as the resolution should be inversely proportional to sheath flow rate. The experimentally observed behavior of the mixer deviates from this prediction in two ways. First, the time calibration data are best fit to an exponential function of FR and not 1/FR. In addition, the theoretical time calibration values are lower than the experimental ones.

The differences between the calculated and experimentally observed behaviors are likely due to theoretical assumptions that were not realized experimentally. The calculation makes the simplifying assumption that the linear flow velocity is constant along the cross section of the mixer, but we expect that there is actually a gradient of flow velocities due to drag on the capillary walls. At the interface between the sheath solution and the wall of the outer capillary, the sheath flow rate should be at a minimum due to the drag of the wall. The sheath flow rate should increase towards the center of the capillary, where drag is minimal. The linear flow velocity used in the theoretical calculation represents a weighted average of all velocities in the flow gradient and is realized somewhere between the center and edges of the outer capillary. Therefore, the position of the inner capillary within the outer capillary will determine the sheath solution linear flow velocity the sample experiences and may not be the same as the average linear flow velocity used in the calculation. Since the cross-sectional flow gradient varies nonlinearly with the volumetric flow rate, the observed linear flow velocity should not follow the expected 1/FR relationship, which explains the observed exponential relationship shown in figure 2.5. The calculations also assumed that the sample is flowing at the same rate as the sheath solution. Initially, the sample flow rate is significantly slower, but it is rapidly accelerated by contact with the sheath flow. It is possible that the two streams are not yet in equilibrium within the time of the measurements, thereby making the observed time per pixel greater than the theoretical prediction. These results emphasize the importance of experimental determination of the actual flow rate, although this is not common practice for microfluidic mixing studies.

Diffusional Mixing Time

The time required for diffusional mixing of the sheath solution with the sample stream was determined by observing the quenching of fluorescein fluorescence by potassium iodide (KI). The mixing time was determined by flowing a fluorescein sample stream through a sheath solution of KI and measuring the time required for the iodide to diffuse into the sample stream and quench the fluorescence. Fluorescein was excited at 488 nm using the filtered output of a HBO mercury short-arc lamp from Osram (Danvers, MA). Emission from the sample was transmitted through a long-pass filter and directed to the camera. All fluorescein and KI quenching experiments were performed using a 60X water immersion objective (UPlanSApo, Olympus). Fluorescein sodium salt was purchased from Sigma-Aldrich (St. Louis, MO). A solution of fluorescein was prepared by dissolving it in deionized (DI) water and then adding NaOH to the solution to reach a pH of approximately 8. The concentration of fluorescein was determined using the extinction coefficient of 80,000 $M^{-1}cm^{-1}$ at 488 nm.[94]

The diffusional mixing time indicates the time required for the sheath solution to diffuse through the cross-sectional area of the sample stream. We observe this diffusion as an exponential rate and therefore report the 1/e time of the fluorescence decay as the mixing time. A sample of 20 μM fluorescein was flowed through a sheath solution of 2.5 M KI, which quenches the fluorescence of fluorescein in a diffusion controlled reaction.[95] Images of the fluorescence quenching were collected for eight different flow rates. The fluorescein fluorescence signal across each image was fit to a single exponential function, and the decay in pixels of each function was determined. These decays were multiplied by the appropriate time resolution value, based on the sheath flow rate that was used, to obtain a mixing time. We considered time zero as the point where the sample and sheath solutions were first able to mix, so in this setup this is the end of the inner capillary. The reported mixing times are times from the end of the inner capillary. Figure 2.6 illustrates the mixing times plotted against their corresponding sheath flow rates. The data demonstrate a decrease in mixing time as sheath flow rate increased. The data were fit to a single exponential function ($\tau_{mix} = 82 + 530e^{-3.0v}$) where τ_{mix} is the 1/e mixing time and v is the sheath flow rate in mL/min. The fit indicates a minimal diffusional mixing time of 82 μs for iodide that can be achieved at the highest sheath flow rate. Iodide has a relatively slow rate of diffusion, so we expect that shorter mixing times may be achieved with smaller, faster diffusing solutes. A mixing time of 98 μs is calculated for the flow rate of 1.17 mL/min used in the pH jump experiments with apoMb described below. The decrease in mixing time as flow rate increases shown in figure 2.6 is likely due to increased hydrodynamic focusing of the sample at higher sheath flow rates and constant sample flow rate. As hydrodynamic focusing increases, the width of the sample stream decreases. The distance through which a solute in the sheath solution must diffuse in order to mix with the sample effectively decreases as the sheath flow rate increases, allowing diffusion to occur more rapidly.

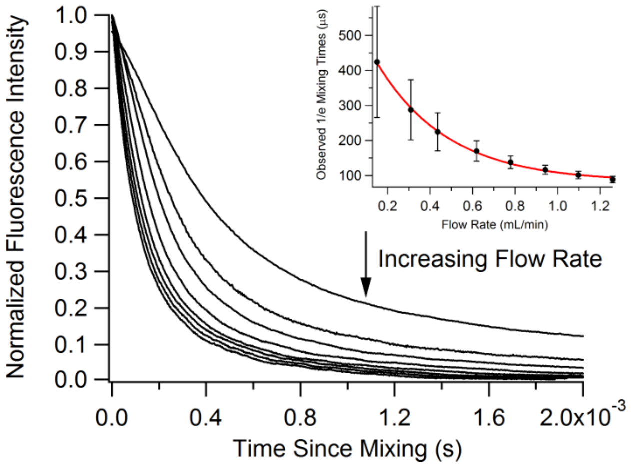

Figure 2.6: Mixing time calibration. Fluorescence transients from the quenching of fluorescein fluorescence by mixing with potassium iodide at different sheath flow rates. Inset shows the observed mixing times as determined by exponential fits. Inset data were fit to a single exponential function: $\tau_{mix} = 82 + 530e^{-3.0 \cdot v}$.

The mixing times determined for our mixer are faster than many protein structural dynamics, thus making continuous flow mixing a viable approach to initiate fast protein events, including enzymatic catalysis and protein folding. It is also reasonable to expect that mixing experiments that use a pH change might have a faster mixing time than we report here because protons diffuse faster due to their small mass and additional transport mechanisms like the Grotthuss mechanism.[96] However, for the pH jump experiments described here, similar mixing times are observed (verified by pH quenching of fluorescein under the same conditions as the protein experiment) despite the two orders of magnitude increase in diffusion rate of protons compared to iodide. The reason for similar mixing times is that the increase in diffusion rate is negated by the comparatively low concentration of protons available at pH 2, more than two orders of magnitude lower than the iodide concentration in the calibration experiment.

ApoMb Unfolding Kinetics

To verify the utility of this mixing device, we studied the unfolding kinetics of Apomyoglobin (apoMb). ApoMb is an important model system for the study of protein folding mechanisms. The protein consists of only 153 amino acids organized into 8 alpha helices labeled A-H.[97] Several studies have demonstrated that the protein adopts four unique conformational states, depending on solution conditions: the native form (N), the intermediate form (I), the extended form (E), and the unfolded form (U).[98-101] These distinct equilibrium conformations of apoMb have also been observed as kinetic intermediates in T-jump and fast mixing studies.[100, 102-105] All of these states can be accessed in equilibrium by changing the pH and ionic strength of the protein solution. During acid denaturation, apoMb has been shown to transition between its structural states in two distinct folding events. At pH 7, apoMb exists in its N form. Between pH 6 and 4, the protein unfolds from its N form to its I form due to the protonation of the imidazole side chains of three histidine residues (His24, His64, and His113).[106] An additional expansion of apoMb's structure from its I form to E form can occur at pH 3 when the salt concentration of the protein solution is low.[102] Below pH 3, the protein completely unfolds to its U form as the carboxyl groups on the side chains of a glutamate (Glu6) and an aspartate (Asp122) are protonated.[106]

We used the fast mixer to study the unfolding kinetics of apoMb initiated by a rapid pH drop. The pH drop was induced by flowing apoMb through a sheath solution of HCl and the reaction was probed using the fluorescence of 1,8-ANS bound in the heme pocket of the protein in a 1:1 molar ratio.[107] The apoMb sample was at a pH of 4.5, and the HCl sheath was at a pH of 2.0. The diffusion of protons from the flowing sheath solution into the apoMb sample stream lowered the pH of the protein solution to pH 2.0, causing the apoMb to unfold and therefore the 1,8-ANS fluorescence to be quenched. The unfolding lifetime of apoMb is determined from the time dependence of the 1,8-ANS fluorescence quenching. Equilibrium measurements have previously shown that under the initial conditions employed in the present study of minimal salt and pH 4.5, apoMb is in the I form, a partially folded intermediate state with a native-like AGH core. When the pH drops to 2.0, apoMb unfolds to its U form, having very little residual structure.[102] Hence we expect the pH jump to initiate the unfolding transition from I to U under conditions that strongly favor the completely unfolded state U.

Equine skeletal muscle myoglobin was purchased from Sigma-Aldrich. A solution containing 5 mg of protein/mL of deionized water was prepared. Myoglobin was precipitated from this solution by adding ammonium sulfate to 68% saturation at room temperature. The sample was dialyzed overnight against deionized water using regenerated cellulose dialysis tubing from Fisher Scientific (Pittsburg, PA). ApoMb was prepared from this sample according to a modification of the procedure of Adams.[108] In this modification, the diethyl ketone extraction and dialysis were performed twice to improve sample purity. In addition, apoMb was dialyzed against deionized water only. The concentration of apoMb was determined using the extinction coefficient of 15,570

$M^{-1}cm^{-1}$ at 280 nm.[108] 1,8-ANS was also purchased from Sigma-Aldrich. A solution of 1,8-ANS was prepared by dissolving the compound in DI water. The 1,8-ANS solution was added to apoMb to make samples with a 1,8-ANS:apoMb concentration ratio of approximately 1:1. The concentration of 1,8-ANS was determined using the extinction coefficient of 5000 $M^{-1}cm^{-1}$ at 350 nm.[109]

The unfolding lifetime of apoMb was measured at five different sheath flow rates as shown in figure 2.7. In principle, the observed lifetime should be independent of the sheath flow rate provided that it is significantly longer than the effective mixing time. Control experiments compared the apoMb-1,8-ANS fluorescence images for a sample stream flowed through DI water (no pH change) at these five flow rates. We found that the fluorescence signal for the control experiment in DI water decreases along the sample stream as it is hydrodynamically focused by the sheath flow. When the sample stream is focused, there are fewer molecules in the excitation volume of the imaging system, resulting in an apparent decrease in the total fluorescence signal. This effect is removed from the pH jump data by dividing the fluorescence image of an HCl experiment by the image of the reference DI water experiment at the same flow rate. This method yields a corrected 1,8-ANS fluorescence quenching profile. A similar approach was applied by Hertzog and coworkers to analyze fluorescence decays in a different microfluidic flow system.[65] Each fluorescence quenching profile was fit to a single exponential to determine the profile's decay in pixels. Each decay was then converted to an unfolding lifetime by multiplying by the appropriate flow dependent time resolution. The dependence of the observed unfolding lifetime on the sheath flow rate (fig. 2.7) can be understood in terms of the inverse relationship between sheath flow rate and mixing time due to hydrodynamic focusing of the sample stream. At slow sheath flow rates, the mixing time is slow and it overlaps with the unfolding time, yielding an apparent lifetime that is slower. As the sheath flow rate is increased, the apparent lifetime increases until it reaches the limiting value of 760 ± 8 μs and becomes independent of flow rate. At this point the mixing time is less than 100 μs, meaning it no longer perturbs the observed unfolding time. We conclude that the observed decay time of 760 ± 8 μs at the fastest sheath flow rates represents the actual lifetime of the pH induced transition from the I to U form of apoMb.

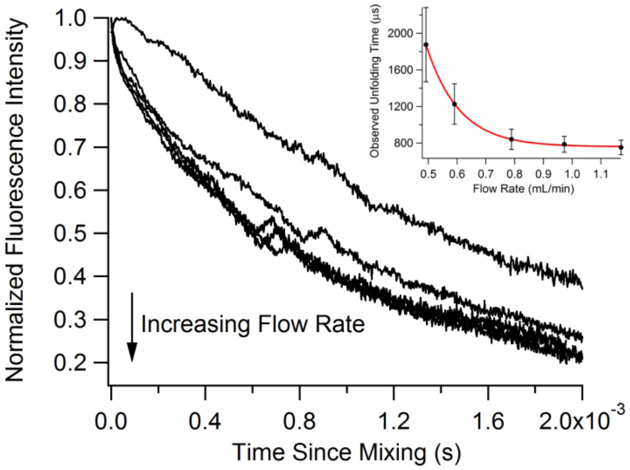

Figure 2.7: pH-induced unfolding of apoMb. Fluorescence transients from the rapid change in pH of apoMb from 4.5 to 2.0 are shown at various flow rates in the large image. Inset shows apoMb unfolding times as determined by exponential fits. The unfolding time decreases according to an exponential function: $\tau_{unf} = 760 + 80000e^{-8.8 \cdot v}$. The baseline indicates a flow rate independent unfolding time (I ↔ U) of 760 ± 8 μs.

The unfolding mechanism of apoMb has been studied by many different methods, including T-jump, rapid mixing and H/D exchange.[98-99, 103, 105, 110-113] The consensus of previous work is a multi-state unfolding mechanism:

Scheme 2.1

$$N \leftrightarrow I \leftrightarrow E \leftrightarrow U$$

The earliest intermediate in the folding reaction, the E state, consists of a hydrophobically collapsed chain stabilized by packing of the nearly fully formed A, G and H helices to make a core structure. The formation of this state was not resolved in early stopped flow and continuous flow experiments, but rather was observed as a burst phase.[111, 113] T-jump IR measurements, however, observed sub-millisecond relaxation lifetimes for the E state.[103] The I state has been observed both as a kinetic intermediate in refolding experiments at pH 6[112] and also as an equilibrium intermediate at pH 4.2-4.5 and high ionic strength (20 mM NaCl).[102] It resembles the E state, having a folded AGH core, but it also has the fully folded B and E helices. A recent study measured the rate of urea induced unfolding of sperm whale apoMb starting from the I state at pH 4.2 (labeled "M" by the Roder group), using a turbulent flow mixer with similar time resolution to the present work.[105] This study postulated an additional state "L" between I and E to account for the observed kinetics and reported an overall unfolding lifetime (I ↔ L ↔ E ↔ U) at pH 4.2 extrapolated to zero urea concentration of 1.5 ms. We find a significantly shorter unfolding lifetime (760 μs) at pH 2 and no urea. More importantly, we find that the unfolding reaction under these conditions does not populate any intermediates, but rather can be modeled as a simple two-state process (I ↔ U).

We emphasize that the rapid pH jump achievable in our continuous flow mixer enables the investigation of the unfolding kinetics of apoMb on a previously unexplored part of the energy landscape. At pH 2 and low salt, apoMb unfolds in a highly cooperative, all or nothing transition that does not populate intermediate states. This result means that the “E” and “L” intermediates are not obligatory and that it is possible for the protein to unfold through a more direct route under highly destabilizing conditions that impose a large driving force for the unfolding reaction. Alternatively, it is possible that the protein still unfolds through the same intermediates observed at pH 4.2, but they are not populated to any great extent under these conditions due to differences in the activation barriers. One other difference worth noting is that the while the horse protein used in the present study has considerable sequence identity (88%) to the sperm whale protein, and while overall folding behavior of the two forms is similar, some subtle differences have been observed.[114] These differences are small, however, and are unlikely to cause a change in the unfolding mechanism by themselves. Furthermore, the observation of two state unfolding of I to U is not unprecedented, since Baryshnikova *et al.* found that unfolding of apoMb starting in the native state N proceeds through a single intermediate state I (N ↔ I ↔ U) under strongly denaturing conditions.[115] Thus it is possible to effectively bypass the L and E intermediate states under conditions that strongly destabilize the folded structure.

Conclusions

We have demonstrated the utility of a new continuous flow rapid mixer for the study of protein dynamics. The mixer has a robust design that is easy and inexpensive to implement and allows rapid recovery from clogs. The mixer utilizes 3D, hydrodynamic focusing of a sample solution by an all-encompassing sheath solution in order to achieve rapid diffusive mixing between the sample and sheath. Characterization of the mixer’s performance was conducted completely via experimentation, rather than simulation. The mixer achieves a minimum time resolution of 1.2 μs/pixel at sheath flow rates above 1 mL/min. Flowing the sample at a rate of 0.1 μL/min minimizes its consumption. At a sheath flow rate of 1 mL/min, diffusive mixing of small molecules from the sheath into the sample is accomplished in under 100 µs. This fast mixing time is sufficient to resolve the unfolding kinetics of apoMb from its I form (pH 4.5) to its U form (pH 2.0) with an unfolding time of 760 ± 8 µs. This reaction occurs as a single cooperative transition, without populating intermediates, unlike its behavior in the presence of denaturants at higher pH. The rapid pH jump made possible by the continuous flow mixer allows access to a part of the folding energy landscape of apoMb not previously explored. These results demonstrate the applicability of this rapid continuous flow mixer to the study of protein dynamics in general, including enzymatic catalysis. Complete optical access is available to the entire mixing region, and it is possible to use UV excitation of intrinsic fluorophores (280 nm excitation of tryptophan) or extrinsic labels. The extension of possible probe wavelengths deeper into the UV substantially expands the applicability of fast mixers. Moreover, the mixer is simple enough to construct and operate in any biophysical chemistry laboratory. This ease of access and usage is a substantial advantage over similar devices, which have comparable experimental mixing times but are more complicated to operate.[59, 100, 116] We expect these advances to lead to more widespread application of this methodology to the study of biomolecular reactions.

Chapter 3. Lactate Dehydrogenase

Section 3.1 Introduction to Lactate Dehydrogenase

Lactate dehydrogenase (LDH) is an oxidoreductase enzyme that catalyzes the oxidation of lactate to pyruvate. This process can is mediated by a NAD+ cofactor in our studies but may use other cofactors depending on the particular enzyme. LDH is also either specific to the L- or D- form of lactate. These enzymes, regardless of class, are utilized during metabolism to convert pyruvate to lactate when sufficient oxygen is not present in animals. Then at a later time when the organism is less stressed, the enzyme converts lactate back to pyruvate to be used in other metabolic pathways. Different isoforms of the enzyme are present which are biased toward one side of this reaction or the other.[117-118] In animals, three major isoforms exist – heart, muscle, and sperm – so named due to where they are the dominant isoform. LDH naturally forms a multimer in solution made up of a combination of the heart and muscle except in the testes where only the sperm isoform is expressed. These formulations are tuned depending on the needs of a particular tissue or organ.[119] All of the experiments using LDH described below utilize pig heart (L-lactate) LDH. Figure 3.1 summarizes the reaction scheme for pig heart (L-lactate) and shows the relevant structures.

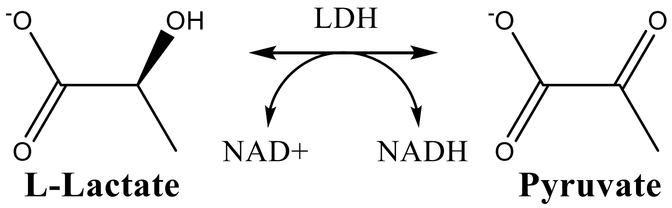

Figure 3.1: Reaction scheme for pig heart (L-lactate) LDH.

Pig heart (L-lactate) LDH is composed of four subunits of the porcine heart LDH isoform. It is strongly biased toward lactate formation, the K_{eq}, with pyruvate considered as the product, is 2.5 x 10^{-12} M.[88] It utilizes NAD+ as its cofactor during the oxidation of lactate. We chose to work with pig heart LDH because of it wide commercial availability and because it has previously been well studied as a model system.[32, 86, 120] Upon binding of substrate and cofactor, a substantial conformational change occurs in the enzyme. The new conformation is required so as to correctly setup all the electrostatic interactions required to align and polarize the substrate and cofactor for chemistry.[121] The motion that is most relevant to our work is the movement of a surface loop structure. This loop is a short sequence of 12 amino acids (residues 98-110 in our subject) which serves two key roles in LDH catalysis. Its first role is to provide stabilizing hydrogen-bonds to the carbonyls of pyruvate from an appropriately arranged arginine (R109) residue. The loop position is shown in figure 3.2A and the layout of the active site interactions is shown in figure 3.2B. Its second role is more representative of a general role of enzymatic loop motions in that it acts like a protective cover for the active site. This cover both isolates the active site from solution and stabilizes the substrate while catalysis happens.[122-123] Figure 3.3 shows the extremes of the loop movement from crystal structures of a structurally similar LDH. The movement of this loop happens on the millisecond timescale and is believed to be the rate limiting step of catalysis.[123] Therefore, understanding this loop motion is critical to understanding how the enzyme functions. Furthermore, due to the dynamic nature of the loop and its function, it is necessary to use kinetic techniques to investigate the loop. Our studies utilizing temperature-jump spectroscopy and rapid mixing are detailed below.

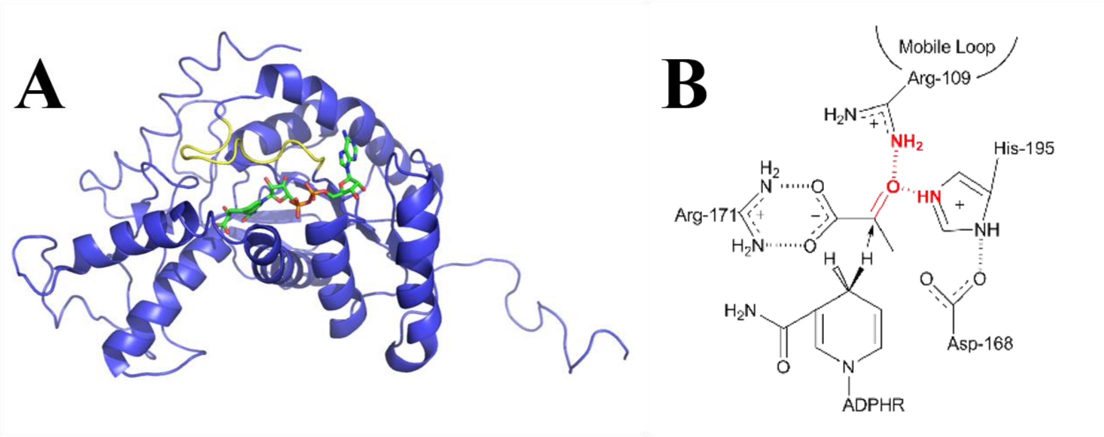

Figure 3.2: Structure of pig heart LDH. Panel A is a cartoon representation from PDB ID 5LDH. The surface mobile loop is highlighted in yellow and the cofactor-substrate complex is shown as a stick structure in green. Panel B shows the active site configuration when the loop is closed. The catalytically key surface loop (residues 98-110) closes over the active site, bringing residue Arg109 in hydrogen bond contact with the ligand, forcing water to leave the pocket and, accompanied by the motions of mobile areas in the protein, rearranges the pocket geometry to allow for favorable interactions between the cofactor and the ligand that facilitate on-enzyme catalysis. Of particular relevance to sections 3.3 and 3.4 are the hydrogen bonds formed between Arg-109 and His-195 to the C2 carbonyl of pyruvate (emphasized in red). These bonds dictate the polarity of the carbonyl when pyruvate is bound.

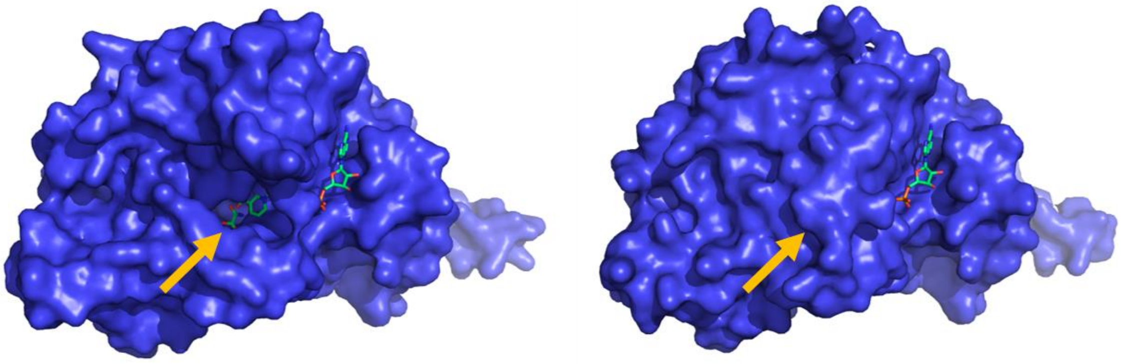

Figure 3.3: Space-filling model of LDH. Its loop is shown in the open (left) and closed (right) states. The yellow arrow points to the active site that gets covered up when the loop closes. The cofactor-substrate complex is shown as a stick structure in green. The images are from the PDB structures 6LDH and 1LDM of dogfish muscle LDH in its apo and tertiary forms.

Section 3.2 Summary of Previous Catalytic Models

The simplest model that can be applied to the LDH catalytic cycle given the information about the loop dynamics presented above is a modification of the Michaelis-Menten model. In this model we label the encounter complex as the loop open state and the Michaelis state as the loop closed state. See scheme 3.1. This scheme assumes that the loop opening for product release and product release occurs at the same time. For the sake of simplifying this discussion we will ignore the binding of cofactor to the enzyme as it should generally happen prior to substrate binding, and the binding order should not affect the timing of the loop motions.

Scheme 3.1

$$LDH \bullet NADH + Pyruvate \leftrightarrow LDH \bullet NADH \bullet Py^{Open} \leftrightarrow LDH \bullet NADH \bullet Py^{Closed}$$
$$\leftrightarrow LDH \bullet NAD^{+} + Lactate$$

Even in early kinetic studies of LDH this scheme was found to be insufficient. For example using the transition-state mimic oxamate (fig. 3.4), McClendon et al. were able to use fluorescence temperature-jump spectroscopy to investigate the loop motion. They took advantage of the natural fluorescence of NADH for their optical probe. The fluorescence efficiency of NADH changes depending on the enzyme state. Their data were reasonably complex enough that they proposed a second encounter complex that was still characterized by an open loop.[124] Oxamate (fig. 3.4) is used to simplify studies of LDH as it is believed to bind similarly to pyruvate but is not catalytically active allowing for investigation of pre-chemistry catalytic events.

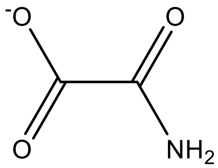

Oxamate

Figure 3.4: Chemical structure of oxamate.

This work was followed up by the same lab in collaboration with the Dyer group by switching their optical probing method to infrared absorbance.[125] The advantage of using a vibrational method, like infrared absorbance, over fluorescence spectroscopy is the direct connection between infrared observables and particular molecular structures. With fluorescence methods, a connection between signal changes and particular structures is less clear. In this study, Deng et al. probed the carbonyl stretches on each of the carbons of oxamate separately. They expected to see significant changes in the vibrational mode of these stretches upon binding to and conformational motion of the enzyme because these events stabilize the carbonyl bonds inside a rigid electrostatic configuration (see section 3.1). In equilibrium studies, upon binding of oxamate to LDH•NAD+ they saw the vibrational band of these carbonyl bonds both sharpen up and split into two different bands. The appearance of two bands indicates that the existence of two distinct subpopulations of oxamate in the enzyme. Furthermore, the sharpening of the bands indicates that the number of subpopulations observed has been significantly reduced. Their original interpretation of this data was in line with scheme 3.1, the two new bands corresponded to the encounter and Michaelis complexes as these are the only other states with pyruvate present; however, their kinetic results indicate something else.

When observing the response to temperature of the C_2 carbon, the carbon where chemistry happens, their results indicated heterogeneous kinetics between the two infrared bands. Both the signal intensity and signal timing was different between the two bands. If a model like scheme 3.1 was correct and their interpretation of these bands as the encounter and Michaelis states was correct, then the kinetic results should mirror one another in both intensity and timing with perhaps slight variations due to some minor additional binding/unbinding from the encounter complex. This contradiction in their analysis led them to propose a new state; however, this state was not a pre-encounter complex open loop state as from their original work with fluorescence. The new state was a second closed loop state, a second encounter complex. Based on the discrepancy in signal intensity they also assigned one of the states to be a major state, where most loop closures lead, and the other as a minor state. This mechanism is summarized in scheme 3.2.

Scheme 3.2

$$LDH \bullet NADH + Substrate \quad \leftrightarrow \quad LDH \bullet NADH \bullet Sub^{Open} \quad \begin{matrix} \leftrightarrow \\ \leftrightarrow \end{matrix}$$

$$\begin{matrix} LDH \bullet NADH \bullet Sub^{Closed-Major} \\ LDH \bullet NADH \bullet Sub^{Closed-Minor} \end{matrix}$$

Of course, the results from these series of experiments are not fully satisfying because they are not using a chemically competent reaction mixture. This leads to some questions about scheme 3.2. Are both the major and minor complexes catalytically competent? If both are competent, do they proceed at the same rate? Does the loop positioning define the major and minor complex? In their next paper, the Callender lab worked toward answering some of these questions by returning to fluorescence-probed temperature jump spectroscopy using pyruvate instead of oxamate.[88] To establish an equilibrium where species of both the pyruvate and lactate sides of the equation were present they had to do the work with a large excess of lactate (see the K_{eq} indicated at the beginning of the chapter). Under these conditions they were able to simultaneously probe all the substates in the LDH equilibrium. Although useful, this detail further complicated the analysis of the temperature-jump data and required computational modeling to understand the observed relaxation rates. The conclusions from modeling of the relaxation data showed no heterogeneity, like the infrared experiment, and also did not show a second encounter complex like their fluorescence experiment with oxamate.[88, 124-125] This leads back to a mechanism like that presented in scheme 3.1.

These results do not preclude the existence of enzymatic heterogeneity; there are other possibilities to explain the discrepancies. As described before, the use of infrared as the probing method is generally more sensitive than fluorescence especially because they were able to directly probe the enzyme substates. It is possible that the fluorescence experiment on the active system did not indicate heterogeneity because the probing method was not sensitive enough. Furthermore, as indicated above, interpreting the active experiment is necessarily more complicated than interpreting the inhibited complex because of the existence of more states and reaction pathways. The modeling that was done to interpret the live system experiments was not entirely rigorous and could lead to misinterpretation of the data. From our review of previous kinetic catalytic models, it was clear that more work needed to be done to understand LDH and its loop motions. To add to this investigation we proceeded to design experiments that would address the issues complicating analysis listed above. Three approaches were taken.

First, we performed temperature-jump studies on the active LDH system utilizing infrared absorption as our probe method to gain substate sensitivity. We present this data in section 3.3. Second, to interpret the infrared temperature-jump data we develop a novel computational modeling method that is both rigorous and discerning. We explain both the method and its insights when applied to this problem in section 3.4. Finally, utilizing fast mixing to initiate the oxamate and pyruvate reactions instead of temperature-jump spectroscopy we were able to study the LDH reaction with only a few of its states present thereby simplifying analysis. This is described in section 3.5.

Section 3.3 Infrared Temperature-Jump Experiments with LDH

The work presented here as sections 3.3 and 3.4 has previously been published as one journal article. The article is adapted with permission from reference [126]. Copyright 2014 American Chemical Society. It is reproduced here in a modified format to allow for a thorough description of our studies of lactate dehydrogenase.

Using infrared absorption as a probing method with the LDH•NADH•oxamate complex yielded results that indicated heterogeneity within the prechemistry steps of the LDH reaction.[125] Therefore, to further examine heterogeneity in the live chemically competent system, we used infrared absorption to study this system as well. Using infrared absorption to probe the enzyme equilibrium will give us a higher molecular resolution than using fluorescence. Due to technical considerations, including high water infrared absorbance and the lack of infrared-compatible materials for flow studies, these kinetic experiments must be done using the temperature-jump method described in section 2.2.

Infrared absorption is an optical probing method that depends on the excitation of vibrational modes within a molecule. A full review of vibrational spectroscopy is outside the realm of this work, but many good reviews exist.[127-130] In short, we have utilized mid-infrared frequencies to perform absorption experiments. Specifically, we have used frequencies from 1600-1750 cm^{-1} to probe the carbonyl stretching modes of pyruvate. A complication of working in this region is that the solvent, water, and the protein backbone of the enzyme absorb strongly at these frequencies. We can reduce the water absorption in the sample by switching from working in H_2O to D_2O. With the additional weight of a couple extra neutrons the vibrational modes become in resonance at lower frequencies. This shift is enough to significantly reduce the infrared extinction coefficient so that we can still work in this region. This approach has been utilized previously.[76, 131] The amide I band of the protein background is due to the carbonyl groups in the protein backbone.[132-134] Since we are also concerned with a carbonyl mode, it is not surprising that there would be overlap with our signal of interest. To get around this problem we will use protein constituted from 13C and ^{15}N labeled amino acids. Generating the labeled protein is done by growing *E. coli* cells expressing LDH in minimal media with ^{13}C-glucose and ^{15}N-ammonium chloride. A full description of this process has been discussed elsewhere.[135] As with the D_2O solution above, the added molecular weight shifts the amide I band down in frequency enough so as to not be a major problem for our studies.

A further technical adjustment that has to be done to make this experiment work is the use of difference methods. Difference methods depend on the idea that spectroscopic signal are often additive. This implies that if you have a sample composed of two parts, AB, where each component generates a signal independently, Signal_A and Signal_B that the total signal for AB is $\text{Signal}_A + \text{Signal}_B$. When this is true you can look at the signal of just one component by literally subtracting out the independent spectrum of the other component from the total signal, $\text{Signal}_A = \text{Signal}_{AB} – \text{Signal}_B$. This is useful when dealing with complex reaction mixtures because it allows us to subtract out the signals of the mixture that we are not interested in studying. A good review of applying difference methods to biological samples using Raman spectroscopy is available by Deng and Callender.[136] Applying this method to our studies with LDH, we can take the spectrum of the enzyme-substrate ternary complex (LDH•NADH•pyruvate) and subtract out the enzyme ternary complex with isotopically-labeled pyruvate (LDH•NADH•$^{13}C_2$-pyruvate) to see changes in the infrared absorption signal that are only related to carbon-2 of pyruvate.

FTIR Spectroscopy

Static FTIR spectroscopy was carried out on a Magna 760 Fourier transform spectrometer (Nicolet, Instrument Corporation, Madison, WI) using an MCT detector as described previously.[125, 137] Infrared cells consisted of CaF_2 windows with 15 µm Teflon spacers. Spectra were collected in the range of 1100-4000 cm^{-1} with 2 cm^{-1} resolution. A Blackman-Harris three-term apodization and a Happ-Genzel apodization were applied respectively. Omnic 4.1a (Nicolet Instruments, Corp.) software was used for data collection and analysis. All samples were prepared in D_2O buffer with 100 mM phosphate at pH 7.2 (pH meter reading). The LDH reaction mixture was prepared at the initial concentrations of 4:4:20 mM (LDH•NAD^+•lactate, where LDH concentration refers to active sites). Under such conditions, about half of the NAD^+ was converted to

NADH, yielding an on-enzyme pyruvate concentration of about 2 mM as determined by UV-Vis measurements.[138] This high level of protein concentration is required to be able to see the weak signal of the carbonyl bond of interest as each protein active site will only contribute one carbonyl bond. We saw no evidence of protein aggregation in the infrared measurements at these concentrations. Additionally, we performed temperature-dependent FTIR measurements on this same reaction mixture. The sample cell was in thermal contact with the stage. The temperature of the stage was controlled by a water bath. Collection of spectra and temperature control were automated by Labview (National Instruments, Austin, TX) routines written in our lab.

Figure 3.5 displays the infrared isotope edited difference spectra of LDH-bound pyruvate at 5, 15, 25, and 35 °C. The difference spectra were generated by subtracting the protein bound [2-^{13}C]pyruvate spectra from the protein bound [2-^{12}C]pyruvate spectra at each temperature. The resulting difference spectra report only on the infrared bands that are affected by the label; therefore, these IR difference features report directly on the reactive carbonyl bond involved in the catalytic turnover. The [2-^{12}C]pyruvate carbonyl stretches are the positive bands in the spectrum whereas the [2-^{13}C]pyruvate carbonyl stretches would appear as negative bands at lower energy (not shown).

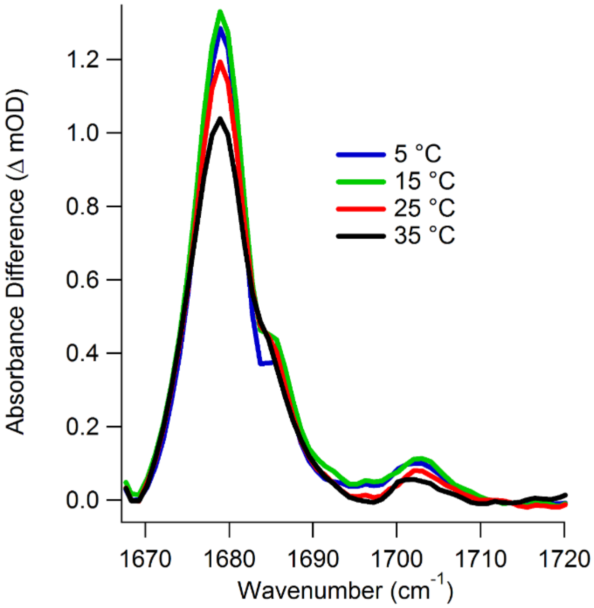

Figure 3.5: Isotope-labeled difference FTIR spectra of LDH•NADH•pyruvate. The spectra are processed as [U-^{15}N,-^{13}C]LDH•NADH•[2-^{12}C]pyruvate minus [U-^{15}N, -^{13}C]LDH•NADH•[2-^{13}C]pyruvate at the indicated temperatures.

The ^{12}C2=O stretch IR spectrum of bound pyruvate is heterogeneously broadened. Gaussian fits to the spectrum reveal several sub-bands that we assign to different enzyme-bound pyruvate conformational substates.[137] A reasonable fit of the data was produced by the sum of four Gaussian sub-bands with center frequencies at 1674, 1679, 1686, and 1703 cm^{-1}; although, we cannot rule out the possibility that each of these bands could be composed of more than one overlapping substate. There is also the likelihood of sparsely populated substates that are not apparent in the IR difference spectra due to limited sensitivity.[139] Two observations illustrate that the substate distribution is temperature-dependent. First, all band intensities tend to decrease as the temperature is raised. This indicates the population shifts way from bound pyruvate to either free pyruvate or to the product side (bound or free lactate) at higher temperature. The IR difference spectra do not allow us to track the lactate population directly, because upon conversion to lactate the C2 carbonyl infrared stretch is lost and the corresponding lactate vibration is not observed in this spectral region (it is at lower frequency and obscured by protein absorbance). The second observation is that a new equilibrium is established amongst the substates when comparing the lowest temperature spectrum to higher ones. This trend is visible by comparing the more dramatic decrease in absorption at 1679 cm^{-1} to the minimal decrease in absorption at 1674 and 1686 cm^{-1}. Therefore, changing temperature is a viable method for disturbing the LDH equilibrium and can be used to study the dynamics of this redistribution.

Temperature-Jump Kinetics

The relaxation times for establishing new equilibria amongst the IR detected substates and the product states were determined by laser-induced temperature jump relaxation spectroscopy employing IR probes at infrared frequencies representative of each of the substates noted above. T-jump IR spectroscopy was performed with a previously described setup.[86, 140] Briefly, a 1.91 µm pump beam is produced by the 1st Stokes shift of the fundamental line from a Nd:YAG laser (30 mJ/pulse, 10 Hz repetition rate, 10 ns pulse width, Spectra Physics, Mountain View, CA) pumping a H_2-filled Raman shifter. The 1.91 µm pump beam is absorbed weakly by the combination bands of the D_2O solution allowing for near uniform heating of the solution. The heated region is probed by a quantum cascade laser (Daylight Solutions Inc., Poway, CA) tunable from 1565-1723 cm^{-1}. Changes in probe beam transmission are detected by a fast (200 MHz) photovoltaic MCT detector (Kolmar Technologies, Newburyport, MA) and the signal is filtered and amplified in a low noise preamplifier (SR560, Stanford Research Systems). Typically, 10,000 pump-probe events are averaged for each probe frequency of interest.

The sample cell path length was 200 µm. Temperature jumps of 8 and 15°C were employed in this study. A consistent final temperature of 30 °C was used so that all results were reporting on the same thermal equilibrium. The useful time range of the instrument used in this study is from ten µs to one ms. The lower limit of this range is set by the bandwidth of the preamplifier. The geometry of our cell arrangement is such that heat diffuses out of the irradiated volume with a lifetime of a few ms; this determines the duration of the T-jump and thus sets an upper limit to the useful time range.

We used a probe frequency of 1710 cm^{-1} to study the free pyruvate population as well as 1704, 1685, 1679, and 1670 cm^{-1} to study the 1703, 1686, 1679, and 1674 cm^{-1} protein-bound pyruvate bands, respectively, under an assumption of one substate for each probe frequency. Although it is possible, and probably likely, that there are more than these five pyruvate substates present and contributing overlapping signals this is the minimum number of states that can fit our equilibrium data. At the probe frequencies used to study the bound pyruvate substates, we can safely assume that the dominant contributor to each spectroscopic signal is the assigned substate from equilibrium. Using the fitting parameters presented previously for the FT-IR data,[137] we can estimate the relative contribution of each of the substates to a given probe frequency. This analysis suggests that the probe frequencies are dominated by the assigned substate in a range of 75 – 100 % contribution.[126]

Figure 3.6 shows the relaxation transient at each probe wavelength from ten µs to one ms. The data presented in the figure represent jumps of the sample to the same final temperature, 30 °C, but different initial temperatures. 30 °C is a good final temperature to use because it yields the largest change in the ^{12}C2=O stretch infrared signal from any of the lower temperatures (fig. 3.5). The 1710 and 1704 cm^{-1} IR transients were obtained with a jump from an initial temperature of 15 °C. The other three probe frequencies had an initial temperature of 22 °C. The initial temperature determines the initial populations of the various states, whereas the final temperature has a direct effect on the relaxation kinetics, depending on the activation energies. The difference in the initial temperatures affects the amplitude of the transients, scaling to a good approximation as the size of the temperature jump. Therefore, the transient relaxation lifetimes for jumps to the same final temperature are comparable directly, but comparison of the magnitude requires adjustment to the size of the T-jump. Beyond 1 ms, the solution begins to cool and it is not possible to separate further changes in the IR signal due to the enzyme dynamics from the cooling induced changes. The relaxation transients are all well fit to a single exponential function as shown in figure 3.6, except for the 1704 cm^{-1} data. A double exponential function is required to achieve a reasonable fit of the 1704 cm^{-1} transient. The fit lifetimes are provided in table 3.1.

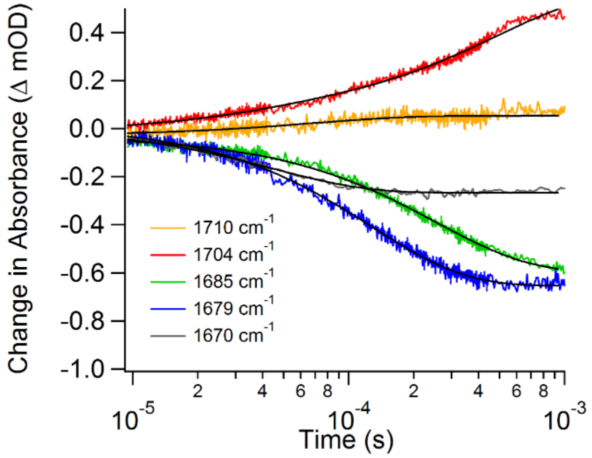

Figure 3.6: Isotope-labeled IR difference temperature-jump transients. The relaxation data are processed as [U-^{15}N, -^{13}C]LDH•NADH•[2-^{12}C]pyruvate minus [U-^{15}N, -^{13}C]LDH•NADH•[2-^{13}C]pyruvate at the various probe frequencies. Each probe frequency is plotted as a different color as specified in the legend, and the exponential fits are plotted as black lines.

Table 3.1: Exponential Fit Lifetimes for LDH Temperature-Jump Data

Probe Frequency	**Experimental Relaxation Lifetime**	**Simulation Relaxation Lifetime (see section 3.4)**
1710 cm^{-1}	69 ± 6 µs	63.6 ± 0.6 µs
1704 cm^{-1}	33 ± 3 µs (14 %)[a]	332.0 ± 0.6 µs
	480 ± 20 µs (86 %)[a]	
1685 cm^{-1}	254 ± 3 µs	245.6 ± 0.6 µs
1679 cm^{-1}	128 ± 1 µs	134.0 ± 0.4 µs
1670 cm^{-1}	44.2 ± 0.6 µs	93.81 ± 0.04 µs

[a] Percent contribution of the phase to the overall fit.

The 1685, 1679, and 1670 cm^{-1} transients each show a negative amplitude signal with a sub-millisecond relaxation lifetime that depends on the probe frequency; the fit lifetime decreases as the probe frequency decreases. The relaxation time is dominated by the chemistry step (see kinetics modeling work in section 3.4); consequently the rate of the hydride transfer is inversely correlated with the frequency of the C2 carbonyl stretch (the rate increases as the frequency decreases). Because the C2 carbonyl stretch frequency is directly related to the bond strength, or the polarization of the bond, it correlates with the reactivity towards hydride transfer. Such a correlation is consistent with previous studies relating the frequency of the C2 carbonyl vibration to the rate of enzymatic turnover.[121-122, 141] Previous studies generated a series of mutations of LDH from *B. stearothermophilus* to alter the hydrogen bonding network at the active site. Isotope edited Raman spectroscopy was used to determine the effect of these mutations on the frequency of the C2 carbonyl stretch and thus how the altered hydrogen bonding affects the polarity of the C2 carbonyl. These studies concluded that an increase in the polarity of the bond is directly correlated to an increase in the hydride transfer rate.[121]

The present work is a more direct observation of the relationship between carbonyl bond polarity and the rate of hydride transfer because it compares different conformations of the same enzyme. The transients observed for the substates probed by 1685, 1679, and 1670 cm^{-1} depend on the rate of chemical transition from pyruvate to lactate. This conclusion is also consistent with the observation that in the equilibrium measurements this cluster of infrared bands has the lowest stretch frequency, highest polarity, and therefore it represents substates closest to forming lactate. Importantly, the amplitudes of these transients are all negative, indicating a decrease in population of the substates, due at least in part to shifting the equilibrium towards lactate. Furthermore the substate transients are independent in time, and there is no evidence of correlated changes expected for direct interconversion of one substate to another. Specifically, if substate A is directly converted to substate B, then we should observe a decrease in the infrared absorbance of A and a corresponding increase in the infrared absorbance of B; these signals would be correlated in time with amplitudes of comparable but opposite sign. This is not observed in this case. We have previously observed direct interconversion in studies of phLDH with the Michaelis complex substrate analog, oxamate.[125] Therefore, we assign this cluster of bands to a set of activated conformations within a parallel reaction pathway. In this context, activated indicates the complexes are ready to perform chemistry, analogous to the Michaelis complex in a simplified reaction scheme. We have also previously reported evidence of a parallel reaction pathway in the phLDH•NADH•oxamate system.[125] The observation that the substates follow parallel pathways and have different reactivity is important because it is in direct conflict with conventional enzyme models in which the chemistry occurs by crossing a single dominant activation barrier.

In contrast, the 1704 cm^{-1} transient shows a positive absorbance change and the 1710 cm^{-1} absorbance of free pyruvate is changed very little. The 1704 cm^{-1} transient is fit to a faster phase with an approximately 35 μs time constant that contributes 14% of the total signal intensity and a slower, 500 μs, phase that contributes the rest. This transient forms an important counterpart to the 1685, 1679, and 1670 cm^{-1} transients. Since the 1704 cm^{-1} transient has an intensity of the opposite sign and also effectively spans the timescale of the lower frequency bleaches, we conclude that a fraction of the population of the three Michaelis complex substates is transforming directly into the 1704 cm^{-1} substate. The 1704 cm^{-1} transient absorbance only accounts for about half of the sum of the bleach features, however, meaning the rest of the population of the Michaelis states is converting to product. We assign the 1704 cm^{-1} band as an encounter complex formed between LDH•NADH and pyruvate at an early stage of binding along the reaction pathway, characterized by weak hydrogen bonding between the protein and C2=O moiety of pyruvate. Evidence for such a state has been observed before in other studies with phLDH.[86, 124-125] The 1710 cm^{-1} transient signal of free pyruvate shows a small increase on a fast timescale that is not well correlated with the other signals. The small magnitude of this transient and its uncorrelated time dependence implies that only a small amount of free pyruvate is formed in response to the T-jump, most likely from the encounter complex directly and not from the Michaelis states.

To summarize, the transient IR data indicate three features of the enzyme reaction mechanism: first, the existence of several Michaelis complex conformations well advanced along the reaction pathway that do not directly interconvert and are characterized by varied reactivity for the chemical conversion of pyruvate to lactate; second, the existence of an encounter complex that interconverts to the activated conformations; third, the lack of a direct pathway between free pyruvate and the Michaelis states, meaning the encounter complex is an obligatory intermediate. The simplest model that incorporates all of the above conclusions from the temperature-jump data is presented in scheme 3.3 below.

Scheme 3.3

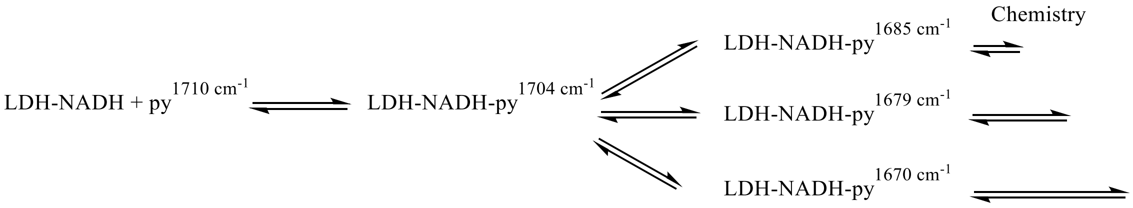

Additional support for this scheme comes from a significant body of previous work. The key points are: initial binding via the formation of a weakly interacting encounter complex,[86, 124-125] protein conformational changes associated with forming the Michaelis complex,[142] multiple well populated conformations within the Michaelis complex which do not directly interconvert, and one of these populations being incompetent towards conversion to lactate.[125, 143-144] An important finding from previous work is that a slow conformational motion within the enzyme is likely rate limiting, not the chemistry step itself. The protein motion that limits enzyme turnover involves the closure of the surface loop (residues 98-110) to bring the key residue, Arg109, into the active site (fig. 3.1), accompanied by changes far from the active site.[142] This conformational change is represented in scheme 3.3 as the transition between the encounter complex (1704 cm^{-1}) and the reactive Michaelis states. Steady state kinetics measurements of the LDH enzyme yielded a k_{cat} of 245 s^{-1} with a KIE of 1.4 comparing enzyme loaded with NADD versus NADH.[137] This value for the H/D primary KIE is lower than expected; a characteristic value of six or more would be observed if the chemical step were rate limiting. We conclude that the various protein atomic rearrangements occurring within the phLDH•NADH•pyruvate complex are on a similar timescale as the chemical step (steps 2 and 3 respectively in scheme 3.3), such that they are strongly coupled kinetically. To test the validity of our kinetic assignments we needed to develop a robust method for interpreting the temperature-jump results. Our computational modeling method is discussed in the next section.

Section 3.4 Computational Modeling of Lactate Dehydrogenase Kinetics

The complex nature of relaxation kinetics makes it impossible to make strong conclusions about samples in complex equilibrium based solely off observed relaxation rates and intensities. The observed rates are actually complex composites of all the rate constants coupled into the probed state. The degree of contribution of any reaction rate is also a complex relationship. To solve for a relaxation rate or amplitude of a known reaction pathway requires solving a system of coupled differential equations. In this section, we describe one approach to solving such a problem and apply it to modeling our LDH relaxation data described in section 3.3.

To understand our approach to modeling temperature-jump relaxation kinetics, we must first explain how to calculate relaxation times and amplitudes. We will discuss this in terms of a simple system described in equation (3.1) as this is a simplification of the Michaelis-Menten model for enzyme kinetics. Our goal is to develop a set of equations that we can use to solve for the change in concentration of a system component with time, ΔA(t), which can easily be transformed into an expression for the concentration with time A(t) if the initial concentration of component A is known. We start by writing the rate equations describing the reaction from equation (3.1).

$$A + B \underset{k_{-1}}{\overset{k_1}{\leftrightarrow}} C \underset{k_{-2}}{\overset{k_2}{\leftrightarrow}} D \tag{3.1}$$

$$\frac{dA}{dt} = \frac{dB}{dt} = -k_1AB + k_{-1}C \tag{3.2}$$

$$\frac{dC}{dt} = k_1AB - (k_{-1} + k_2)C + k_{-2}D \tag{3.3}$$

$$\frac{dD}{dt} = k_2C - k_{-2}D \tag{3.4}$$

These expressions are general and in terms of the concentration of each component (A, B, C, or D). However, we want the rate equations due to the change in these concentrations (ΔA etc.) with respect to after the temperature jump, so equilibrium concentrations (A_{eq}) and rates will be with respect to the final temperature of the jump. This change for equations (3.2)-(3.4) can be made by noting the concentration of a component is always equal to its concentration at equilibrium plus the change from equilibrium, see equation (3.5). Substituting the expression from equation (3.5) into equation (3.2) yields equation (3.6).

$$X = X_{eq} + \Delta X \tag{3.5}$$

$$\begin{aligned}\frac{d(A_{eq} + \Delta A)}{dt} = \frac{d(B_{eq} + \Delta B)}{dt} \\ &= -k_1(A_{eq} + \Delta A)(B_{eq} + \Delta B) + k_{-1}(C_{eq} + \Delta C) \\ &= -k_1A_{eq}B_{eq} + k_1C_{eq} - k_1\Delta A\Delta B - k_1A_{eq}\Delta B \\ &- k_1B_{eq}\Delta A + k_{-1}\Delta C\end{aligned} \tag{3.6}$$

We then make two key simplifications to this equation. The first is to recognize that the first two terms in the final expression of equation (3.6) are actually equation (3.2) written in terms of equilibrium. By definition, the rate of change of a concentration at equilibrium is 0, so we can take out the first two terms. This simplification also applies to the left hand side of the equation. The second simplification is that the third term (-$k_1\Delta A\Delta B$) is ignored. This is applied to all terms of the second order with respect to changes in concentration. This simplification is known as linearization of the rate expression. It is considered acceptable if only small, $\Delta X \ll X_{eq}$, changes are made to the equilibrium. In these cases, the second order terms are very small compared to the first order terms and therefore make very small contributions to the overall expression. The error from this simplification is small enough, normally, to ignore. Applying the simplifications described above to equation (3.6) yields equation (3.7). Using a similar approach, we can generate the respective rate equations for the case of C and D as well, equations (3.8) and (3.9).

$$\frac{d\Delta A}{dt} = \frac{d\Delta B}{dt} = -k_1 A_{eq}\Delta B - k_1 B_{eq}\Delta A + k_{-1}\Delta C \tag{3.7}$$

$$\frac{d\Delta C}{dt} = k_1 A_{eq}\Delta B + k_1 B_{eq}\Delta A - (k_{-1} + k_2)\Delta C + k_{-2}\Delta D \tag{3.8}$$

$$\frac{d\Delta D}{dt} = +k_2\Delta C - k_{-2}\Delta D \tag{3.9}$$

Equations (3.7)-(3.9) are a system of simultaneous differential equations which are not independent of each other. To simultaneously solve these equations we will want to make them independent. This particular example can be written in terms of two equations and two ΔX variables. This can be done by choosing any two equations and variables to be rewritten. The first choice is straightforward. Since by mass action ΔA = ΔB, we can just make this substitution to get rid of one variable. The second substitution can be done by noting that ΔC = -(ΔA+ΔD). Using these substitutions we are left with equations (3.10) and (3.11) to fully describe the system with independent equations.

$$\frac{d\Delta A}{dt} = -\left[k_1(A_{eq} + B_{eq} + k_{-1}\right]\Delta A - k_{-1}\Delta D \tag{3.10}$$

$$\frac{d\Delta D}{dt} = -k_2\Delta A - (k_2 + k_{-2})\Delta D \tag{3.11}$$

Since equations (3.10) and (3.11) are of the general form:

$$\frac{dx_1}{dt} + a_{11}x_1 + a_{12}x_2 = 0 \tag{3.12}$$

$$\frac{dx_2}{dt} + a_{12}x_1 + a_{22}x_2 = 0 \tag{3.13}$$

They have solutions of the general form:

$$x_1 = x_1^{01}\exp\left(-\frac{t}{\tau_1}\right) + x_1^{02}\exp\left(-\frac{t}{\tau_2}\right) \tag{3.14}$$

$$x_2 = x_2^{01}\exp\left(-\frac{t}{\tau_1}\right) + x_2^{02}\exp\left(-\frac{t}{\tau_2}\right) \tag{3.15}$$

We can solve for the constants x_1^{01}, x_1^{02}, x_2^{01}, x_2^{02}, τ_1, and τ_2 by using a standard eigenvalue decomposition if we write the system of equations (3.10) and (3.11) in the general form:

$$\vec{X} = [Y]\vec{x} \tag{3.16}$$

$$\text{where } \vec{X} = \begin{bmatrix} \frac{d\Delta A}{dt} \\ \frac{d\Delta D}{dt} \end{bmatrix}, \tag{3.17}$$

$$[Y] = \begin{bmatrix} -[k_1(A_{eq} + B_{eq} + k_{-1}] & -k_{-1} \\ -k_2 & -(k_2 + k_{-2}) \end{bmatrix}, \tag{3.18}$$

$$\text{and } \vec{x} = \begin{bmatrix} \Delta A \\ \Delta D \end{bmatrix}. \tag{3.19}$$

When solving these problems the eigenvalues are equal to the relaxation rates and the eigenvectors can be transformed into the relaxation amplitudes. In the simple example given here, you can solve for these constants analytically. However, since this methodology can be extended to any equilibrium being studied by relaxation methods, it makes sense to use a more general solver. A more general method is to solve for these constants numerically using computer aided software (e.g. MATLAB, Mathcad) to be able to handle equilibria of higher levels of complexity. This is the approach that we took in our simulations described below. This has been a brief summary of one approach to calculate relaxation rates and amplitudes. Further descriptions utilizing various methods and describing how to transform eigenvectors into relaxation amplitudes have been given previously and are cited for the interested expert.[145-149] Our treatment of this problem is highly informed by Bernasconi's approach.[75]

Our method for modeling reaction kinetics uses the approach above as just part of a larger technique. A schematic overview of the technique is given in figure 3.7. Modeling a proposed reaction scheme to fit the measured temperature-jump kinetics was performed with MATLAB 2013b (MathWorks, Natlick, MA) using routines written in our lab. A standard curve fitting approach is not applicable to this problem because there is not enough information known about the rate constants at each step and such an approach would be underdetermined. Instead, our overall approach was to test how well the predicted relaxation kinetics from an input reaction scheme match the experimental relaxation (temperature-jump) results.

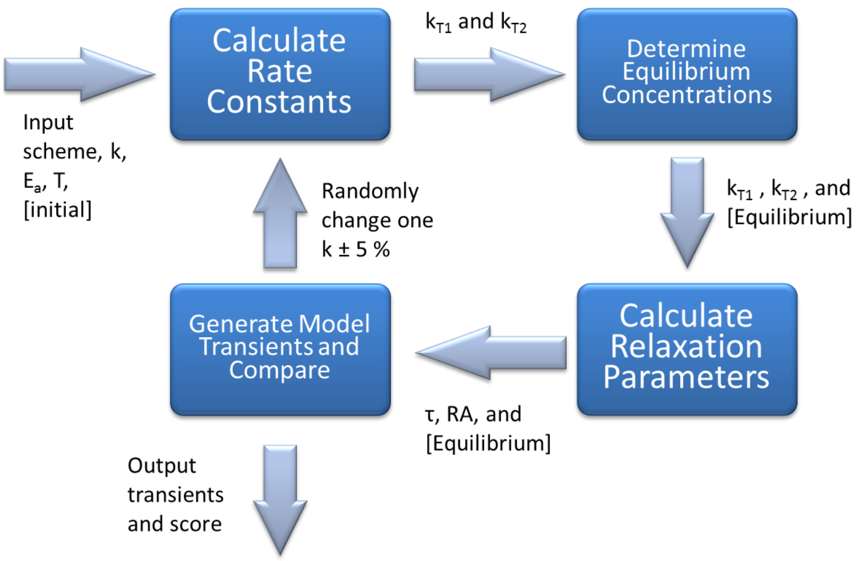

Figure 3.7: Our approach to modeling temperature-jump kinetics. The listed parameters should be taken as plural. k is for rate constants. E_a is activation energies. T is temperatures. Notes in brackets are describing concentrations. τ is relaxation times. RA is relaxation amplitudes. The score is described in the text. The technique will cycle up to a given number of cycles and will keep any rate constant changes that improve the score.

Our fitting routine involves four main steps and requires an input reaction scheme, a set of rate constants and activation energies that define the scheme at a given temperature, initial and final jump temperatures, and initial concentrations of each component in the reaction scheme. Step one generates rate constants for the scheme at the experimentally relevant temperatures. Step two determines equilibrium concentrations of all states at each temperature using a master equation approach. Step three calculates relaxation times and amplitudes by an eigenvalue decomposition approach. Step four calculates a time-dependent profile of each state based on the parameters calculated in the previous steps. To quantitatively compare similarity between a predicted set of results and the experimental data we devised a scoring method that considers all of the transient data at five different probe frequencies. First, we calculated an accuracy score for each transient as shown in equation (3.20).

$$Score_j = \sum_{i}^{n} (experimental_i - predicted_i)^2 \qquad (3.20)$$

Where j is each probe frequency, n is the total number of points in the transient, and i is a given point in time. This method gives a direct measure of how accurately the predicted transient matches the experiment and ignores whether the predicted data over- or under-estimates the experimental data. A perfect score is zero. Finally, a composite score for an entire fitting run is compiled as the summation of all the transient scores as shown in equation (3.21).

$$Total\ Score = \sum_{j} Score_j \qquad (3.21)$$

The total score is used for comparison as the whole process is cycled in a Monte Carlo fashion where a rate constant is randomly modified, the steps are repeated and the score is computed to determine if the fit is improved. To test multiple trajectories with many Monte Carlo steps in a reasonable amount of time, the calculations were performed on a multi-processor cluster in the Emerson Center for Scientific Computation.

We used this computational routine to fit the reaction scheme to the IR temperature-jump data presented in section 3.3. In essence, the routine searches for rate constants to define a given reaction scheme that will match input relaxation data. This method incorporates all coupled reaction steps and does not require making simplifying assumptions about dominant pathways. The fit data in table 3.1 show that the transients are changing on similar timescales; therefore, making assumptions about dominant pathways is unwarranted. So, using our fully realized approach is necessary.

We first attempted to fit the relaxation data with the mechanism presented in scheme 3.3. We used the rate constants and activation energies adapted from previous optical absorption and emission T-jump studies of phLDH as initial guesses.[88] However, the calculations did not fit well to all of the experimental transients with the calculations consistently reporting scores of 50-100 (lower is better) for the trajectories. Starting trajectories with random rate constants did not produce better scores. Upon analysis of the results, two types of fits were produced. Either all of the transients except the 1704 cm^{-1} transient were fit well or the 1704 cm^{-1} was fit well and the rest were not. Figure 3.8A shows a representative fit using the kinetics model defined by scheme 3.3. Step-wise adjustments to the reaction mechanism were made to test how well new models fit to the experimental data. Still, none of the various models attempted were significantly better. We conclude that the mechanism presented in scheme 3 is not sufficient to describe the relaxation data.

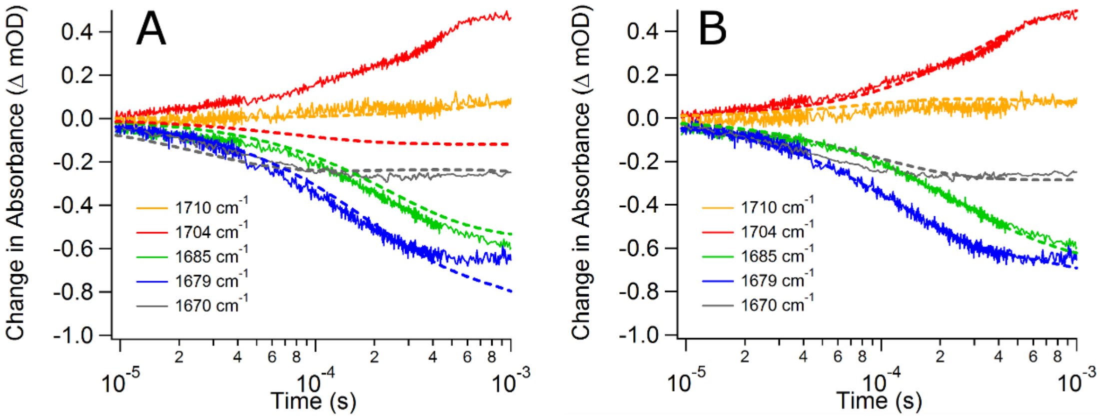

Figure 3.8: Comparison of the simulated and experimental relaxation kinetics, dashed and solid lines respectively. Graph A uses scheme 3.3 as the reaction model for simulated results. Graph B uses scheme 3.4 as the reaction model for simulated results. The most significant change is the better fit for the 1704 cm^{-1} transient when scheme 3.4 is used.

Various other possible kinetic schemes were tried;[126] these mostly involved tweaking the treatment of the 1704 cm^{-1} substate, which produced dramatic improvement of the model. We focused on this substate because the results, like those of figure 3.8A, indicate that 1704 cm^{-1} was somehow different than the other substates. The best model added the inclusion of a second encounter complex with the constraint that it could be populated only from free pyruvate (and hence is not along the reaction pathway to lactate formation). Scheme 3.4 summarizes this new kinetic mechanism. In this scheme, the encounter complex state labeled LDH•NADH•py has no discernable IR signature. The lack of an IR signal is probably due to the heterogeneous nature of this state. Most likely what we are labeling as one state is in reality a multitude of similar weakly-binding pyruvate states along a productive pathway. This heterogeneity would lead to a very broad infrared band that would be hard to detect except at high concentrations. Our simulations indicate that this substate has a concentration of 2.9 μM at equilibrium. In contrast, the 1704 cm^{-1} substate has a more tightly-bound pyruvate conformation leading to a narrower IR band allowing for its 3.8 µM concentration to still be visible. There is previous computational evidence for an array of bound pyruvate structures in lactate dehydrogenase that may give an idea of what these substates look like.[139] The inclusion of an additional substate resulted in two more microscopic rate constants. Previous experimentally derived rate constants were assumed for the competent encounter complex.[88] The final fit variables generated by the simulation examples shown in figure 3.8 are reported elsewhere.[126] The result of the change was to increase the overall population of the non-competent encounter complex at elevated temperature in the simulation and therefore increase the absorbance at 1704 cm^{-1}.

Scheme 3.4

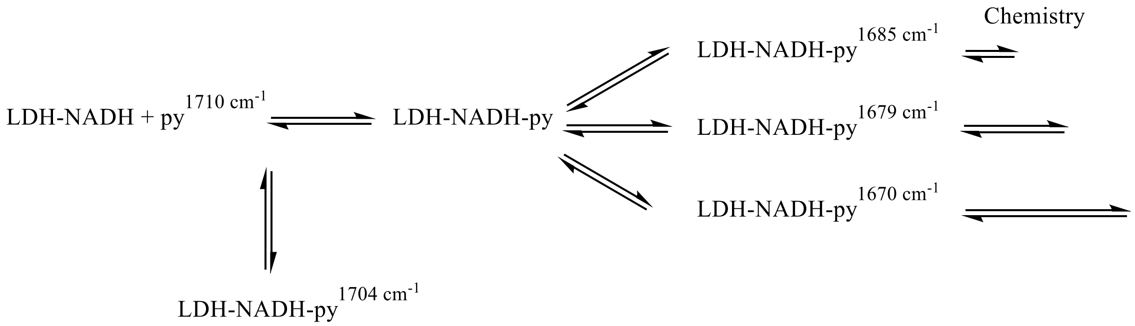

The model summarized in scheme 3.4 fits the experimental data well in a number of ways. It is qualitatively obvious by looking at figure 3.8B that the new model better matches each of the experimental transients than the fits shown in figure 3.8A. Quantitatively, the routine-specific score values of 3-5 were drastically better for the new model as compared to the original model's scores of 50-100. Finally, we can see by comparison in table 3.1 that the observed relaxation lifetimes calculated by fitting the theoretical transients are similar to the observed relaxation lifetimes from the experimental data. The inclusion of a dead-end, or non-competent state along the reaction pathway is not a new concept. We have previously seen evidence for a dead-end complex when studying the phLDH system with the substrate mimic oxamate using infrared as the probing method.[125] However, the oxamate work suggested the observed dead-end complex was a well-populated Michaelis conformation instead of an encounter complex. Scheme 3.4 is not intended to assert that there are no additional Michaelis conformations, or that all activated conformations are productive. Instead, scheme 3.4 is the simplest model that fits the experimental data, and it supports multiple enzyme conformations at both the encounter and Michaelis complex stages of the reaction pathway. There is no evidence for dead-end complexes when the pyruvate system is studied using only NADH fluorescence as a probe with temperature-jump.[88] In work on a nitrated mutant enzyme, Clarke and coworkers did see evidence of multiple enzyme-bound pyruvate states where one such state was significantly slower reacting at cryo-temperatures using stopped-flow.[150] They suggested these states could slowly interconvert directly. It is possible that our second encounter complex may in fact be the second pathway they suggest, but that it is interconverting or reacting too slowly to observe in our experiments and is essentially non-productive. Experiments in section 3.5 using our mixing system are aimed at studying this pathway described by Clarke and coworkers to determine its relevance at more physiologically-relevant conditions when examined by mixing.

There are differences between the experimental and simulated transients, even for the best fit to scheme 3.4. The major differences are that the best fit to the 1704 cm^{-1} transient is to a different number of exponentials and that the 1670 cm^{-1} transient is fit to a significantly different lifetime. The simulated lifetime for the 1704 cm^{-1} transient is in-between the two lifetimes of the double exponential fit of the experimental data. This difference is likely due to the noise and small subtraction artifacts present in the experimental data that make it difficult to fit the data. The simulation also predicts a longer lifetime for the 1670 cm^{-1} transient than what is observed experimentally. The transient IR signal for this state is very small due to its low population, making it difficult to fit. It is also possible that the rate constants for this state are not fully optimized in the simulation, since it only contributes a small fraction of the total reaction flux. It is important to point out that, despite these small discrepancies, the model still predicts a decreasing lifetime with decreasing probe frequency.

The defining feature of the kinetic model in scheme 3.4 is parallel pathways with Michaelis states of varied reactivity. Furthermore, the model indicates that the reactivity scales with the frequency of the pyruvate C2 carbonyl stretching frequency: the lower the frequency, the higher the reactivity (shorter lifetime for the chemistry step). This relationship can be understood in terms of the relationship of the vibrational frequency to the force constant and hence the bond distance or the degree of polarization of the bond. In the diatomic approximation, a shift of the carbonyl mode from 1710 to 1679 cm^{-1} represents a lengthening of the C=O bond by 0.01 Å,[151] making it more susceptible to nucleophilic attack by the hydride. It is interesting to note that the enzyme does not primarily bind pyruvate in the most reactive substate. At equilibrium the 1679 cm^{-1} substate is clearly the most populated one, as shown in figure 3.5. Since these substates do not interconvert directly, the net flux through each depends on the branching from the initial encounter complex. Apparently the enzyme is not optimized to primarily use the fastest pathway and the overall turnover rate is a population weighted average of the multiple parallel pathways. The model outlined in scheme 3.4 and the kinetic parameters used to generate figure 3.8B predict an ensemble averaged turnover rate of k_{cat} = 179 s^{-1},[126] which is similar to the average turnover rate determined from NADH absorbance measurements k_{cat} = 245 s^{-1}.[137] Thus, the IR measurements provide a high-resolution view of many of the relevant substates in the enzyme reaction pathway in contrast to simply observing the ensemble turnover rate

From our analysis of the work presented in sections 3.3 and 3.4, we developed a model of LDH catalysis that involves numerous pathways with varied reactivity. To continue to study these reaction pathways we paired the temperature-jump studies with fast mixing studies. The results of the mixing studies are discussed in the next section.

Section 3.5 Rapid Mixing Experiments with Competent and Inhibited Samples

Our work using infrared temperature-jump to study lactate dehydrogenase has added to the evidence for off-reaction pathway states for LDH. These states are indicative of the relevance of a three-dimensional reaction landscape to describe the energetics of the LDH reaction. However, the studies on LDH that support off-reaction pathways have utilized temperature-jump spectroscopy.[125-126] While the temperature-jump method is reliable, it is often difficult to clearly define kinetic constants from the interpretation of temperature-jump data. The cryogenic stopped-flow work of Clarke and coworkers also found evidence for branching reaction pathways in LDH and were able to fully describe the rate constants that govern the pathways.[150] The application of their work to physiological conditions is unclear because they had to work at cryogenic temperatures and with dimethyl sulfoxide as a buffer component to be able to slow down the reaction kinetics enough to work with a traditional stopped-flow device. We can avoid this limitation by utilizing our fast mixing device described in section 2.3.

The mixing experiments we performed included mixing substrates with the binary LDH•NADH complex. We used both the active substrate pyruvate and the transition state mimic oxamate. The pyruvate mixing experiments are the ideal experiment because they allow for direct observation of the enzyme performing chemistry. Since we expect oxamate to bind in the same way as pyruvate, mixing oxamate with the enzyme should show all enzymatic events up to chemistry. By comparing the results from both mixing experiments we are able to sort out what observed events are due to pre-chemistry conformational change and which are directly coupled to chemistry.

Equilibrium Fluorescence

The catalytically competent LDH system has three natural fluorescence probes: direct tryptophan emission (excitation at 280 nm, emission at 350 nm), direct NADH emission (excitation at 340 nm, emission at 445 nm), and FRET from tryptophan to NADH emission (excitation at 280 nm, emission at 445 nm). In the fluorescence mixing data below we use all three of these probes to investigate the mixing of LDH•NADH with both the catalytically competent substrate pyruvate and the non-competent substrate analog oxamate. All equilibrium fluorescence measurements were performed on a Horiba Jobin Yvon (Edison, NJ) Spex Fluoromax-3 fluorimeter with a 1 nm resolution, a 1.00 nm excitation slit width, a 1.40 emission slit width, a 0.1 s integration time, and either 280 nm or 340 nm excitation light. The reported spectra are an average of 10 scans. The data were exported and analyzed with Igor Pro 5.00 software from Wavemetrics (Lake Oswego, OR). The samples initially contained 5 µM LDH and 10 µM NADH and either no additional substrate, 10 µM pyruvate, or 10 µM oxamate. The buffer used for all studies was 50 mM sodium phosphate and 100 mM NaCl at a pH of 7.1. Of course, upon mixing enzyme, cofactor (NADH), and pyruvate this system became a chemically competent reaction and would mainly contain enzyme, oxidized cofactor (NAD+), and the reaction product lactate. Experiments were carried out at room temperature, approximately 22 °C. Figure 3.9 displays the fluorescence profiles of the enzyme equilibrium mixtures that correspond to the products of the mixing reactions described below.

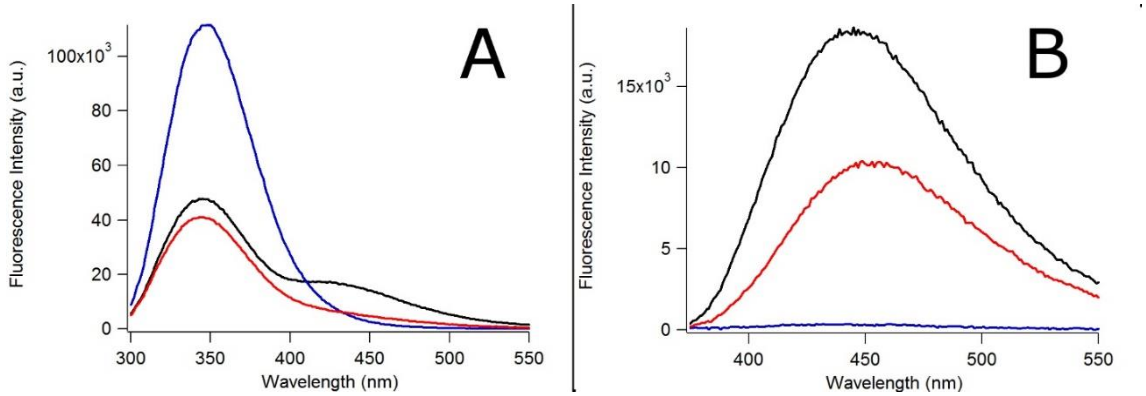

Figure 3.9: Equilibrium fluorescence of LDH•NADH complexes. The complexes are LDH•NADH with no substrate (black), LDH•NAD+•lactate which is the result of mixing LDH•NADH and pyruvate (blue), and LDH•NADH•oxamate (red). The spectra on the left (A) are excited at 280 nm and show tryptophan emission centered around 350 nm and FRET from tryptophan to NADH centered around 445 nm. The spectra on the right (B) are excited at 340 nm and show NADH emission centered around 445 nm.

As can be observed in figure 3.9, there are significant differences in the emission spectra of the mixing reaction products when probed by all three emission probes. When pyruvate is added to a solution of LDH•NADH we expect, under these conditions, for the enzymatic reaction of pyruvate to lactate to go to completion since there is enough NADH present. This is most clearly observed in figure 3.9B where we see the emission of NADH from direct excitation disappear almost entirely. Upon oxidation of NADH to NAD+ on the enzyme, NADH loses its 340 nm absorbance band and can no longer be excited to an emissive state by this wavelength. Similarly, we observe in figure 3.9A that upon mixing pyruvate with LDH•NADH the FRET band at 445 nm also disappears almost entirely for the same reason. As a consequence of this loss of FRET from the excited tryptophan to the NADH we also observe a significant increase of the tryptophan emission.

In contrast to the chemical turnover that occurs with the addition of pyruvate to LDH•NADH, when we add oxamate to the enzyme binary complex no catalytic turnover occurs. Even without oxidation of NADH from enzyme turnover there are still significant changes to the emission spectra of LDH•NADH upon binding of oxamate. The changes that the addition of oxamate induces are caused by enzyme conformational changes which change the cofactor orientation upon substrate binding and have been discussed previously.[124] These changes are observed spectroscopically in three ways. First, the emission from direct excitation of NADH is decreased by almost 50 % and the emission wavelength red-shifts by a few nanometers. Second, due to decreased acceptor, i.e. NADH, emission intensity there is also an approximately 50 % decrease in FRET intensity. Finally, the signal from direct tryptophan emission is also slightly decreased. This last observation is somewhat confusing. If acceptor emission efficiency has been decreased, as in the pyruvate case, we may expect to see an increase in donor emission. However, the interpretation of tryptophan emission is not so straightforward. We have no direct evidence for a decrease in FRET efficiency, just for a decrease in acceptor efficiency. The tryptophan emission should still be getting quenched by NADH since no chemistry has occurred. Furthermore, each LDH monomer contains six tryptophans. It is possible that the substrate-binding induced conformational changes of the enzyme may be causing some of the tryptophans to be exposed to a more quenching environment like a nearby histidine or solution. The origin of this change is not key to our work, but it is useful to note that tryptophan emission is decreased upon substrate binding.

In total, the equilibrium fluorescence spectra presented in figure 3.9 indicate that there are very significant changes to the emission spectra of LDH•NADH upon mixing with pyruvate or oxamate. Furthermore, since there is a difference in both the magnitude and direction of these changes depending on whether oxamate or pyruvate is introduced, we should be able to sort out which changes in the fluorescence mixing data presented below are due to substrate binding and which are due to chemical turnover by comparing the results of mixing both substrates with LDH•NADH.

Microfluidic Fast Mixing

The fast mixing device we used to study the reaction dynamics of LDH is capable of quickly changing probing methods; therefore, the various spectroscopic results presented below are recorded sequentially with the same mixing experiment. While collecting the reaction dynamics with each substrate we were able to maintain the device flowing and just change over the solution source for the outer capillary solution effectively eliminating protein sample variability between the different substrate mixing experiments. In this experiment we flowed a solution of 200 µM LDH and 300 µM NADH in the inner stream and, where applicable, a 1 mM solution of substrate in the outer stream. We chose to flow the substrate in the outer solution because of its small size and therefore faster diffusion time. The mixing time of the substrate with the inner solution is approximately 100 µs. As the diffusion time of the protein is slow, the concentration of the enzyme remained relatively constant for several milliseconds.

Data from the mixer was collected on an Olympus (Center Valley, PA) IX81 microscope system. For these LDH experiments, the microscope was used for fluorescence imaging. For direct tryptophan excitation studies and FRET emission studies, the source of light was the frequency tripled output from a Coherent (Santa Clara, CA) Mira Ti:Sapphire laser run at 82 MHz centered around 850 nm pumped by a Coherent Verdi-V12. For direct NADH excitation studies, the light source was a CrystaLaser (Reno, NV) Q-Switched 351 nm diode pumped laser run at a 1000 Hz rep rate. Excitation light was directed through an appropriate short pass filter from IDEX Optics and Photonics (Albuquerque, NM) through a 40x UV focusing objective from Thorlabs (Newton, New Jersey). Emission is collected through the same objective and reflected off the short-pass filter through an appropriate bandpass filter (also from IDEX), depending on optical probe, and collected as an image on a Hamamatsu (Bridgewater, NJ) C9100-14 ImageM-1k EM-CCD camera. Images were collected with various exposure times to maximize signal, but typical exposure times were 20 seconds for direct excitation of tryptophan, 5 seconds for direct excitation of NADH, and 3 seconds for FRET studies with a gain setting of 1 and an intensification setting of 255. The CCD array was actively cooled to -57 °C. Sample solutions were at room temperature for mixing experiments, approximately 22 °C. Figure 3.10 displays the results of mixing pyruvate or oxamate with LDH•NADH when probed by direct excitation of tryptophan emission.

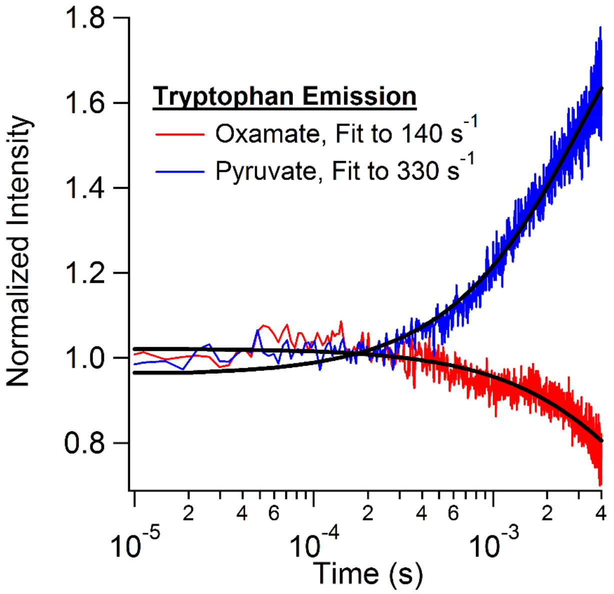

Figure 3.10: Trp-probed mixing transient of LDH•NADH and substrate. The data are presented as the normalized fluorescence intensity of tryptophan emission (excitation: 280 nm, emission: 340 nm). Single-exponential fits to the data are shown and their fit rates are listed in the legend. The fit shown for the oxamate data is shown to emphasize the difference in the traces, but should not be taken as an accurate fit because the fit lifetime is outside the observation window.

The results of probing the fast mixing of LDH•NADH with pyruvate by tryptophan emission are markedly different than those obtained by fast mixing with oxamate. The most obvious difference in the two transients shown in figure 3.10 is the opposite sign of their signal change. The pyruvate-mixing transient shows a significant increase in tryptophan emission whereas the oxamate transient shows a slight decrease in tryptophan emission. This result is consistent with the equilibrium fluorescence data presented above. The obvious assignment for the kinetic event observed in the pyruvate transient is chemical turnover. Not only does the tryptophan emission increase as expected, see above, but we do not see a commensurate change in the oxamate signal where chemical turnover should not occur. The kinetic event fits to a single exponential curve with a rate of 330 s^{-1}. This rate is in-between previously reported rates for the chemical step, 637 s^{-1}, and the reported k_{cat} for pig heart LDH of 245 s^{-1}.[88, 137] Product release is likely not being observed because the increase in tryptophan emission should occur due to the redox step, not any conformational change. The subsequent loop domain rearrangement, or opening, must follow the chemistry step, so it is understandable that our observed rate is faster than k_{cat}.[88, 123] The exponential fit to the oxamate data is shown to help the reader see the difference in the timescales of the observed changes, but should not be taken as accurate because the exponential function is fitting to a decay time (10 ms) substantially outside the data collection window (4.5 ms).

Figure 3.11 shows the results of observing the mixing reaction by FRET from the tryptophan to the NADH. In contrast to the tryptophan transients displayed in figure 3.15, there is more similarity in the FRET transients. Both the pyruvate and oxamate FRET transients show a decrease in overall signal of approximately the same amount. When these transients are fit to exponential functions, the oxamate data fits to a faster decay rate of 2060 s^{-1} whereas the pyruvate data fits to a decay rate of 1620 s^{-1}. The oxamate data is fit only to a single exponential curve, but the pyruvate data is actually shown fit to a double exponential curve. The pyruvate data did not fit well to just a single exponential curve; the fit was unable to match the early timescale data. The faster decay rate of the double exponential fit was 17,400 s^{-1}. This is approximately equal to the rate expected for pyruvate binding, approximately 15,000 s^{-1}, under these conditions.[88] However, we would expect the binding to be obscured, if visible, because it is within the approximately 100 μs mixing time for the apparatus. The additional exponential curve in the fit is a good approximation for the overlap of the substrate binding and mixing which allows us to effectively separate out this early time event from the slower event. A single exponential fit is sufficient to fit the oxamate data. This is reasonable because the binding constant of oxamate at this temperature is almost twice as fast as the pyruvate binding constant.[124] This would lead to the majority of oxamate binding being outside the observation window of this technique.

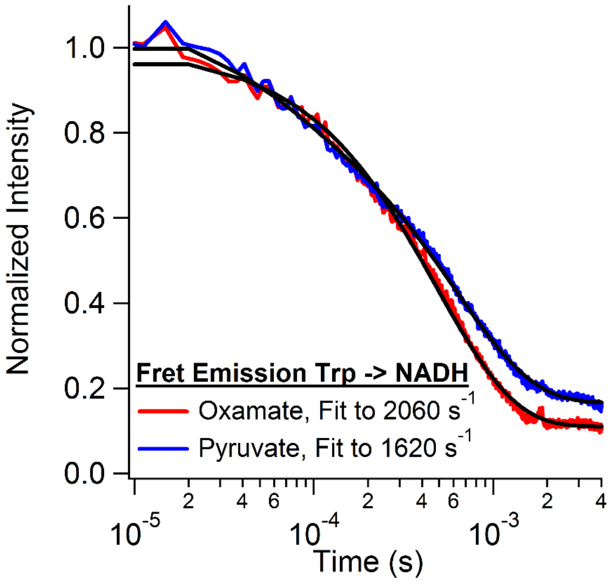

Figure 3.11: FRET-probed mixing transient of LDH•NADH and substrate. The data are presented as the normalized fluorescence intensity of FRET emission, tryptophan to NADH (excitation: 280 nm, emission: 460 nm). Exponential fits to the data are shown and their representative fit rates are listed in the legend.

We assign the decay rates in figure 3.11 to substrate-binding induced conformational change. As has been discussed extensively in this chapter, it well-known and previously observed that there is a mobile loop on LDH that closes down after substrate binds and prior to chemistry occurring. From the discussion above regarding the binding times of these substrates, we know that the decay rates of 2060 s^{-1} and 1620 s^{-1} are well after the substrate is bound and mixing is complete. Furthermore, the tryptophan transients shown in figure 3.10 allow us to determine the timescale of the chemistry step under these experimental conditions to be much later than the FRET decay rates. Therefore, since the observed rate is in-between substrate-binding and the chemistry step, and we know the loop motion should affect the acceptor emission of the FRET pair, we can confidentially assign the FRET decay as due to the loop motion in the enzyme. It is interesting that the oxamate rate is faster than the pyruvate rate. Previous temperature-jump studies have indicated the rate of the loop motion to be faster in the oxamate-bound complex as opposed to the pyruvate-bound complex, but this is the first direct comparison of these rates.[88, 124-125]

The final spectroscopic probe we used to investigate these mixing reactions was direct excitation of the NADH cofactor. The results of that study are shown in figure 3.12. The NADH mixing transients are more similar to the FRET transients than the tryptophan transients. We again see similarity between the oxamate-mixing and pyruvate-mixing transients. Both transients decrease in signal by about the same amount. There is a key difference between the data sets though. The oxamate NADH data levels off on the millisecond timescale, both FRET transients do this as well, but the pyruvate NADH data does not level off. This difference is significant. We are able to sort out the meaning of this difference through fitting the data.

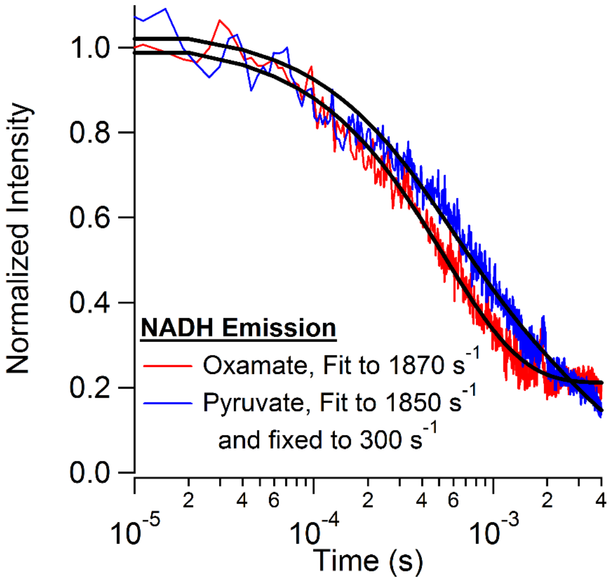

Figure 3.12: NADH-probed mixing transient of LDH•NADH and substrate. The data are presented as the normalized fluorescence intensity of NADH emission (excitation: 355 nm, emission: 460 nm). Fits to the data are shown and their representative fit rates are listed in the legend. See the text for a discussion of the fitting functions used.

The oxamate NADH transient is again well-fit by a single exponential curve. The decay rate of 1870 s^{-1} is similar enough to the FRET decay rate of 2060 s^{-1} that, within the error of this experiment, the two transients are likely reporting on the same event. The pyruvate NADH data can also be fit to a single exponential curve. The decay rate of this fit is about 1100 s^{-1}. Unlike with the case of the oxamate data, the pyruvate NADH decay rate is not very close to the pyruvate FRET data. A reasonable explanation for this discrepancy is that we would expect the NADH emission to report on more than the just the loop motion. The oxidation of NADH during the chemistry step should also be visible here. We have shown the chemistry step to occur on the 300 s^{-1} timescale and the loop motion to occur on the 1600 s^{-1}. These two events are similar enough in timescale that they are coupled kinetic events. We can fit to a series of coupled unimolecular transformations to test this hypothesis. Equation (3.22) gives the basic scheme for two consecutive unimolecular transformations while equation (3.23) shows the application of this model to this LDH study. Equation (3.24) indicates that the overall spectroscopic signal that we observe at any given time, S(t), is really a linear combination of the three relevant concentrations multiplied by a spectroscopic scaling constant, s_x, that describes their relative fluorescence.

$$A \overset{k_1}{\to} B \overset{k_2}{\to} C \tag{3.22}$$

$$LDH \bullet NADH \bullet pyruvate^{open} \overset{k_1}{\to} LDH \bullet NADH \bullet pyruvate^{closed} \tag{3.23}$$

$$\overset{k_2}{\to} LDH \bullet NAD + \bullet \text{ lactate}$$

$$S(t) = s_A A(t) + s_B B(t) + s_C C(t) \tag{3.24}$$

The time-dependence of two consecutive unimolecular transformations has been solved for previously and are shown in equations (3.25)-(3.27).[152] Where A_0 is the initial concentration of state A, the rate constants k_1 and k_2 are defined as in equation (3.22), and t is time.

$$A(t) = A_0 e^{-k_1 t} \tag{3.25}$$

$$B(t) = \frac{k_1}{k_2 - k_1} A_0 (e^{-k_1 t} - e^{-k_2 t}) \tag{3.26}$$

$$C(t) = A_0 - B(t) - A(t) \tag{3.27}$$

In preparation for substituting equations (3.25)-(3.27) into equation (3.24), we can make some simplifying adjustments. Since all the mixing transients are normalized to one at early time and we know that at early time only A exists, then the product of the spectroscopic constant for component A, s_A, times the concentration of A at early time,

A_0, must be equal to one. We can also define the constant s_B in terms of s_A by realizing that its intensity is some fraction, s_f, of the overall intensity of the constant s_A. And finally, as figure 3.9 shows, the oxidized NAD+ does not have any fluorescence when excited at 340 nm. Therefore, we can set this spectroscopic term, s_C, to be zero. These statements are summarized in equations (3.28)-(3.30).

$$s_A A_0 = 1 \tag{3.28}$$

$$s_B = s_f \cdot s_A \tag{3.29}$$

$$s_C = 0 \tag{3.30}$$

Substituting equations (3.25)-(3.30) into equation (3.23) and simplifying yields equation (3.31). A final y_0 term is added to compensate for background fluorescence.

$$S(t) = \left(1 + s_f \frac{k_1}{k_2 - k_1}\right) e^{-k_1 t} - \left(s_f \frac{k_1}{k_2 - k_1}\right) e^{-k_2 t} + y_0 \tag{3.31}$$

If we fit the pyruvate NADH mixing data to equation (3.31), the RMSD of the fit improves by about 3 percent. The decay rates are 1400 s^{-1} and 150 s^{-1}. These rates, particularly the slower rate, are smaller than expected. Furthermore, some of the other fit constants, like $y_0 = -0.012$, are non-sensible. Based on how we have normalized the data, we expect to see a positive signal baseline due to the excess NADH in solution. The non-linear least squares algorithm being used is likely failing due to the small amplitude of the slow phase and because there is a limited amount of time in the millisecond region of the observation window through which to fit the slow phase. A better way to handle this fitting task is to take advantage of the known slow phase rate from the tryptophan transient data and hold the decay rate of the second phase to 300 s^{-1}. When the fit is repeated under these conditions, the RMSD of the fit is within 0.5 % of the original single exponential fit. The similarity in the RMSD values indicates that the fits are equally valid; however, the results of the latest fit make more sense. The fast phase is fit to a decay rate of 1850 s^{-1} while the slow phase is held to 300 s^{-1}. The y_0 is fit to 0.020, a more reasonable final fluorescence level. Finally, the spectroscopic constant relating the fluorescence intensity of state A to state B is fit to a value of 0.36. This number is very close to what you would predict, 0.30, by scaling the data in figure 3.9 to the appropriate concentrations and integrating the intensity of the emission band by the parameters of the bandpass filter we were using to observe the NADH emission on the camera. We have already assumed in this analysis that there is a slow rate related to chemistry. We can assign the faster decay rate by observing the fit value's similarity to the value from the FRET pyruvate transient. The faster rate is likely to be loop motion. Therefore, if we fit the NADH pyruvate mixing transient as a sequence of coupled consecutive steps we are able to comprehend the observed changes in fluorescence.

We studied the kinetics of the reaction pathway of LDH with our microfluidic fast mixer in hopes of better understanding the heterogeneity observed in other experiments. Our mixing results are actually well-resolved by a relatively simply model of kinetics. The substrate binds to the enzyme, the enzyme undergoes a conformational change, and then the chemistry step occurs. We were able to show that the conformational change in the oxamate-binding case is faster than the pyruvate case. We were also able to clearly resolve the rate constant for the conformational change at physiologically-relevant conditions. We were unable to see evidence for the slow or dead end pathway seen in our temperature-jump studies or the cryogenic stopped-flow studies of Clarke and coworkers.

One possible explanations is that our mixing studies did not favor the dead end reaction pathway. In the cryogenic work, as the temperature increased, the amount of the enzyme that went down the slower pathway was reduced. The amount of excursions down the slower pathway was also reduced as the researchers decreased the amount of dimethyl sulfoxide in the buffer solution.[150] Since the conditions in our mixing study were at significantly higher temperatures and the buffer contained no dimethyl sulfoxide, it is possible that we were just unable to see such an unfavored state with our studies. The difference between the mixing studies indicates that different parts of the reaction landscape are accessible when the system is probed under different conditions and emphasizes the utility of fast mixing devices to study enzyme kinetics.

Section 3.6 Summary and Conclusions of LDH Work

In this work, we examined the reaction pathway of pig heart LDH using temperature-jump and rapid-mixing. Through analysis of equilibrium infrared spectra, relaxation transients, and subsequent kinetic modeling, we developed a novel scheme for LDH catalysis that involves several branching pathways and supports the presence of a slow or dead-end complex. Our results provide direct evidence not only for the population of various enzyme conformations, but also indicate that the enzyme samples multiple conformations while performing catalysis. This observation provides further support for a dynamic view of enzyme catalysis where the role of the enzyme is not just to bring reactants together, but also to guide the conformational search for chemically-competent interactions. In contrast, the mixing data did not clearly indicate heterogeneous kinetics, despite earlier mixing studies supporting multiple pathways. However, it seems that what we have shown is that the environment under which a system is studied and also the method by which it is studied can have significant impacts on which reaction pathways are accessible.

The inclusion of substates that are off an optimal kinetic pathway is particularly interesting when considering the induced fit framework for understanding enzyme reactions. In this framework the binding of substrate induces conformational changes in the enzyme that are necessary for catalytic action.[153] The presence of a non-competent encounter complex complicates this framework because it suggests the induced conformational change can be wrong. Because in our studies this non-competent encounter complex does not convert to the competent one directly, the enzyme must release the substrate and try again. This result also implies that the enzyme is not perfectly pre-organized for any interactions with substrate, but is instead in a dynamic search for the correct interaction with substrate that will lead to catalysis. The presence of similar heterogeneity in the activated conformations indicates this search is not complete once substrate binds to the enzyme. The search continues throughout the reaction pathway. Furthermore, our results indicate that the various Michaelis states are catalytically competent at different rates. This finding implies that the enzyme's conformational search is not necessarily for one optimal pathway or conformation, but simply for one that will work. The discrepancy in our experiments also supports this idea because the easiest pathway for the enzyme to utilize can vary with the environmental conditions. The enzyme, therefore, has not eliminated the search for the correct reactant interaction, as compared to uncatalyzed chemistry, but instead provides a platform for greatly reducing the search. The non-optimized nature of many enzymes has already been noted by other researchers, so it is interesting to consider whether the imperfection in the search process is part of the evolutionary fine-tuning of an enzyme to keep turnover rates from becoming so fast as to throw off biological equilibrium.[2] For this reason, we expect populations of catalytically-relevant heterogeneous structures to be an important conserved feature of many enzymes.

Chapter 4. Dihydrofolate Reductase

Section 4.1 Introduction to Dihydrofolate Reductase

Dihydrofolate reductase (DHFR) catalyzes the reduction of 7,8-dihydrofolate (DHF) to 5,6,7,8-tetrahydrofolate (THF) mediated by the cofactor NADPH (fig 4.1). The pro-R hydride of NADPH is known to transfer to the C6 carbon of the pterin ring while the N5 position of the pterin ring is protonated by a water or adjacent residue.[154-155] In *E. coli* DHFR, the version studied here, the residue Asp27 is associated with this proton transfer.[156-158] The production of tetrahydrofolate is important as a precursor for biosynthesis of thymidylate, purine nucleotides, and some amino acids.[155, 159] In some organisms, such as higher vertebrates, DHFR is also known to function less effectively on other pterin systems like folate, H_2biopterin, 6-methylH_2pterin and 8-methylpterin.[155]

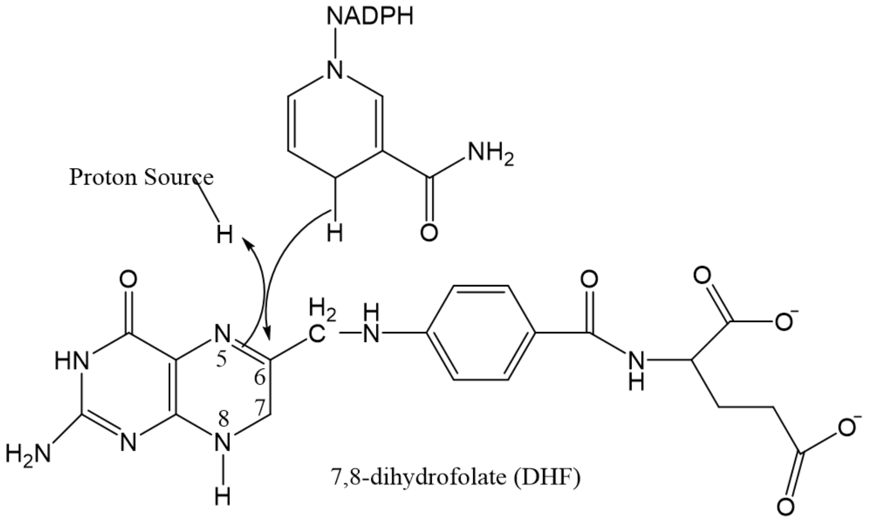

Figure 4.1: Chemical reaction catalyzed by dihydrofolate reductase (DHFR). DHFR utilizes the cofactor NADPH and a proton source to reduce 7,8-dihydrofolate to 5,6,7,8-tetrahydrofolate. A hydride from NADPH is transferred to C6 of DHF, and a proton is transferred to N5 of DHF.

Since DHFR is the sole source of cellular THF, it is an essential catalyst for cell proliferation. For this reason DHFR has been extensively studied as a drug target. DHFR is the target for the anticancer compound methotrexate (MTX, fig 4.2). In fact, MTX was utilized first as an anticancer drug and then DHFR discovered in studies to understand its function.[160] MTX still serves as an important drug for the treatment of leukemia and lymphoma. MTX, and therefore likely DHFR inhibition, is also used in the treatment of rheumatoid arthritis.[161] The DHFR sequence varies significantly enough between species that it effects the binding of inhibitors; consequently, DHFR inhibitors designed to take advantage of these differences can be used in the treatment of parasitic infections. Trimethoprim binds *E. coli* with a K_i of approximately 100 pM while binding to many vertebrates with a K_i in a range of 1-4 µM. The 10^4 difference in K_i allows for the selective inhibition, and subsequent cell death, of many bacterial infections. Pyrimethamine is used similarly to treat malaria caused by *Plasmodium* infections.[155]

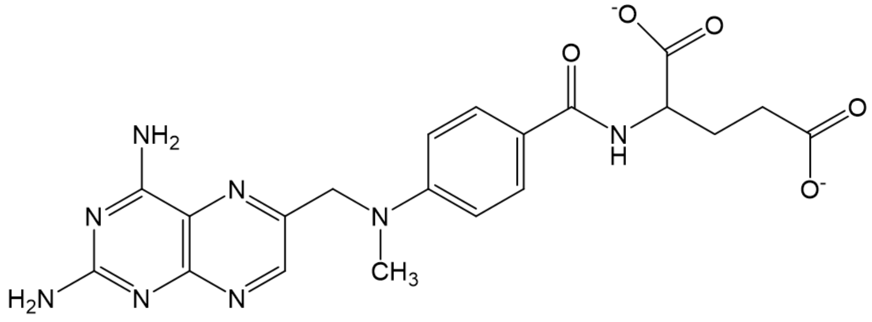

Figure 4.2: Chemical structure of methotrexate (MTX), a high-affinity ligand of DHFR.

The long history of DHFR studies has made it a good model system for examinations of enzyme function. The structure of DHFR from several organisms and in several ligand-bound states have been resolved.[155, 162] A thorough explanation of its kinetic scheme, including the rate constants between micro-states along the reaction pathway, has also been determined.[159] As the questions in enzyme function research have shifted from “what” enzymes do to “how” enzymes do what they do, it is not surprising that DHFR has become an important system because of this extensive knowledgebase. For example, early enzyme theory would predict that primarily only mutations near the active site could affect reaction rates; however, studies involving DHFR have shown that mutations remote from the active site can significantly affect hydride transfer rates and kinetic isotope effects (KIE).[163-165] These kinds of observations have led to questions about the role of networks of coupled proteins motions for enzymatic function.[154, 166-167] Furthermore, analysis of these protein motions in enzymes have led some researchers to argue for an increased role of quantum-mechanical tunneling in enzymes utilizing proton and hydride transfers, such as DHFR.[30, 32, 120] Including tunneling in the variety of ways enzymes can go past the reaction barrier is a significant shift in our understanding of enzymes and can help explain some shortcomings of applying transition state theory to enzymes.[32] Another way DHFR has been useful in studies of enzyme function has been its ubiquity. Since DHFR is found in all organisms, it is possible to compare the enzymes from several organisms native to a wide variety of environments. Comparing the flexibility, kinetics, and structure of DHFR from psychrophiles, mesophiles, and thermophiles is useful for understanding enzyme evolution and how enzymes utilize energy from their surroundings to function.[168-170] Early examinations of DHFR made all these latter studies possible leading to an even more detailed understanding of how the enzyme functions, yet questions still remain regarding the relationship between structure, function, and dynamics in DHFR.

One uncertain feature of DHFR catalysis is the role of its many loops. The *E. coli* version of DHFR is known to contain three major loop subdomains: the Met20 loop (residues 9-24), the F-G loop (residues 116-132), and the G-H loop (residues 142-150).[161] These loops are flexible and dynamic, so that the contacts between them and the active site can change throughout the reaction cycle.[162, 171] The Met20 loop is known for making the most distinct changes throughout the reaction cycle. The Met20 loop exists in three different conformations known to change due to the ligands bound to the protein and the progress in the reaction cycle.[162, 172] The reactant-like states, such as the holoenzyme (DHFR•NADPH) and the Michaelis complex (DHFR•NADPH•DHF), are believed to exist in the so-called closed loop state where the loop closes on the nicotinamide ring of the NADPH. The product-bound states involving THF exist in the occluded conformation where the loop has folded into the nicotinamide-binding pocket to force out the cofactor.[172] The third Met20 loop state is the open state. This state is associated with a more flexible enzyme structure; the open Met20 loop is not as rigidly locked down into a particular conformation and has more disorder.[173] The open confirmation is the most frequently occurring crystallographic conformation as it can be resolved from several ligand-bound states.[162] It is believed that the open confirmation may be sampled during the transition state but not necessarily be the dominant state during the rest of the reaction cycle.[174] Figure 4.3 shows the structures of these three states.

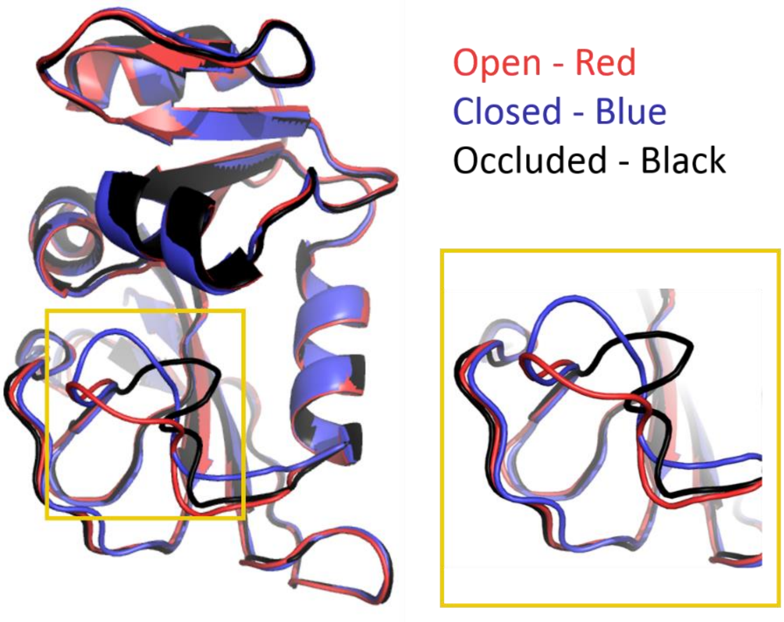

Figure 4.3: The crystal structure of DHFR in the three Met20 states. The yellow box signifies the Met20 loop in the context of the entire protein on the left and is expanded on the right. The red structure represents the open state, PDB: 1RA9. The blue structure represents the closed state, PDB: 1RX2. The black structure represents the occluded state, PDB: 1RX7.

While the structural characteristics of the three Met20 loop conformations are well-understood, their contribution and coupling to catalysis is not. A general kinetic scheme and the associated changes in the Met20 structure along the reaction cycle are known, but not the kinetics of the loop motions themselves.[159, 172] The limit to cataloging these features has been experimental. The loop motion lifetimes should be around the millisecond timescale, which is traditionally hard to observe. Using the techniques described in chapter 2 of this work we should be able to observe these motions directly. We take advantage of the intrinsic tryptophan fluorescence of DHFR as our probe. DHFR has five tryptophan residues spread throughout the protein (fig. 4.4). As the protein adopts a new conformation, these tryptophans move and their emission changes accordingly. We present in the following sections studies of the loop motions of DHFR utilizing fluorescence temperature-jump spectroscopy (section 4.2) and our microfluidic mixer (section 4.3).

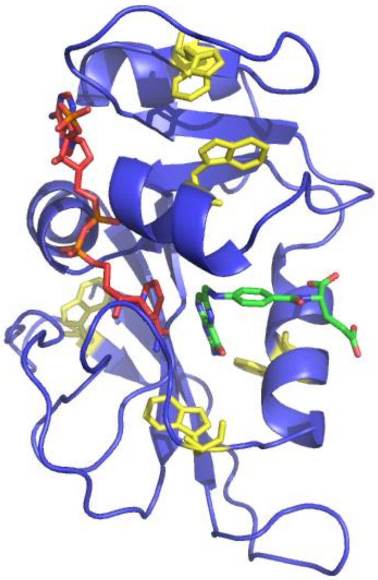

Figure 4.4: Crystal structure of DHFR highlighting the tryptophan residues. The crystal structure is in the closed conformation. The five native tryptophans are shown in yellow dispersed throughout the structure. The folate substrate is shown in green. The NADP+ cofactor is shown in red. The active site of the enzyme is in the middle of the image where the nicotinamide ring of NADP+ is close to the pterin ring of the folate. (PDB: 1RX2)

Section 4.2 Temperature-Jump Studies on DHFR

We chose to apply the temperature-jump technique to study three inactive DHFR complexes: DHFR•NADP+, DHFR•Folate, and DHFR•NADP+•Folate. It is useful to use the inactive complexes because they allow for more easily creating a stable equilibrium and simplify data analysis by reducing the number of possible pathways. DHFR•NADP+ is mimic of the cofactor bound sate in the reaction pathway. The DHFR•NADPH binary complex could also have been utilized for this purpose, but using the oxidized form reduces the possible spectroscopic interactions and therefore allows for simpler data analysis. The DHFR•Folate (DHFR•Fol) complex mimics the product bound state of the reaction. The ternary complex DHFR•NADP+•Folate (DHFR•NADP+•Fol) is a good mimic of the ternary complex or Michaelis state of the reaction cycle. While all complexes may populate each of the three major Met20 conformers, dominant conformers can be assigned for each of these complexes. The DHFR•NADP+ and DHFR•NADP+•Fol are dominantly in the closed conformation. The DHFR•Fol complex is dominantly in the occluded conformation.[162, 175] These three conformations will allow us to investigate the loop kinetics from different points in the reaction and from different loop states.

Equilibrium Fluorescence

We first performed equilibrium fluorescence measurements on these complexes to determine the sensitivity of their fluorescence to changes in binding equilibrium when altered by temperature. All equilibrium fluorescent measurements were carried out at temperatures from 6 to 60 °C with a data point taken every 3 °C. A 3 minute equilibration period was given after the heat exchange unit reached the desired temperature. The spectra for the DHFR•Fol samples were collected on a Horiba Jobin Yvon (Edison, NJ) Spex Fluoromax-3 fluorimeter with 1 nm resolution, a 1.00 nm excitation slit width, a 2.00 nm emission slit width, a 0.5 s integration time, and with 280 nm excitation light. The spectra for the DHFR•NADP+ and for the DHFR•NADP+•Fol sample were collected on a Horiba Jobin Yvon (Edison, NJ) Dual-FL fluorimeter using a fixed CCD array detector with 1 nm resolution, 5.00 nm fixed slits widths, a 0.2 s integration time, averaging of 3 scans, and with 280 nm excitation light. All samples contained 3 μM of DHFR mixed with 6 μM of the accompanying ligands. The buffer used for all studies was 50 mM sodium phosphate and 100 mM NaCl at a pH of 7.1. Folic acid dihydrate, NADP+ hydrate, and buffer components were obtained from Sigma-Aldrich (St. Louis, MO). Figure 4.5 shows normalized integrated peak intensity of the tryptophan emission peak between 322 and 387 nm for each of the complexes at various temperatures.

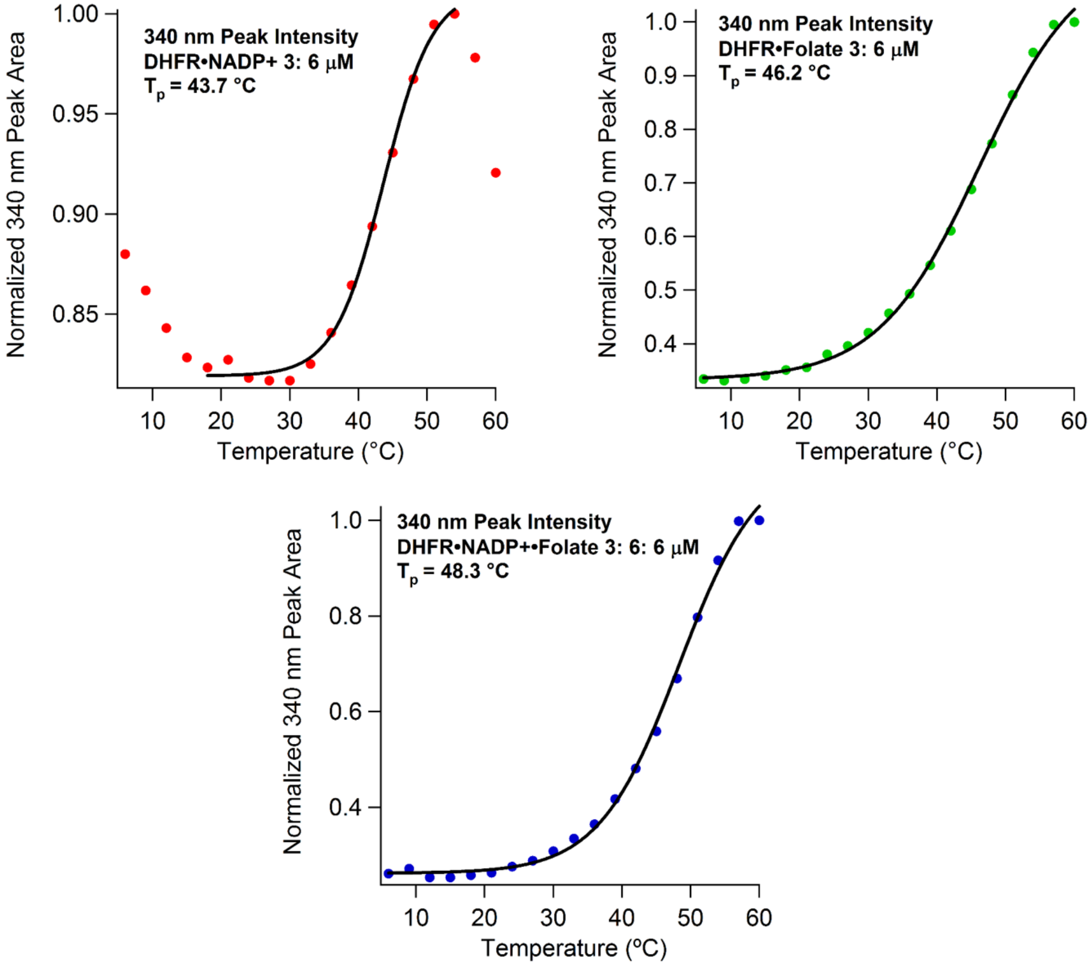

Figure 4.5: Temperature-dependent fluorescence of DHFR complexes. The integrated 340 nm peak intensity at each temperature is shown as round marker. A sigmoid fit of the major transition for each data set is shown in black. The intensity of the tryptophan fluorescence for all complexes increases with temperature because the bound ligand is being released and quenching is reduced. The intensity change in the DHFR•NADP+ tryptophan fluorescence is much smaller than in the other two complexes. The intensity also starts to decay at a lower temperature due to reduced thermal stability.

All three of the studied DHFR complexes show an increase of tryptophan emission with temperature. Upon binding of ligands to DHFR, the tryptophan emission is quenched. In the case of folate this is partially due to energy transfer, but in both cases there is change due to a substrate-induced conformational change.[159] The additional mechanism for quenching in cases with folate explains the larger change in fluorescence compared to the oxidized cofactor binary complex. As the temperature is increased, the equilibrium constants of these complexes shift toward the unbinding of substrate; therefore, our observed increase in fluorescence in intensity is explained by the decrease in quenching interactions as the substrate is driven off of the protein with increased temperature.[176] The three complexes exhibit transition points (T_p) in their fluorescence increases in the range of 40-50 °C, see the values shown in figure 4.5. These transition points are slightly below the published value of melting temperature for the apoenzyme of 49.3 °C.[177] Furthermore, they are likely more significantly below the melting temperatures of the protein complexes given that the binding of substrates tends to increase the thermal stability of the protein.[178] The DHFR•NADP+ shows two unique features. The first is the initial decrease in fluorescence intensity with temperature. We are unsure of the nature of this transition, but it is repeatable and indicates a lower temperature limit for normal enzyme function. The second unique feature is the decrease in fluorescence intensity around 50 °C. This transition is the protein unfolding after ligand release. The other complexes would show a similar unfolding-induced decrease in fluorescence at higher temperatures. The differences in the melting points for the complexes can be explained by previously reported decreased thermal stability of cofactor binding compared to substrate binding.[176] The DHFR•NADP+ complex loses its ligand at a lower temperature and is therefore able to unfold at a lower temperature compared to the other complexes studied. The fluorescence response to temperature of all the complexes is consistent with a model for unfolding where the ligands unbind prior to significant protein structure collapse. As such, we should expect that the temperature-jump will shift the equilibrium of the complexes away from binding, and we will observe this change as an increase in fluorescence signal.

Temperature-Jump Kinetics

Temperature-jump relaxation experiments were carried out on a custom-built instrument. A similar instrument has been described previously; the major difference is the source of the heating pulse.[179] The temperature-jump pump pulse is created by a Q-switched, Tm: fiber-pumped Ho:YAG laser, run at 50 Hz to create a 7 mJ, approximately 10 ns pulse of 2090 nm light (AQS-Ho-YAG, IPG Phototonics Corporation, Oxford, MA). The repetition rate of these pulses is further reduced to 12.5 Hz by an optical chopper (Thorlabs Newton, NJ). The probing method is tryptophan emission excited around 280 nm. The excitation source is the quasi-continuous frequency-tripled output of a Mira 900 Ti:Sapphire laser (850 nm) pumped by a Verdi V12 DPSS high-power laser (Coherent, Santa Clara, CA). The sample emission is focused through an appropriate bandpass filter (Semrock, Rochester, NY) before being measured on a Hamamatsu R7518 photomultiplier tube (Hamamatsu Photonics K. K., Hamamatsu City, Japan). The signal is collected, digitized, and averaged (2000 shots) using a Teledyne LeCroy Wavesurfer 62Xs-B oscilloscope (Chestnut Ridge, NY). Data collection is managed by an in-house routine using the LabVIEW computer program (National Instruments, Austin, TX). The sample thickness is 250 µm. To maintain an even transmittance of the pump pulse through this spacer thickness, the pump beam is split using a 50/50 beamsplitter (Thorlabs) and oriented to heat the sample from both sides. All of the temperature-jump experiments described below utilized a sample containing 200 µM of DHFR and appropriate ligand, unless otherwise noted, in a 50 mM sodium phosphate and 100 mM NaCl D_2O buffer at a pH of 7.1.

Figure 4.6 displays the temperature-jump relaxation transients and the corresponding temperature-dependence of the observed rates for each of the three complexes studied. In all cases, the reported fluorescence signal is the difference between the listed sample transient and a reference tryptophan solution. Subtracting out a reference transient is necessary because the quantum yield of tryptophan fluorescence has an intrinsic temperature dependence causing it to drop with increasing temperature. By taking the difference of the sample and reference spectrum, we are able to effectively eliminate this intrinsic change from our spectra and focus on signal changes due to protein-related dynamics. Under these conditions, the cooling of the sample after the temperature-jump begins to occur on the millisecond timescale. The cooling phase of the sample and reference fluorescence transients is similar enough up to the 5 millisecond timescale that we can subtract out this effect. Furthermore, the theoretical limit of the instrument in early time is the timescale of the heating pulse. In this case, that limit is approximately 10 ns. We can increase the overall observed signal size by altering the terminating resistor used to generate the signal on the oscilloscope. As we increase the terminating resistor, we increase the observed signal voltage (Ohm’s Law). However, this increase in resistance also increases the RC time constant and response of the system.

A careful balance must be chosen with the terminating resistance to maximize signal, but not lose early timescale effects. For all complexes shown here, we varied conditions to be sure of the earliest observable event. We could not detect any transient phases prior to 10 µs. Thus, our conditions were chosen to maximize signal between the observation window of 10 µs and 5 ms.

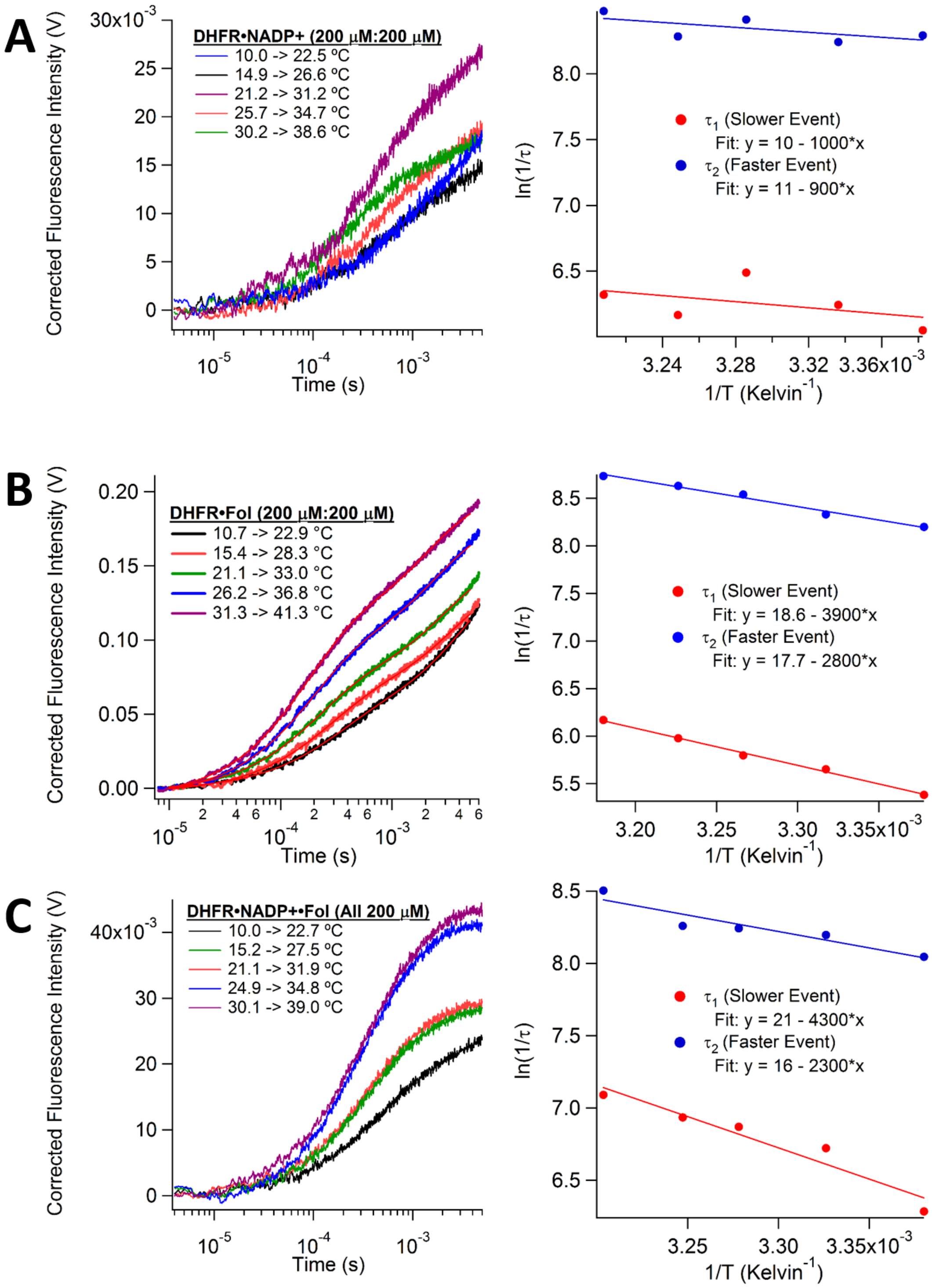

Figure 4.6: Temperature-jump transients of DHFR complexes. The temperature-jump transients at various final temperatures (left) and the temperature-dependence of the observed rates (right) is shown for (A) DHFR•NADP+, (B) DHFR•Fol, and (C) DHFR•NADP+•Fol.

The fluorescence temperature-jump transients of all three complexes fit better to a double exponential curve than to a single exponential curve. This indicates that there are at least two relaxation times in each system. The minimum model required for two relaxation times includes three states (see section 2.2). The dominant state in each complex should be the ligand-bound state after it has undergone its conformational change; therefore, the simplest model to describe these three states would include the free enzyme state, the preconformational change ligand-bound state, and the postconformational change ligand-bound state (scheme 4.1). The observed increase in fluorescence signal for all complexes is line with our interpretation of the equilibrium fluorescence measurements described above.

Scheme 4.1

$$E + L \underset{k_{-1}}{\overset{k_1}{\leftrightarrow}} E^1L \underset{k_{-2}}{\overset{k_2}{\leftrightarrow}} E^2L$$

Evaluation and identification of the relaxation rates is a more complicated task. Tables 4.1, 4.3, and 4.5 list the rates determined from nonlinear least squares regression fits to the data shown in figure 4.6. Inspection of the listed rates reveals that the relaxation times are only ever a little more than an order or magnitude different than each other. This would indicate the rates are coupled to each other under these conditions. Another indication of this coupling is the fact that two rates are observed at all. If one rate was much faster than the other, we would only be able to observe the slower rate-limiting step. This coupling makes extraction of the actual rate constants difficult from the data without a complicated model to account for coupling. We can infer from data taken at various concentrations (see tables 4.2, 4.4, 4.6, and 4.7) which relaxation rate is more concentration-dependent; in all cases the faster rate is more sensitive to changes in concentration. Since the bimolecular step should be, despite coupling, more sensitive to concentration, we can conclude that the faster rate is dominated by the bimolecular step. The identity of the bimolecular step is straightforward in the binary complexes because there is only one possible ligand to be lost from the protein; however, the identification of the ligand lost in the ternary complex experiment is more complicated. If we study the temperature-dependence of the relaxation rates (slopes of the linear fits in figure 4.6), we observe that the temperature-dependence of the DHFR•NADP+•Fol complex is more similar to the temperature-dependence of the DHFR•Fol complex. This observation is in-line with the predicted reaction cycle of the protein as well. Both the DHFR•NADP+ and DHFR•NADP+•Fol complexes are dominantly in the closed conformations which indicates they are more reactant-like states. Therefore, the release of the folate from the ternary complex would be more like a reversal of the natural reaction cycle as opposed to release of the cofactor which would be similar to mimicking the product-side of the reaction cycle. Again, we do not expect to mimic the product-side of the cycle because the ternary complex is more reactant-like.[172, 175]

Table 4.1: Temperature-Jump Relaxation Rates for DHFR•NADP+

T_{final} (°C)	**$1/\tau_1$ (Hz)**	**$1/\tau_2$ (Hz)**
22.5	420 ± 30	4000 ± 300
26.6	540 ± 40	3800 ± 200
31.2	660 ± 40	4500 ± 200
34.7	480 ± 30	4000 ± 100
38.6	560 ± 60	4800 ± 100

Table 4.2: Concentration-Dependence of Rates for DHFR•NADP+
(DHFR concentration is 200 μM in all cases. Final temperature is 30 °C)

[NADP+] (μM)	$1/\tau_1$ (Hz)	$1/\tau_2$ (Hz)
100	500 ± 50	2800 ± 200
150	600 ± 40	3500 ± 200
200	520 (Calculated from temperature-dependent data)	4200 (Calculated from temperature-dependent data)
300	460 ± 50	4600 ± 200

Table 4.3: Temperature-Jump Relaxation Rates for DHFR•Fol

T_{final} (°C)	$1/\tau_1$ (Hz)	$1/\tau_2$ (Hz)
22.9	220 ± 10	3640 ± 60
28.3	280 ± 10	4160 ± 50
33.0	330. ± 9	5120 ± 50
36.8	395 ± 8	5600 ± 40
41.3	478 ± 8	6220 ± 40

Table 4.4: Concentration-Dependence of Rates for DHFR•Fol
(DHFR concentration is 200 μM in all cases. Final temperature is 31 °C)

[Fol] (μM)	$1/\tau_1$ (Hz)	$1/\tau_2$ (Hz)
100	220 ± 30	2630 ± 50
150	400 ± 20	4000 ± 40
200	260 ± 10	4730 ± 60

Table 4.5: Temperature-Jump Relaxation Rates for DHFR•NADP+•Fol

T_{final} (°C)	**$1/\tau_1$ (Hz)**	**$1/\tau_2$ (Hz)**
22.7	540 ± 40	3100 ± 100
27.5	830 ± 50	3630 ± 90
31.9	960 ± 50	3800 ± 100
34.8	1000 ± 50	3860 ± 90
39.0	1200 ± 30	4900 ± 100

Table 4.6: NADP+ Concentration-Dependence of Rates for DHFR•NADP+•Fol
(DHFR and Fol concentrations are 200 µM in all cases. Final temperature is 29 °C)

[NADP+] (µM)	**$1/\tau_1$ (Hz)**	**$1/\tau_2$ (Hz)**
100	230 ± 40	3600 ± 200
150	340 ± 40	4200 ± 300
175	330 ± 50	4900 ± 300
200	360 ± 40	4400 ± 300

Table 4.7: Fol Concentration-Dependence of Rates for DHFR•NADP+•Fol
(DHFR and NADP+ concentrations are 200 µM in all cases. Final temperature is 29 °C)

[Fol] (µM)	**$1/\tau_1$ (Hz)**	**$1/\tau_2$ (Hz)**
100	530 ± 70	2900 ± 200
150	440 ± 70	2300 ± 300
175	290 ± 50	3500 ± 300
200	360 ± 40	4400 ± 300

The temperature-jump data and corresponding analysis indicate that the typical approach to DHFR kinetics which ignore the conformational change are insufficient to fully describe the system.[159] Applying previously determined rate constants and equilibrium constants to our experiments above would predict relaxation rates in-between what we observed (e.g. approximately 1000 s^{-1} for both binary complexes at 25 °C) .[159, 176, 180] This disagreement is because the stopped-flow methods used previously could not distinctly detect the rate of the conformational change. While strongly coupled, there is a distinct conformational state between the substrate binding and the Michaelis state. The rate constants of substrate binding and conformational change (loop motion) have yet to be determined. What we have shown here is that while others may have focused on developing new probes for studying DHFR, it is possible to observe these events with the native protein.[181-183] Future studies collecting a large set of concentration-dependent data could be used to build and solve a kinetic scheme that allows for quantifying these rate constants.

Section 4.3 Microfluidic Fast Mixing Applied to DHFR

One method to simplify the analysis of DHFR kinetic data would be to use our microfluidic fast mixer described in section 2.3. The drastic change in equilibrium concentrations initiated by mixing simplifies the data analysis because the forward rates dominate the kinetics. With our current system there are significant limitations for the DHFR system. The outer capillary of our mixer has an inner diameter of 200 µm while the sample stream has a diameter of approximately 2-5 µm. That means that the optical pathlength of the sheath stream is more than 40x greater than the optical pathlength of the sample stream. If the substrate used to initiate mixing has even a small fraction of the same response to the probing method, it will prevent observation of changes in the sample stream as distinct from the background. This is the case with nearly all of the natural fluorophores in the DHFR system. Both folate and dihydrofolate weakly absorb 280 nm and 340 nm light and weakly emit broadly around 400 nm. The optical properties of the cofactors are also disruptive because, while not nearly as favored as the 340 nm excitation for 450 emission, the 260 nm absorption band of the cofactor can induce mid-400 nm emission as well.

One option that remains for mixing experiments of this kind is to use methotrexate. Methotrexate is a substrate inhibitor believed to force the enzyme into a transition-state-like structure when it binds to a DHFR•cofactor (reduced or oxidized) binary complex. Methotrexate itself is not a transition-state analog, but alters the conformation of the enzyme into a disordered state believed to be populated prior to hydride transfer.[162, 174] Upon binding to the enzyme, methotrexate (MTX) quenches the intrinsic tryptophan fluorescence by about 80-90 % due mainly to an energy transfer mechanism.[180, 184] MTX will quench the tryptophan fluorescence of the DHFR•NADPH complex by approximately 60 %.[184] The signal to noise ratio of this experiment can be maximized by following the reaction by FRET from the enzymatic tryptophan to the cofactor. Solution contaminants and optical components, the main component of background fluorescence in this experiment, are much less likely to emit around 450 nm than 340 nm when excited by 280 nm light. In this proof of concept study we used a saturating concentration of MTX (500 µM) to mix with a 200 µM DHFR and 300 µM NADPH solution. The sheath flow rate was set to 1 mL/min and the inner flow rate was set to 0.1 µL/min. Under these conditions, the mixing time should be less than 100 µs and the binding of MTX should be diffusion-limited.[93, 184] The excitation source for this study was the frequency tripled output from a Coherent (Santa Clara, CA) Mira

Ti:Sapphire laser run at 82 MHz centered around 850 nm pumped by a Coherent Verdi-V12. Excitation light was filtered with a bandpass filter centered at 280 nm. Emission was filtered with a bandpass centered at 450 nm. The excitation light was focused on the sample through a 40x UV focusing objective from Thorlabs (Newton, New Jersey). The emission light was collected through the same objective and reflected through the emission bandpass filter and collected on a Hamamatsu (Bridgewater, NJ) C9100-14 ImageM-1k EM-CCD camera. A typical exposure time for this system is approximately 3 seconds with a gain setting of 1 and an intensification setting of 255. The CCD array was actively cooled to -57 °C. Sample solutions were at room temperature for mixing experiments, approximately 22 °C. Figure 4.7 shows the mixing transient of this reaction.

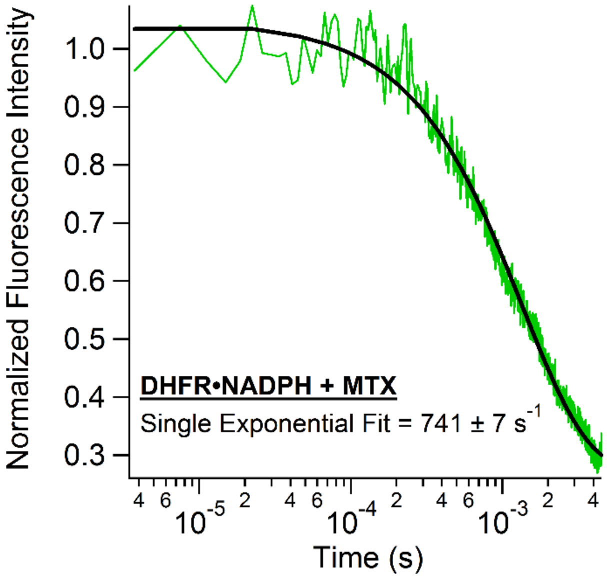

Figure 4.7: The mixing transient of DHFR•NADPH with MTX. The mixing time and binding of the substrate should be well below 100 μs. The observed signal change is fit to a single exponential curve and should only represent conformational change.

The mixing transient shown in figure 4.7 fits well to a single exponential curve. Since substrate binding should be much faster than the 741 s^{-1} fit rate under these conditions, we can be confident that the observed rate is only related to substrate-induced conformational change. The straight-forward interpretation of these data gives a reliable estimate of the timescale of loop motion in DHFR upon mixing with MTX. It is quite possible that the conformational changes associated with other loop motions is different than this rate. The slow rate from the temperature-jump studies discussed above is slower than the rate observed from mixing studies. This difference may be revealing that the rate of loop motion is a function of ligand identity, but other factors besides substrate identity could explain the discrepancy (e.g. different kinetic approach). A more thorough analysis of loop closure rates and ligand identity is needed. The labeling studies referenced earlier may allow for mixing studies to play a more significant role in DHFR rate constant determination by increasing the number of substrates that can be mixed in our mixer.[181-182] Another approach would be to shift to a more traditional 2D, or sandwich-style, microfluidic mixer to get rid of sheath optical screening altogether.[185] Some combination of these techniques, either with additional modeling or protein variants, will allow for a more complete understanding of DHFR loop kinetics. These methods will then allow important questions to be answered about the role of coordinated motions in the catalysis of DHFR.

Chapter 5. Purine Nucleoside Phosphorylase

Section 5.1 Introduction to Purine Nucleoside Phosphorylase

Purine nucleoside phosphorylase (PNP) is a ubiquitous enzyme that is important for the salvage of purine bases from nucleosides. PNP takes the ribo- or deoxyribo-nucleoside form of a purine and an inorganic phosphate molecule to form the ribose or deoxyribose-1-phosphate and the purine base (fig. 5.1). The enzyme functions with varying specificity, by organism, for adenosine, guanosine, and inosine. PNP energetically favors the synthesis of purine nucleosides but is physiologically coupled to more energetic processes to be driven in the direction of phosphorolysis. The PNP-driven formation of purine bases is a critical route for purine stasis particularly in tissues and cells where synthesis is not favored, e.g. kidneys, lymphocytes, and erythrocytes.[186]

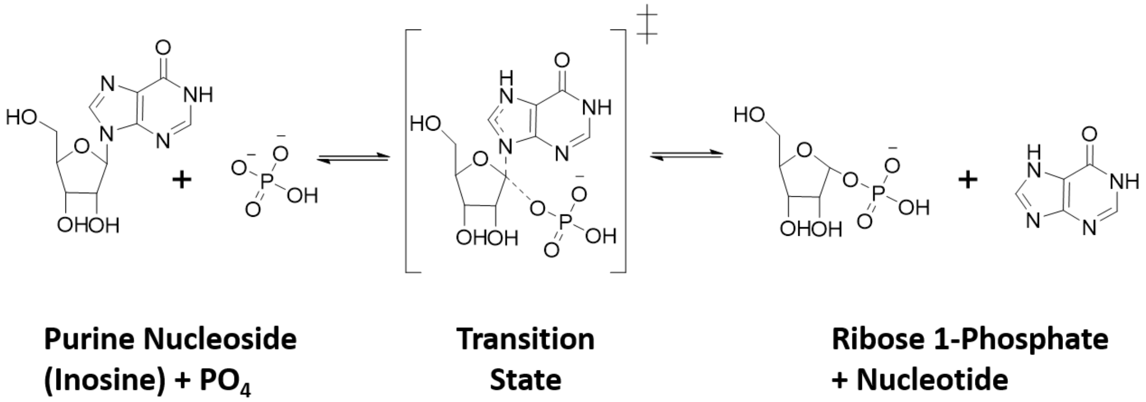

Figure 5.1: Chemical structures of PNP relevant compounds. PNP catalyzes the phosphorolysis of purine nucleosides to form a phosphorylated sugar and a purine base. This example is shown with the nucleoside inosine and a ribose sugar. PNP enzymes can also function on adenosine and guanosine as well as deoxyribose sugars depending on species of origin.

The dependence on PNP for maintaining proper physiological purine concentrations, and therefore for cell proliferation, has made PNP an ongoing drug target.

Specifically, a deficiency in PNP activity has been linked to defective T-cell immunity.[187-189] Therefore, diseases and conditions caused by overactive T-cell responses or associated with T-cell responses, such as T-cell lymphoma, T-cell leukemia, rheumatoid arthritis, lupus, and organ transplant rejection, have potential to be treated by targeted PNP inhibition.[190-191] Inhibiting PNP can aide in the treatment of some metabolic disorders, like hyperuricemia, because the production of purine bases by PNP can act as an antecedent to uric acid production.[192] Finally, PNP has also been linked to the decrease in effectiveness of some chemotherapeutic nucleoside-like cytotoxic compounds. The abundance of PNP in humans leads to significant breakdown of these nucleoside analogues even when PNP has very low activity on them.[190, 193] The multifaceted application of a high-affinity, highly-effective PNP inhibitor drives research not only into new inhibitors, but in understanding their mechanism of inhibition.

Inhibitor design has developed in stages around searching for structural similarity. Early attempts at inhibitor design were focused on finding appropriate analogues of the nucleoside substrates. While successful at inhibiting the enzyme, the K_i of 200 nM for 8-aminoguanine was insufficient to meet the projected K_i value of < 10 nM necessary for PNP inhibition at reasonable inhibitor concentration given the high concentration of PNP in humans.[190-191, 194] Later attempts focused on the crystal structure of the enzyme and iteratively comparing Monte Carlo-based conformational searches for inhibitor candidates with their measured IC_{50} values.[195] While this approach showed improvement, attaining K_i values in the nanomolar range, further progress was necessary for significant reduction in T-cell activity.[196] A particularly successful approach has been to design inhibitors based off the transition-states structure of the enzyme (fig. 5.2).

Immucillin-H (Imm-H) is an inhibitor designed with this approach. Imm-H is shown to have a picomolar level, K_i = 58 pM, of inhibition.[196-197] While Imm-H effectively binds to the enzyme, there is a significant entropic penalty to its binding because it minimizes the distance between the ribocation and the purine leaving group and decreases the inherent flexibility of the enzyme's catalytic site.[31] Further development in transition-state mimics has focused on maintaining the enzyme's flexibility. One of the successful inhibitors developed in this way was 4'-deaza-1'-aza-2'-deoxy-1'-(9-methylene)-Immucillin-H (DIH). DIH has a significantly stronger K_i of 9 pM.[197] The work presented below focuses on DIH and its effect on the larger scale motions of PNP's loops vs the natural substrate inosine.

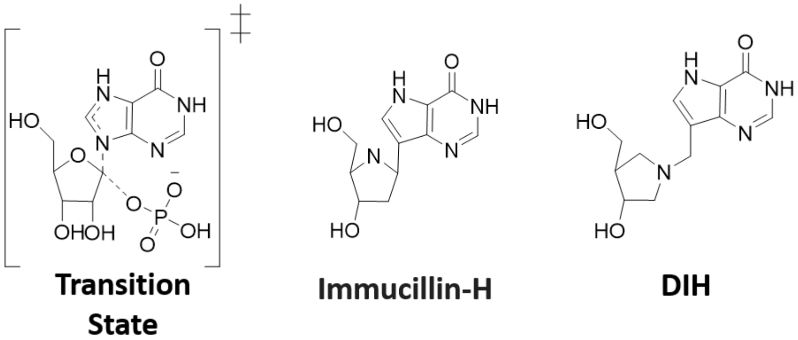

Figure 5.2: Chemical structures of PNP inhibitors. The chemical structures of the transitions-state mimics Immucillin-H and DADMe-Immucillin-H (DIH) compared to the inosine transition-state structure of PNP. The extra flexibility of DIH decreases the entropic penalty of protein inhibition compared to Immucillin-H and leads to a stronger binding constant.

The substrate-binding induced conformational change that occurs in PNP is characterized by the motion of three loop sections. Human PNP exists as a homotrimer (fig. 5.3). Two of the loop sections, loops 1 and 2, are positioned on the same enzyme monomer as the active site they interact with, but loop 3 is on an adjacent monomer to the active site monomer it interacts with. Loop 1 changes from an unstructured loop to an α-helical segment. This change also moves His257 about 15 Å so that the imidazole ring can provide electrostatic stabilization for the ribocation of the transition-state. Loop 2 makes a change from an α-helix into a loop to reposition an imidazole ring approximately 17 Å, this time of His64, so that it can stabilize the phosphate in the substrate-bound complex. Loop 3, which includes Phe159, makes a significantly smaller conformational change to help provide a hydrophobic cover for the active site along with the other two loops described above.[31, 197-198] Despite the essential functions that these loops are known to perform, little is known about the timing and coupling of the loops with respect to the chemistry step of the catalytic cycle.

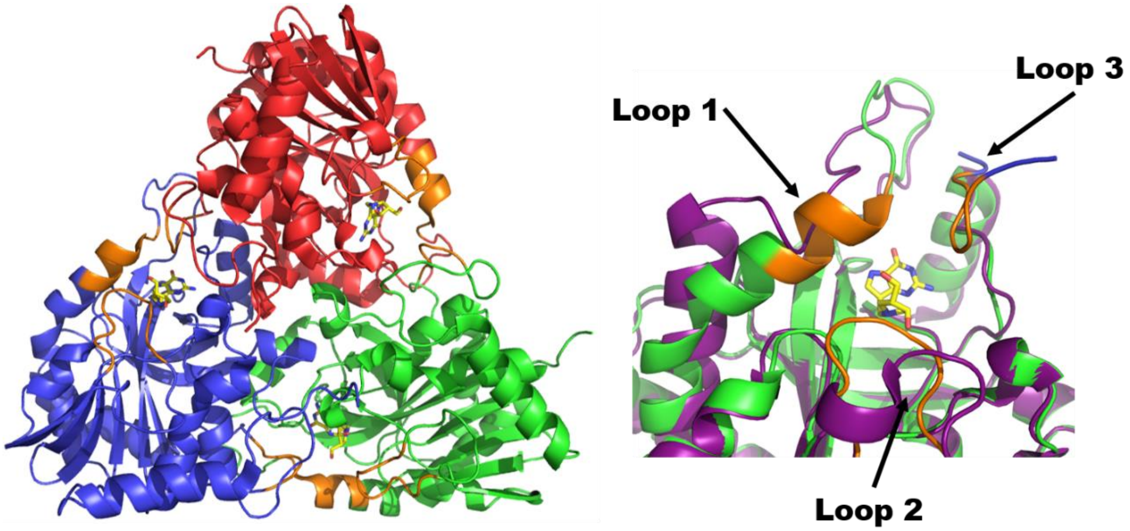

Figure 5.3: Crystal structures of PNP. The left image shows the trimeric state of PNP. The three monomers are colored red, blue, and green. The loops in each structure are orange. The bound substrate is yellow (PDB: 3PHB). The image on the right emphasizes the three loops described in the text with relation to the active site and contrasts the positions of loops 1 and 2 with their analogues in the substrate-free structure in purple (PDB: 1M73). Loop 3 is primarily shown in blue, same coloring as the image on the left, to emphasize that it from an adjacent PNP monomer.

In addition to the structural role of PNP's loops that has been inferred from crystal structures (fig. 5.3), the information known about the coupling of PNP's loop motions to catalysis has come from fluorescence temperature-jump spectroscopy and NMR labeling studies. The wild-type structure of PNP has three tryptophans distributed throughout the structure. Tryptophan is a natural fluorophore, but the locations of these tryptophans does not allow for obvious assignment of observed spectroscopic signals. To create a more informative fluorescent version of PNP, the three tryptophans can be mutated to tyrosine and then tryptophans mutations made at more useful locations. The tryptophan free version (Leuko-PNP) has been studied and shown to exhibit similar reaction kinetics to the wild-type form.[199]

Three studies using modifications of Leuko-PNP have been used to probe PNP dynamics. First, the mutant Y249W-Leuko-PNP was made to be able to study the substrate binding dynamics with respect to loop 1. This mutant was useful for studying the pre-steady-state substrate binding kinetics, but was unsuccessful as a probe for temperature-jump studies, where the faster loop motions could have been observed, because the substrate-induced change in fluorescence signal was too small.[199] Second, the mutant F159W-Leuko-PNP was used as a site-specific probe to loop 2. A combination of temperature-jump and stopped-flow kinetics studies on this mutant were able to establish a model for the PNP reaction that included several stable conformational states in-between ligand binding and the chemistry step of the reaction cycle. It is believed that these conformational changes reorganize the enzyme active site to prepare it for the catalytic event.[90] Third, two different mutant versions of the protein with one tryptophan each H257-6FW-Leuko-PNP and H64-6FW-Leuko-PNP were made to introduce site-specific NMR labels in to the enzyme. 6FW is a fluorinated version of tryptophan that allows for ^{19}F-NMR to be useful for protein structure analysis. The chemical shift and line shape analyses of this NMR data showed that when a transition-state mimic binds to the protein, the loops collapse from a flexible conformational distribution into a much tighter set of conformations. This observation implies that crossing the reaction barrier requires both a conformationally flexible protein and a specific set of defined chemically-ready states.[198] Together these three studies uncovered the importance of a pre-chemistry conformational search involving the three loops of PNP, but did not allow for a definitive description of this search. To this end, we utilized three mutants of Leuko-PNP that would allow for observing the kinetics of each loop during the conformational search. We describe the application of our microfluidic fast mixer to studying these kinetics in the next section.

Section 5.2 Microfluidic Fast Mixing Studies of PNP

We set out to study the conformational search of human PNP between its substrate-binding step and its chemistry step. To study this search we utilized three variations of the Leuko-PNP construct described above. The H257W-Leuko-PNP mutant should act as a site-specific fluorescence probe for loop 1, the H64W-Leuko-PNP mutant should report on loop 2, and F159W-Leuko-PNP mutant should report on loop 3. These mutant proteins were produced as previously described.[90, 198-199]

We used the microfluidic fast mixer described in section 2.3 of this work to initiate the substrate binding of inosine or the transition state mimic DIH with the various mutants of human PNP. In each case, 180 µM of a PNP variant in a 50 mM PO_4 buffer at pH 7.4 was flowed in the inner capillary of the mixer. The substrate flowed in the outer capillary of the mixer. Various concentrations of inosine were used as noted below but no concentration-dependence of the transient signals was observed. The probing method was tryptophan fluorescence. The excitation source was the frequency tripled output from a Coherent (Santa Clara, CA) Mira Ti:Sapphire laser run at 82 MHz centered around 850 nm pumped by a Coherent Verdi-V12. Excitation light was filtered with a bandpass filter centered at 280 nm. Emission was filtered with a bandpass centered at 357 nm. The excitation light was focused on the sample through a 40x UV focusing objective from Thorlabs (Newton, New Jersey). The emission light was collected through the same objective and reflected through the emission bandpass filter and collected on a Hamamatsu (Bridgewater, NJ) C9100-14 ImageM-1k EM-CCD camera. Images were collected with various exposure times to maximize signal, but a typical exposure time was 30-60 seconds with a gain setting of 1 and an intensification setting of 255. The CCD array was actively cooled to -57 °C. A reference data set was also collected for each mixing study where buffer was flowed in the outer capillary instead of substrate. The fluorescence signal of the sample data set, where substrate was flowed, was divided by this reference data set to correct for changes in the fluorescence signal due to the physical interaction between the inner and outer capillary fluids. This correction allows only the chemical interaction to be studied. Experiments were carried out at room temperature, approximately 22 °C.

The human PNP mutant H257W-Leuko-PNP was intended to study the conformational changes of the protein specific to loop 1. As the flow transient shows in figure 5.4, we observed no significant change in the fluorescence signal as induced by mixing with inosine. This was also true when the protein was mixed with DIH. A similar result was obtained from previous temperature-jump studies utilizing the mutant Y249W-Leuko-PNP.[199] A change in fluorescence signal would be expected as the tryptophan moves from a more solvent-exposed environment to the protein environment.[200] One possible interpretation is that the protein's conformation change does not affect these two residues' exposure to solvent. Upon inspection the crystal structures of the purine-free and purine-bound protein, PDB: 1M73 and 3PHB respectively, it does appear that the position of residue 249 does not change very much as it is on a peripheral section of loop 1; however, residue 257 is in the section of the loop 1 that changes from a unstructured loop to an α-helix. As described above, this change moves the imidazole ring of the histidine residue at position 257 approximately 15 Å and swings the imidazole right into the active site where it is in position to make necessary contact with the substrates. Further, the H257W mutant has already been shown to act as a reporter for conformational flexibility.[198] It is possible that a combination of instrument noise and weak tryptophan fluorescence sensitivity to this specific environmental change can explain the lack of observed signal change. The change in loop 1 is also likely to be outside the observation window, probably slower, of this mixer. This is a reasonable conclusion because we know that the chemistry step is fast, but its rate is limited to 200 s^{-1} by slower conformational motions.[90] Follow-up studies using more sensitive fluorescent probes with larger overall signals and changes in signal could allow for an observation of loop 1 conformational changes by fluorescently-probed mixing. Instruments with longer observation windows, like stopped-flow, could also be useful in determining the timescale of loop 1 motions.

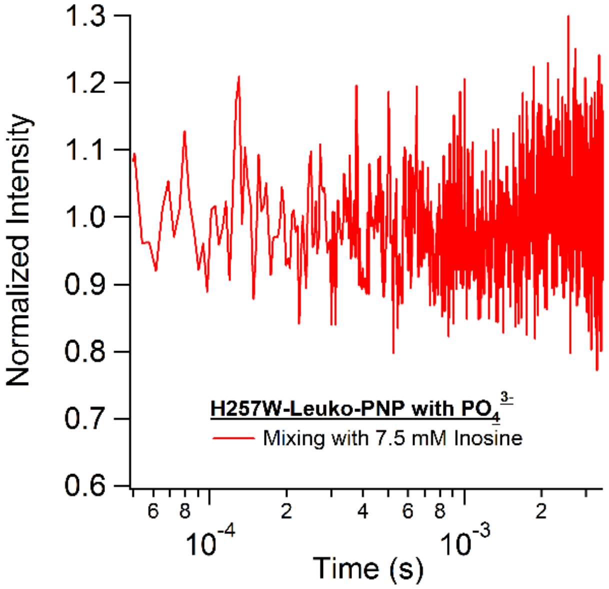

Figure 5.4: Fluorescence mixing transient of H257W-Leuko-PNP with phosphate and inosine. The mixing transient shows that when inosine is rapidly mixed with H257W-Leuko-PNP and phosphate ions there is no observable change in fluorescence signal. This is unexpected because previous studies have shown that this residue is a good reporter of substrate-induced conformational changes in the protein.[198] See the text for a discussion of possible explanations.

To study the dynamics of loop 2 of human PNP, we mixed F159W-Leuko-PNP and phosphate with inosine (fig. 5.5). Unlike the transient showed for the H257W mutant, there is a definite change in signal observed in this data. The signal change observed for the H64W variant is an increase in fluorescence intensity with a rate of 1600 s^{-1}. The increase in fluorescence is expected because the crystal structure data on the protein, same PDB files as discussed previously, indicate that His64 moves from a solvent exposed state to being buried in the active site of the enzyme. The shift from an aqueous environment to the more hydrophobic environment of the protein interior tends to blue-shift the fluorescence and increase its intensity. [200-203] This rate is on a similar timescale, 2200 s^{-1}, to previous observations of conformational change rates in human PNP as studied by temperature-jump spectroscopy.[90] As these temperature-jump studies dealt with a site-specific probe of loop 3, we may expect the observed rates to vary. We may also expect a difference due to the difference in experimental method. The observation of this rate specific to loop 2 is the first direct observation of the kinetics of loop 2 in PNP.

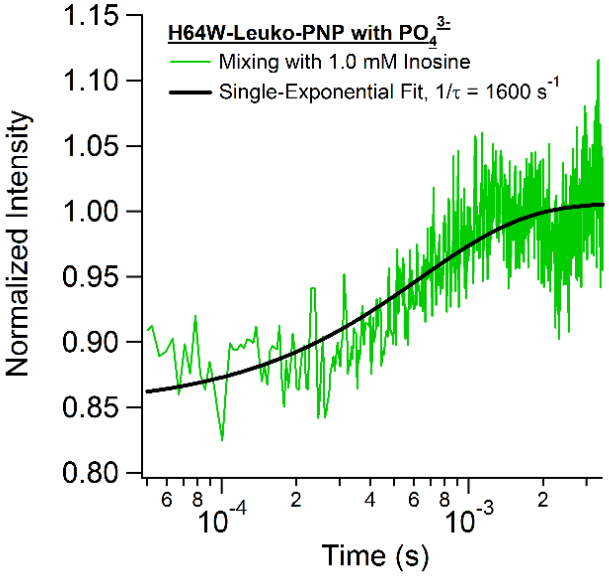

Figure 5.5: Fluorescence mixing transients of H64W-Leuko-PNP with phosphate and inosine. The binding of inosine to the H64W mutant induces a conformational change that increases the observed tryptophan fluorescence.

The final mutant version of PNP we studied by mixing was F159W-Leuko-PNP. This mutant reports on loop 3, which is the loop that is provided by an adjacent PNP monomer. We mixed the F159W-Leuko-PNP mutant with both inosine and DIH (fig. 5.6). Our mixing studies showed a significant decrease in tryptophan emission intensity when either substrate or inhibitor are mixed with the protein. In the case of mixing with inosine, transient change can be fit to a rate of 1130 s^{-1}. This rate is slower than what is reported by temperature-jump experiments on the same complex using the same probing method. The temperature-jump studies observed two post-binding fluorescence signal changes, one with a 10500 s^{-1} rate and one with a 2200 s^{-1} rate. The faster rate is not observed because it would overlap with the approximately 90 μs mixing time of the system. The slower rate, 2200 s^{-1}, is likely to be reporting on the same event as our observed 1130 s^{-1} event. As mentioned in the discussion of the H64W, the difference in rates is likely due to the difference in experimental methods. Temperature-jump is a relaxation method and is therefore probing a system already at equilibrium moving to a nearby equilibrium whereas this mixing study is probing a more significant change in reaction conditions. We are likely probing a different path along the reaction landscape, so we are consequently seeing a different reaction rate. However, both the results from the H64W mutant and the results from the F159W mutant are from the same experimental method. The H64W mutant shows a faster rate of fluorescence signal change than the F159W mutant. This can be interpreted to indicate that loop 2 of PNP completes its conformational change prior to loop 3. We can make this conclusion despite the difference in substrate concentration used for mixing because there was no concentration-dependence on the observed rate.

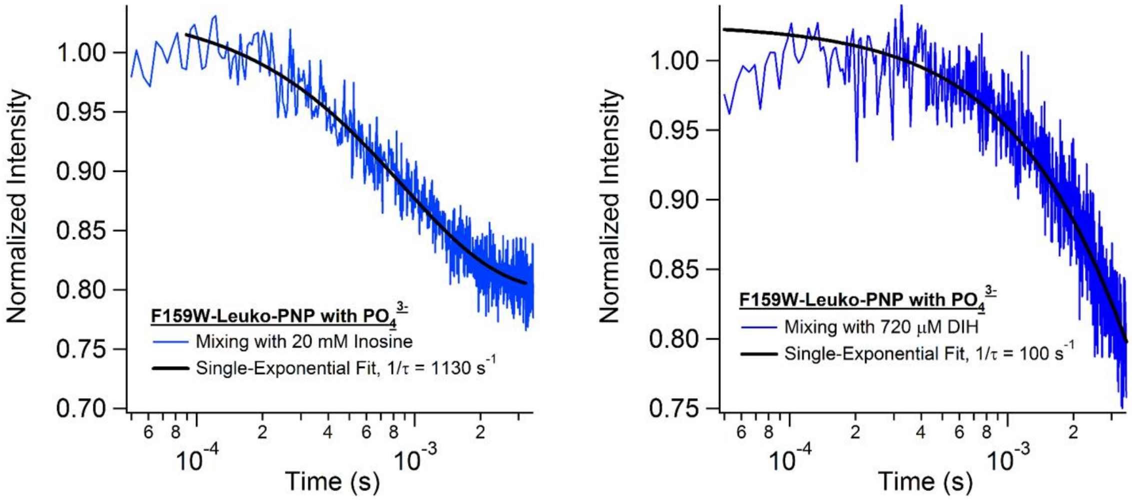

Figure 5.6: Fluorescence mixing transients of F159W-Leuko-PNP with phosphate and inosine or DIH. The image on the left display the fluorescence transient of the mixing of PNP and inosine. The image on the right displays the fluorescence transient of the mixing of PNP with DIH. The mixing transient with inosine shows a substantially faster decrease in signal than the mixing transient with DIH.

In contrast to the mixing transient of F159W-Leuko-PNP and phosphate with inosine, the mixing transient with the transition-state inhibitor DIH displays a much slower change in fluorescence signal. The exponential fit rate shown with the DIH mixing transient is 100 s^{-1}. This is not a realistic rate for the given data because the observation window of this experiment does not extend long enough, 10 ms, in time to observe this event. The line of best fit and its corresponding rate are given here to emphasize the difference in timing of the signal changes depending on the substrate used. Also, even though the concentrations are different between the two substrates, we saw no change in rate of this kinetic event with changes in substrate concentration. A lower DIH concentration was used because it could be, due to a very low K_i, and because using a large concentration of inhibitor is cost-prohibitive. Both the sign and degree of the change in the fluorescence signal is similar between the two mixing experiments. This similarity implies that we are looking at the same event and that they are reaching a similar degree of completeness. It appears from this data that DIH-binding induces a longer conformational search after substrate binding than inosine. This can be understood by the natural evolution of PNP to optimize its reaction progress from the reactant-like substrate and not from the transition-state-like substrate. A different, apparently non-optimized, reaction pathway must be taken to reach the transition-state structure from the inhibitor encounter complex. This change in pathway surely increases the effectiveness of the inhibitor by increasing the interaction time of the protein with the inhibitor and therefore necessarily decreasing the protein's availability to interact with a productive substrate.

Through mixing studies of three different site-specific fluorescent mutants of human PNP, we are able to develop a better understanding of how the loops in PNP function. We were able to observe that loop 2 experiences the substrate-induced conformational change prior to loop 3. By lack of observed signal change with probing loop 1, we have also hypothesized that it is likely to be the final loop to experience the conformational change. Finally, mixing studies with DIH have indicated that one of the ways the inhibitor functions is to disrupt the conformational search process. PNP's loops are designed to function in a step-wise fashion to move the enzyme through the reaction coordinate; alterations to this search disrupt the enzyme's optimization.

Chapter 6. Conclusion

Loop structures can serve a variety of important features in enzymatic catalysis. Loops can serve as binding domains for ligands.[38] Loops can also provide key stabilizing interactions for reaction intermediates during catalysis.[31, 121-123, 172, 197-198] Loops are not unique in these functions. Most enzyme structural features can serve these roles as well. What makes loops unique is their inherent flexibility. This flexibility allows loop structures to fluctuate on the timescale of enzyme reactions and creates dynamic interactions between loops and substrates during the catalytic reaction. For example, loops can vary their stabilizing interactions at different points in the reaction cycle such as to stabilize transition states but destabilize products.[121, 162, 172] Most of these dynamic interactions have only been inferred from crystallographic data or predicted computationally due to the inaccessible timescales of these motions. We have shown in this work that, through the use of temperature-jump relaxation methods to study reactions near equilibrium and microfluidic fast mixing to study reactions far from equilibrium, these motions can be observed directly.

In the case of lactate dehydrogenase, temperature-jump studies indicated that the movement of a small loop section drives the conformational search for necessary stabilizing interactions in the active site. The loop can close to create a variety of stable active sites with varied reactivity, and the dominant substate is not the most reactive. Some reaction pathways may even be non-productive. In contrast, while our fast mixing studies on the same protein were able to more definitely describe the loop kinetics, they do not display the same degree of reaction heterogeneity as the temperature-jump results.

The difference in conclusions indicates the importance of environmental conditions for preferred reaction pathways.

In the case of dihydrofolate reductase, temperature-jump studies reveal for the first time an experimental approach for cataloguing the motions of a catalytically critical loop motion. The direct coupling of this loop to catalysis is inferred from crystallographic studies but has been unable to be studied because of a lack of appropriate experimental approaches.[163, 173] Our approach distinguishes the loop motion from substrate binding which will allow for direct conclusions about the coupling of the loop to catalysis. In a complimentary approach, we show that this loop can also be studied by fast mixing, but to be fully realized, modifications to the approach involving protein labeling or instrument modifications need to be made.

In the case of purine nucleoside phosphorylase, we use fast mixing to establish an order for the motion of its three loop structures upon substrate binding. The order of these loops is key to understanding how the enzyme stabilizes each of its intermediates along the reaction pathway. We have also observed that one of the modes of action of a strong inhibitor for purine nucleoside phosphorylase is kinetic. The binding of the inhibitor appears to alter and slow the conformational search for stability which effectively inhibits the enzyme from more productive substrates.

By examining these three enzymes experimentally we can establish that there exists a complex reaction landscape for each of these systems. For all three systems, a series of substates must be populated for catalysis to occur. With lactate dehydrogenase we were able to observe that the process of populating these states can lead to a variety of productive and non-productive substates. This observation implies an even greater degree of complexity behind enzymatic reaction landscapes. By probing these reactions with different kinetic methods we have been able to see that the choice of method, and therefore the choice of environment, can also change how the landscape is perceived. One can populate different parts of the landscape and explore different reaction pathways just by changing observation methods. To fully map these landscapes, exhaustive experimental studies must be performed.

Understanding the richness of enzymatic reaction landscapes has important implications for work with enzymes. With regards to research in enzyme failure, an important consideration for several medical conditions, understanding the distribution of possible reaction pathways, as observed with lactate dehydrogenase, and how the environment can change this distribution could be crucial. Progress on *de novo* enzyme design will improve as we understand the impact loops, like that of dihydrofolate reductase, can have on optimizing the enzyme for each step of the reaction cycle. In terms of pharmaceutical research, as seen in the case of purine nucleoside phosphorylase, a greater understanding of the substates the enzyme populates can lead to new approaches for drug development. These three examples are just the beginnings of what a better understanding of enzymes could mean for chemical research. It is important to take these conclusions and search for similar motifs in other enzymes using the kinds of experimental approaches described here. Only with a more comprehensive catalog of the role of loops, and enzyme dynamics in general, can we fully realize the potential of enzymes.

References

1. Wolfenden, R.; Snider, M. J., The Depth of Chemical Time and the Power of Enzymes as Catalysts. *Accounts Chem Res* **2001,** *34* (12), 938-945.

2. Bar-Even, A.; Noor, E.; Savir, Y.; Liebermeister, W.; Davidi, D.; Tawfik, D. S.; Milo, R., The Moderately Efficient Enzyme: Evolutionary and Physicochemical Trends Shaping Enzyme Parameters. *Biochemistry* **2011,** *50* (21), 4402-4410.

3. Alberty, R. A.; Hammes, G. G., Application of the Theory of Diffusion-Controlled Reactions to Enzyme Kinetics. *The Journal of Physical Chemistry* **1958,** *62* (2), 154-159.

4. Koenig, S. H.; Brown, R. D., H2co3 as Substrate for Carbonic-Anhydrase in Dehydration of Hco3. *Proceedings of the National Academy of Sciences of the United States of America* **1972,** *69* (9), 2422-&.

5. Ro, D.-K.; Paradise, E. M.; Ouellet, M.; Fisher, K. J.; Newman, K. L.; Ndungu, J. M.; Ho, K. A.; Eachus, R. A.; Ham, T. S.; Kirby, J.; Chang, M. C. Y.; Withers, S. T.; Shiba, Y.; Sarpong, R.; Keasling, J. D., Production of the Antimalarial Drug Precursor Artemisinic Acid in Engineered Yeast. *Nature* **2006,** *440* (7086), 940-943.

6. Kirk, O.; Borchert, T. V.; Fuglsang, C. C., Industrial Enzyme Applications. *Current Opinion in Biotechnology* **2002,** *13* (4), 345-351.

7. Janssen, D. B.; Dinkla, I. J. T.; Poelarends, G. J.; Terpstra, P., Bacterial Degradation of Xenobiotic Compounds: Evolution and Distribution of Novel Enzyme Activities. *Environmental Microbiology* **2005,** *7* (12), 1868-1882.

8. Rothlisberger, D.; Khersonsky, O.; Wollacott, A. M.; Jiang, L.; DeChancie, J.; Betker, J.; Gallaher, J. L.; Althoff, E. A.; Zanghellini, A.; Dym, O.; Albeck, S.; Houk, K. N.; Tawfik, D. S.; Baker, D., Kemp Elimination Catalysts by Computational Enzyme Design. *Nature* **2008,** *453* (7192), 190-5.

9. Jiang, L.; Althoff, E. A.; Clemente, F. R.; Doyle, L.; Rothlisberger, D.; Zanghellini, A.; Gallaher, J. L.; Betker, J. L.; Tanaka, F.; Barbas, C. F.; Hilvert, D.; Houk, K. N.; Stoddard, B. L.; Baker, D., De Novo Computational Design of Retro-Aldol Enzymes. *Science* **2008,** *319* (5868), 1387-1391.

10. Siegel, J. B.; Zanghellini, A.; Lovick, H. M.; Kiss, G.; Lambert, A. R.; Clair, J. L. S.; Gallaher, J. L.; Hilvert, D.; Gelb, M. H.; Stoddard, B. L.; Houk, K. N.; Michael, F. E.; Baker, D., Computational Design of an Enzyme Catalyst for a Stereoselective Bimolecular Diels-Alder Reaction. *Science* **2010,** *329* (5989), 309-313.

11. Eiben, C. B.; Siegel, J. B.; Bale, J. B.; Cooper, S.; Khatib, F.; Shen, B. W.; Players, F.; Stoddard, B. L.; Popovic, Z.; Baker, D., Increased Diels-Alderase Activity through Backbone Remodeling Guided by Foldit Players. *Nat. Biotechnol.* **2012,** *30* (2), 190-192.

12. Preiswerk, N.; Beck, T.; Schulz, J. D.; Milovnik, P.; Mayer, C.; Siegel, J. B.; Baker, D.; Hilvert, D., Impact of Scaffold Rigidity on the Design and Evolution of an Artificial Diels-Alderase. *Proceedings of the National Academy of Sciences of the United States of America* **2014,** *111* (22), 8013-8018.

13. Pollak, E.; Talkner, P., Reaction Rate Theory: What It Was, Where Is It Today, and Where Is It Going? *Chaos* **2005,** *15* (2), 26116.

14. Arrhenius, S., Ueber Die Reaktionsgeschwindigekeit Bei Der Inversion Von Rohrzucker Durch Säuren. *Zeitschrift Fur Physikalische Chemie* **1889,** *4*, 226-248.

15. van't Hoff, J. H., *Etudes De Dynamiques Chimiques*. F. Muller and Co.: Amsterdam, 1884.

16. Pelzer, H.; Wigner, E., The Speed Constansts of the Exchange Reactions. *Z. Phys. Chem. B-Chem. Elem. Aufbau. Mater.* **1932,** *15* (6), 445-471.

17. Eyring, H., The Theory of Absolute Reaction Rates. *T Faraday Soc* **1938,** *34* (0), 41-48.

18. Wigner, E., The Transition State Method. *T Faraday Soc* **1938,** *34* (0), 29-41.

19. Eyring, H., The Activated Complex in Chemical Reactions. *The Journal of Chemical Physics* **1935,** *3* (2), 107-115.

20. Callender, R.; Dyer, R. B., The Dynamical Nature of Enzymatic Catalysis. *Accounts Chem Res* **2014**.

21. Pauling, L., Nature of Forces between Large Molecules of Biological Interest. *Nature* **1948,** *161* (4097), 707-709.

22. Kiss, G.; Çelebi-Ölçüm, N.; Moretti, R.; Baker, D.; Houk, K. N., Computational Enzyme Design. *Angewandte Chemie International Edition* **2013,** *52* (22), 5700-5725.

23. Hilvert, D., Design of Protein Catalysts. *Annual Review of Biochemistry* **2013,** *82* (1), 447-470.

24. Hilvert, D., Critical Analysis of Antibody Catalysis. *Annual Review of Biochemistry* **2000,** *69* (1), 751-793.

25. Schramm, V. L., Enzymatic Transition States, Transition-State Analogs, Dynamics, Thermodynamics, and Lifetimes. *Annual Review of Biochemistry* **2011,** *80* (1), 703-732.

26. Jencks, W. P., Binding Energy, Specificity, and Enzymic Catalysis: The Circe Effect. *Adv Enzymol Relat Areas Mol Biol* **1975,** *43*, 219-410.

27. Burgner, J. W.; Ray, W. J., On the Origin of the Lactate-Dehydrogenase Induced Rate Effect. *Biochemistry* **1984,** *23* (16), 3636-3648.

28. Frauenfelder, H.; Sligar, S. G.; Wolynes, P. G., The Energy Landscapes and Motions of Proteins. *Science* **1991,** *254* (5038), 1598-603.

29. Min, W.; Xie, X. S.; Bagchi, B., Two-Dimensional Reaction Free Energy Surfaces of Catalytic Reaction: Effects of Protein Conformational Dynamics on Enzyme Catalysis†. *The Journal of Physical Chemistry B* **2008,** *112* (2), 454-466.

30. Klinman, J. P.; Kohen, A., Hydrogen Tunneling Links Protein Dynamics to Enzyme Catalysis. *Annual Review of Biochemistry* **2013,** *82* (1), 471-496.

31. Schramm, V. L., Transition States and Transition State Analogue Interactions with Enzymes. *Acc Chem Res* **2015,** *48* (4), 1032-9.

32. Klinman, J. P., An Integrated Model for Enzyme Catalysis Emerges from Studies of Hydrogen Tunneling. *Chem. Phys. Lett.* **2009,** *471* (4-6), 179-193.

33. Min, W.; English, B. P.; Luo, G.; Cherayil, B. J.; Kou, S. C.; Xie, X. S., Fluctuating Enzymes: Lessons from Single-Molecule Studies. *Accounts Chem Res* **2005,** *38* (12), 923-931.

34. English, B. P.; Min, W.; van Oijen, A. M.; Lee, K. T.; Luo, G.; Sun, H.; Cherayil, B. J.; Kou, S. C.; Xie, X. S., Ever-Fluctuating Single Enzyme Molecules: Michaelis-Menten Equation Revisited. *Nat Chem Biol* **2006,** *2* (2), 87-94.

35. Nelson, D. L.; Cox, M. M., Protein Function. In *Lehninger Principles of Biochemistry*, W.H. Freeman and Company: New York, 2008; p 153.

36. Tsai, S.; Klinman, J. P., Probes of Hydrogen Tunneling with Horse Liver Alcohol Dehydrogenase at Subzero Temperatures. *Biochemistry* **2001,** *40* (7), 2303-11.

37. Heyes, D. J.; Sakuma, M.; de Visser, S. P.; Scrutton, N. S., Nuclear Quantum Tunneling in the Light-Activated Enzyme Protochlorophyllide Oxidoreductase. *J Biol Chem* **2009,** *284* (6), 3762-7.

38. Oliva, B.; Bates, P. A.; Querol, E.; Aviles, F. X.; Sternberg, M. J., An Automated Classification of the Structure of Protein Loops. *J Mol Biol* **1997,** *266* (4), 814-30.

39. Olson, M. A.; Feig, M.; Brooks, C. L., Prediction of Protein Loop Conformations Using Multiscale Modeling Methods with Physical Energy Scoring Functions. *Journal of Computational Chemistry* **2008,** *29* (5), 820-831.

40. Skliros, A.; Jernigan, R. L.; Kloczkowski, A., Models to Approximate the Motions of Protein Loops. *Journal of Chemical Theory and Computation* **2010,** *6* (10), 3249-3258.

41. Skliros, A.; Zimmermann, M. T.; Chakraborty, D.; Saraswathi, S.; Katebi, A. R.; Leelananda, S. P.; Kloczkowski, A.; Jernigan, R. L., The Importance of Slow Motions for Protein Functional Loops. *Physical Biology* **2012,** *9* (1).

42. Kinetics. In *Biophysical Chemistry*, Cooper, A., Ed. The Royal Society of Chemistry: 2004; Vol. 16, pp 123-142.

43. Beitz, J. V.; Flynn, G. W.; Turner, D. H.; Sutin, N., Stimulated Raman Effect. A New Source of Laser Temperature-Jump Heating. *Journal of the American Chemical Society* **1970,** *92* (13), 4130-4132.

44. Schade, M.; Moretto, A.; Donaldson, P. M.; Toniolo, C.; Hamm, P., Vibrational Energy Transport through a Capping Layer of Appropriately Designed Peptide Helices over Gold Nanoparticles. *Nano Lett* **2010,** *10* (8), 3057-61.

45. Li, G. F.; Magana, D.; Dyer, R. B., Anisotropic Energy Flow and Allosteric Ligand Binding in Albumin. *Nat. Commun.* **2014,** *5*, 7.

46. Iu, K. K.; Kuczynski, J.; Fuerniss, S. J.; Thomas, J. K., Laser Flash Photolysis of Arylsulfonium Salts: Studies of Photoproduced Proton Kinetics and Mechanism in Polar Solvents by a Ph-Jump Method. *Journal of the American Chemical Society* **1992,** *114* (12), 4871-4878.

47. Gutman, M.; Nachliel, E., Time-Resolved Dynamics of Proton Transfer in Proteinous Systems. *Annu Rev Phys Chem* **1997,** *48*, 329-56.

48. Gutman, M.; Huppert, D.; Pines, E., The Ph Jump: A Rapid Modulation of Ph of Aqueous Solutions by a Laser Pulse. *Journal of the American Chemical Society* **1981,** *103* (13), 3709-3713.

49. Dantzig, J. A.; Higuchi, H.; Goldman, Y. E., Studies of Molecular Motors Using Caged Compounds. In *Methods in Enzymology*, Gerard, M., Ed. Academic Press: 1998; Vol. Volume 291, pp 307-348.

50. Alpert, B.; Banerjee, R.; Lindqvist, L., The Kinetics of Conformational Changes in Hemoglobin, Studied by Laser Photolysis. *Proc Natl Acad Sci U S A* **1974,** *71* (2), 558-62.

51. Greene, B. I.; Hochstrasser, R. M.; Weisman, R. B.; Eaton, W. A., Spectroscopic Studies of Oxy- and Carbonmonoxyhemoglobin after Pulsed Optical Excitation. *Proc Natl Acad Sci U S A* **1978,** *75* (11), 5255-9.

52. Woodruff, W. H.; Einarsdottir, O.; Dyer, R. B.; Bagley, K. A.; Palmer, G.; Atherton, S. J.; Goldbeck, R. A.; Dawes, T. D.; Kliger, D. S., Nature and Functional Implications of the Cytochrome A3 Transients after Photodissociation of Co-Cytochrome Oxidase. *Proc Natl Acad Sci U S A* **1991,** *88* (6), 2588-92.

53. Barry, B. A.; Cooper, I. B.; De Riso, A.; Brewer, S. H.; Vu, D. M.; Dyer, R. B., Time-Resolved Vibrational Spectroscopy Detects Protein-Based Intermediates in the Photosynthetic Oxygen-Evolving Cycle. *Proceedings of the National Academy of Sciences of the United States of America* **2006,** *103* (19), 7288-7291.

54. KinTek Corporation USA New Sf-300x Stopped Flow. http://www.kintek-corp.com/products/sf300X.php (accessed May 13, 2015).

55. Kintek Corporation USA Kintek Corporation Rqf-3 Rapid Quench-Flow Instrument. http://www.kintek-corp.com/products/rqf3.php (accessed May 13, 2015).

56. Applied Photophysics Ltd. Stopped-Flow Spectroscopy: Performance Information. http://www.photophysics.com/tutorials/stopped-flow-spectrometry/sx20-performance-0 (accessed May 13, 2015).

57. Abonnenc, M.; Josserand, J.; Girault, H. H., Sandwich Mixer-Reactor: Influence of the Diffusion Coefficient and Flow Rate Ratios. *Lab on a Chip* **2009,** *9* (3), 440-448.

58. Gambin, Y.; Simonnet, C.; VanDelinder, V.; Deniz, A.; Groisman, A., Ultrafast Microfluidic Mixer with Three-Dimensional Flow Focusing for Studies of Biochemical Kinetics. *Lab on a Chip* **2010,** *10* (5), 598-609.

59. Hamadani, K. M.; Weiss, S., Nonequilibrium Single Molecule Protein Folding in a Coaxial Mixer. *Biophys J* **2008,** *95* (1), 352-365.

60. Hertzog, D. E.; Ivorra, B.; Mohammadi, B.; Bakajin, O.; Santiago, J. G., Optimization of a Microfluidic Mixer for Studying Protein Folding Kinetics. *Analytical Chemistry* **2006,** *78* (13), 4299-4306.

61. Pabit, S. A.; Hagen, S. J., Laminar-Flow Fluid Mixer for Fast Fluorescence Kinetics Studies. *Biophys J* **2002,** *83* (5), 2872-2878.

62. Park, H. Y.; Qiu, X. Y.; Rhoades, E.; Korlach, J.; Kwok, L. W.; Zipfel, W. R.; Webb, W. W.; Pollack, L., Achieving Uniform Mixing in a Microfluidic Device: Hydrodynamic Focusing Prior to Mixing. *Analytical Chemistry* **2006,** *78* (13), 4465-4473.

63. Toepke, M. W.; Brewer, S. H.; Vu, D. M.; Rector, K. D.; Morgan, J. E.; Gennis, R. B.; Kenis, P. J. A.; Dyer, R. B., Microfluidic Flow-Flash: Method for Investigating Protein Dynamics. *Analytical Chemistry* **2007,** *79* (1), 122-128.

64. Yao, S.; Bakajin, O., Improvements in Mixing Time and Mixing Uniformity in Devices Designed for Studies of Protein Folding Kinetics. *Analytical Chemistry* **2007,** *79* (15), 5753-5759.

65. Hertzog, D. E.; Michalet, X.; Jager, M.; Kong, X. X.; Santiago, J. G.; Weiss, S.; Bakajin, O., Femtomole Mixer for Microsecond Kinetic Studies of Protein Folding. *Analytical Chemistry* **2004,** *76* (24), 7169-7178.

66. Knight, J. B.; Vishwanath, A.; Brody, J. P.; Austin, R. H., Hydrodynamic Focusing on a Silicon Chip: Mixing Nanoliters in Microseconds. *Phys Rev Lett* **1998,** *80* (17), 3863-3866.

67. Huang, S.-B.; Zhao, Y.; Chen, D.; Lee, H.-C.; Luo, Y.; Chiu, T.-K.; Wang, J.; Chen, J.; Wu, M.-H., A Clogging-Free Microfluidic Platform with an Incorporated Pneumatically Driven Membrane-Based Active Valve Enabling Specific Membrane Capacitance and Cytoplasm Conductivity Characterization of Single Cells. *Sensors and Actuators B: Chemical* **2014,** *190* (0), 928-936.

68. Kohnle, J.; Waibel, G.; Cernosa, R.; Storz, M.; Ernst, H.; Sandmaier, H.; Strobelt, T.; Zengerle, R. In *A Unique Solution for Preventing Clogging of Flow Channels by Gas Bubbles*, Micro Electro Mechanical Systems, 2002. The Fifteenth IEEE International Conference on, 24-24 Jan. 2002; 2002; pp 77-80.

69. Wyss, H. M.; Blair, D. L.; Morris, J. F.; Stone, H. A.; Weitz, D. A., Mechanism for Clogging of Microchannels. *Physical Review E* **2006,** *74* (6), 061402.

70. Anwar, A.; Mazzitelli, S.; Nastruzzi, C. A Simple Trick to Open up Clogged Microfluidic Chip. http://blogs.rsc.org/chipsandtips/2013/07/18/a-simple-trick-to-open-up-clogged-microfluidic-chip/ (accessed May 13, 2015).

71. Barth, A., Infrared Spectroscopy of Proteins. *Biochimica et Biophysica Acta (BBA) - Bioenergetics* **2007,** *1767* (9), 1073-1101.

72. Spectroscopy. In *Biophysical Chemistry*, Cooper, A., Ed. The Royal Society of Chemistry: 2004; Vol. 16, pp 21-69.

73. Cai, D. K.; Neyer, A.; Kuckuk, R.; Heise, H. M., Optical Absorption in Transparent Pdms Materials Applied for Multimode Waveguides Fabrication. *Optical Materials* **2008,** *30* (7), 1157-1161.

74. Barich, M. V.; Krummel, A. T., Polymeric Infrared Compatible Microfluidic Devices for Spectrochemical Analysis. *Analytical Chemistry* **2013,** *85* (21), 10000-10003.

75. Bernasconi, C. F., *Relaxation Kinetics*. Academic Press: New York, 1976; p xi, 288 p.

76. Davis, C. M.; Xiao, S.; Raleigh, D. P.; Dyer, R. B., Raising the Speed Limit for Beta-Hairpin Formation. *J Am Chem Soc* **2012,** *134* (35), 14476-82.

77. Khajehpour, M.; Wu, L.; Liu, S. J.; Zhadin, N.; Zhang, Z. Y.; Callender, R., Loop Dynamics and Ligand Binding Kinetics in the Reaction Catalyzed by the Yersinia Protein Tyrosine Phosphatase. *Biochemistry* **2007,** *46* (14), 4370-4378.

78. Czerlinski, G.; Eigen, M., Eine Temperatursprungmethode Zur Untersuchung Chemischer Relaxation. *Z Elektrochem* **1959,** *63* (6), 652-661.

79. Caldin, E. F.; Crooks, J. E., A Microwave Temperature-Jump Apparatus for Study of Fast Reactions in Solution. *Journal of Scientific Instruments* **1967,** *44* (6), 449-&.

80. Max, J.-J.; Chapados, C., Isotope Effects in Liquid Water by Infrared Spectroscopy. Iii. H2o and D2o Spectra from 6000to0cm−1. *The Journal of Chemical Physics* **2009,** *131* (18), 184505.

81. Venyaminov, S. Y.; Prendergast, F. G., Water (H2o and D2o) Molar Absorptivity in the 1000–4000 Cm−1range and Quantitative Infrared Spectroscopy of Aqueous Solutions. *Analytical Biochemistry* **1997,** *248* (2), 234-245.

82. Hoffmann, H.; Yeager, E.; Stuehr, J., Laser Temperature-Jump Apparatus for Relaxation Studies in Electrolytic Solutions. *Rev Sci Instrum* **1968,** *39* (5), 649-653.

83. Turner, D. H.; Flynn, G. W.; Sutin, N.; Beitz, J. V., Laser Raman Temperature-Jump Study of the Kinetics of the Triiodide Equilibrium. Relaxation Times in the 10-8 - 10-7 Second Range. *Journal of the American Chemical Society* **1972,** *94* (5), 1554-1559.

84. Holzwarth, J. F.; Schmidt, A.; Wolff, H.; Volk, R., Nanosecond Temperature-Jump Technique with an Iodine Laser. *J Phys Chem-Us* **1977,** *81* (24), 2300-2301.

85. Smith, J. J.; McCray, J. A.; Hibberd, M. G.; Goldman, Y. E., Holmium Laser Temperature-Jump Apparatus for Kinetic Studies of Muscle Contraction. *Rev Sci Instrum* **1989,** *60* (2), 231-236.

86. Callender, R.; Dyer, R. B., Advances in Time-Resolved Approaches to Characterize the Dynamical Nature of Enzymatic Catalysis. *Chemical Reviews* **2006,** *106* (8), 3031-3042.

87. Dyer, R. B.; Brauns, E. B., Laser-Induced Temperature Jump Infrared Measurements of Rna Folding. In *Methods in Enzymology, Vol 469: Biophysical, Chemical, and Functional Probes of Rna Structure, Interactions and Folding, Pt B*, Elsevier Academic Press Inc: San Diego, 2009; Vol. 469, pp 353-372.

88. Zhadin, N.; Gulotta, M.; Callender, R., Probing the Role of Dynamics in Hydride Transfer Catalyzed by Lactate Dehydrogenase. *Biophys J* **2008,** *95* (4), 1974-1984.

89. Desamero, R.; Rozovsky, S.; Zhadin, N.; McDermott, A.; Callender, R., Active Site Loop Motion in Triosephosphate Isomerase: T-Jump Relaxation Spectroscopy of Thermal Activation. *Biochemistry* **2003,** *42* (10), 2941-2951.

90. Ghanem, M.; Zhadin, N.; Callender, R.; Schramm, V. L., Loop-Tryptophan Human Purine Nucleoside Phosphorylase Reveals Submillisecond Protein Dynamics. *Biochemistry* **2009,** *48* (16), 3658-3668.

91. Huang, C.-Y.; Getahun, Z.; Zhu, Y.; Klemke, J. W.; DeGrado, W. F.; Gai, F., Helix Formation Via Conformation Diffusion Search. *Proceedings of the National Academy of Sciences* **2002,** *99* (5), 2788-2793.

92. Kwiatkowski, J.; Jabczynski, J. K.; Zendzian, W.; Gorajek, L.; Kaskow, M., High Repetition Rate, Q-Switched Ho:Yag Laser Resonantly Pumped by a 20 w Linearly Polarized Tm: Fiber Laser. *Appl. Phys. B* **2014,** *114* (3), 395-399.

93. Burke, K. S.; Parul, D.; Reddish, M. J.; Dyer, R. B., A Simple Three-Dimensional-Focusing, Continuous-Flow Mixer for the Study of Fast Protein Dynamics. *Lab Chip* **2013,** *13* (15), 2912-21.

94. Tsien, R. Y.; Ernst, L.; Waggoner, A., Fluorophores for Confocal Microscopy: Photphysics and Photochemistry. In *Handbook of Biological Confocal Microscopy,* 3rd ed.; Pawley, J. B., Ed. Springer Science+Business Media, LLC: New York, 2006; pp pgs. 338-351.

95. Kasha, M., Collisional Perturbation of Spin-Orbital Coupling and the Mechanism of Fluorescence Quenching. A Visual Demonstration of the Perturbation. *The Journal of Chemical Physics* **1952,** *20* (1), 71-74.

96. Cukierman, S., Et Tu, Grotthuss! And Other Unfinished Stories. *Biochimica et Biophysica Acta (BBA) - Bioenergetics* **2006,** *1757* (8), 876-885.

97. Evans, S. V.; Brayer, G. D., Horse Heart Metmyoglobin - a 2.8-a Resolution 3-Dimensional Structure Determination. *J Biol Chem* **1988,** *263* (9), 4263-4268.

98. Callender, R. H.; Dyer, R. B.; Gilmanshin, R.; Woodruff, W. H., Fast Events in Protein Folding: The Time Evolution of Primary Processes. *Annu. Rev. Phys. Chem.* **1998,** *49*, 173-202.

99. Uzawa, T.; Akiyama, S.; Kimura, T.; Takahashi, S.; Ishimori, K.; Morishima, I.; Fujisawa, T., Collapse and Search Dynamics of Apomyoglobin Folding Revealed by Submillisecond Observations of Alpha-Helical Content and Compactness. *Proceedings of the National Academy of Sciences of the United States of America* **2004,** *101* (5), 1171-1176.

100. Meinhold, D. W.; Wright, P. E., Measurement of Protein Unfolding/Refolding Kinetics and Structural Characterization of Hidden Intermediates by Nmr Relaxation Dispersion. *Proceedings of the National Academy of Sciences of the United States of America* **2011,** *108* (22), 9078-9083.

101. Weisbuch, S.; Gerard, F.; Pasdeloup, M.; Cappadoro, J.; Dupont, Y.; Jamin, M., Cooperative Sub-Millisecond Folding Kinetics of Apomyoglobin Ph 4 Intermediate. *Biochemistry* **2005,** *44* (18), 7013-7023.

102. Gilmanshin, R.; Dyer, R. B.; Callender, R. H., Structural Heterogeneity of the Various Forms of Apomyoglobin: Implications for Protein Folding. *Protein Sci* **1997,** *6* (10), 2134-2142.

103. Gilmanshin, R.; Callender, R. H.; Dyer, R. B., The Core of Apomyoglobin E-Form Folds at the Diffusion Limit. *Nat Struct Biol* **1998,** *5* (5), 363-365.

104. Gulotta, M.; Gilmanshin, R.; Buscher, T. C.; Callender, R. H.; Dyer, R. B., Core Formation in Apomyoglobin: Probing the Upper Reaches of the Folding Energy Landscape. *Biochemistry* **2001,** *40* (17), 5137-5143.

105. Xu, M.; Beresneva, O.; Rosario, R.; Roder, H., Microsecond Folding Dynamics of Apomyoglobin at Acidic Ph. *J Phys Chem B* **2012,** *116* (23), 7014-7025.

106. Yang, A. S.; Honig, B., Structural Origins of Ph and Ionic-Strength Effects on Protein Stability - Acid Denaturation of Sperm Whale Apomyoglobin. *J Mol Biol* **1994,** *237* (5), 602-614.

107. Stryer, L., The Interaction of a Naphthalene Dye with Apomyoglobin and Apohemoglobin. A Fluorescent Probe of Non-Polar Binding Sites. *J Mol Biol* **1965,** *13* (2), 482-95.

108. Adams, P. A., Kinetics of Recombination Reaction between Apomyoglobin and Alkaline Hematin. *Biochem J* **1977,** *163* (1), 153-158.

109. Weber, G.; Young, L. B., Fragmentation of Bovine Serum Albumin by Pepsin .1. Origin of Acid Expansion of Albumin Molecule. *J Biol Chem* **1964,** *239* (5), 1415-&.

110. Jamin, M.; Baldwin, R. L., Two Forms of the Ph 4 Folding Intermediate of Apomyoglobin. *J Mol Biol* **1998,** *276* (2), 491-504.

111. Uzawa, T.; Nishimura, C.; Akiyama, S.; Ishimori, K.; Takahashi, S.; Dyson, H. J.; Wright, P. E., Hierarchical Folding Mechanism of Apomyoglobin Revealed by Ultra-Fast H/D Exchange Coupled with 2d Nmr. *Proceedings of the National Academy of Sciences of the United States of America* **2008,** *105* (37), 13859-13864.

112. Jennings, P. A.; Wright, P. E., Formation of a Molten Globule Intermediate Early in the Kinetic Folding Pathway of Apomyoglobin. *Science* **1993,** *262* (5135), 892-896.

113. Jamin, M.; Yeh, S. R.; Rousseau, D. L.; Baldwin, R. L., Submillisecond Unfolding Kinetics of Apomyoglobin and Its Ph 4 Intermediate. *J Mol Biol* **1999,** *292* (3), 731-740.

114. Haruta, N.; Kitagawa, T., Time-Resolved Uv Resonance Raman Investigation of Protein Folding Using a Rapid Mixer: Characterization of Kinetic Folding Intermediates of Apomyoglobin. *Biochemistry* **2002,** *41* (21), 6595-6604.

115. Baryshnikova, E. N.; Melnik, B. S.; Semisotnov, G. V.; Bychkova, V. E., Investigation of Folding/Unfolding Kinetics of Apomyoglobin. *Mol Biol+* **2005,** *39* (6), 1008-1016.

116. Wang, C.; Ye, D.-K.; Wang, Y.-Y.; Lu, T.; Xia, X.-H., Insights into the "Free State" Enzyme Reaction Kinetics in Nanoconfinement. *Lab on a Chip* **2013,** *13* (8), 1546-1553.

117. Drent, M.; Cobben, N. A.; Henderson, R. F.; Wouters, E. F.; van Dieijen-Visser, M., Usefulness of Lactate Dehydrogenase and Its Isoenzymes as Indicators of Lung Damage or Inflammation. *The European respiratory journal* **1996,** *9* (8), 1736-42.

118. Ogata, M.; Arihara, K.; Yagi, T., D-Lactate Dehydrogenase of Desulfovibrio Vulgaris. *J Biochem* **1981,** *89* (5), 1423-31.

119. Clausen, J., Lactate Dehydrogenase Isoenzymes of Sperm Cells and Tests. *Biochem J* **1969,** *111* (2), 207-18.

120. Nagel, Z. D.; Klinman, J. P., Tunneling and Dynamics in Enzymatic Hydride Transfer. *Chemical Reviews* **2006,** *106* (8), 3095-3118.

121. Deng, H.; Zheng, J.; Clarke, A.; Holbrook, J. J.; Callender, R.; Burgner, J. W., Source of Catalysis in the Lactate-Dehydrogenase System - Ground-State Interactions in the Enzyme-Substrate Complex. *Biochemistry* **1994,** *33* (8), 2297-2305.

122. Clarke, A. R.; Wigley, D. B.; Chia, W. N.; Barstow, D.; Atkinson, T.; Holbrook, J. J., Site-Directed Mutagenesis Reveals Role of Mobile Arginine Residue in Lactate-Dehydrogenase Catalysis. *Nature* **1986,** *324* (6098), 699-702.

123. Waldman, A. D.; Hart, K. W.; Clarke, A. R.; Wigley, D. B.; Barstow, D. A.; Atkinson, T.; Chia, W. N.; Holbrook, J. J., The Use of Genetically Engineered Tryptophan to Identify the Movement of a Domain of B. Stearothermophilus Lactate Dehydrogenase with the Process Which Limits the Steady-State Turnover of the Enzyme. *Biochem Biophys Res Commun* **1988,** *150* (2), 752-9.

124. McClendon, S.; Zhadin, N.; Callender, R., The Approach to the Michaelis Complex in Lactate Dehydrogenase: The Substrate Binding Pathway. *Biophys J* **2005,** *89* (3), 2024-2032.

125. Deng, H.; Brewer, S.; Vu, D. M.; Clinch, K.; Callender, R.; Dyer, R. B., On the Pathway of Forming Enzymatically Productive Ligand-Protein Complexes in Lactate Dehydrogenase. *Biophys J* **2008,** *95* (2), 804-813.

126. Reddish, M. J.; Peng, H.-L.; Deng, H.; Panwar, K. S.; Callender, R.; Dyer, R. B., Direct Evidence of Catalytic Heterogeneity in Lactate Dehydrogenase by Temperature Jump Infrared Spectroscopy. *The Journal of Physical Chemistry B* **2014,** *118* (37), 10854-10862.

127. Gremlich, H.-U.; Yan, B., *Infrared and Raman Spectroscopy of Biological Materials*. M. Dekker: New York, 2001; p ix, 581 p.

128. Gregoriou, V. G.; Braiman, M. S., *Vibrational Spectroscopy of Biological and Polymeric Materials*. CRC/Taylor & Francis: Boca Raton, FL, 2006; p 430 p.

129. Siebert, F.; Hildebrandt, P. W., *Vibrational Spectroscopy in Life Science*. Wiley-VCH: Weinheim ; Chichester, 2008; p x, 310 p.

130. Lasch, P.; Kneipp, J., Biomedical Vibrational Spectroscopy. John Wiley & Sons: Hoboken, N.J., 2008; p. 1 online resource.

131. Nagarajan, S.; Taskent-Sezgin, H.; Parul, D.; Carrico, I.; Raleigh, D. P.; Dyer, R. B., Differential Ordering of the Protein Backbone and Side Chains During Protein Folding Revealed by Site-Specific Recombinant Infrared Probes. *J Am Chem Soc* **2011,** *133* (50), 20335-40.

132. Arrondo, J. L. R.; Blanco, F. J.; Serrano, L.; Goni, F. M., Infrared Evidence of a Beta-Hairpin Peptide Structure in Solution. *Febs Lett* **1996,** *384* (1), 35-37.

133. Susi, H.; Byler, D. M., Resolution-Enhanced Fourier Transform Infrared Spectroscopy of Enzymes. *Methods Enzymol* **1986,** *130*, 290-311.

134. Yang, W. J.; Griffiths, P. R.; Byler, D. M.; Susi, H., Protein Conformation by Infrared-Spectroscopy - Resolution Enhancement by Fourier Self-Deconvolution. *Appl Spectrosc* **1985,** *39* (2), 282-287.

135. Marley, J.; Lu, M.; Bracken, C., A Method for Efficient Isotopic Labeling of Recombinant Proteins. *J Biomol Nmr* **2001,** *20* (1), 71-5.

136. Callender, R.; Deng, H., Nonresonance Raman Difference Spectroscopy: A General Probe of Protein Structure, Ligand Binding, Enzymatic Catalysis, and the Structures of Other Biomacromolecules. *Annu Rev Biophys Biomol Struct* **1994,** *23*, 215-45.

137. Peng, H.-L.; Deng, H.; Dyer, R. B.; Callender, R., The Energy Landscape of the Michaelis Complex of Lactate Dehydrogenase: Relationship to Catalytic Mechanism. *Biochemistry* **2014**.

138. Zhadin, N.; Callender, R., Effect of Osmolytes on Protein Dynamics in the Lactate Dehydrogenase-Catalyzed Reaction. *Biochemistry* **2011,** *50* (10), 1582-1589.

139. Pineda, J.; Antoniou, D.; Schwartz, S. D., Slow Conformational Motions That Favor Sub-Picosecond Motions Important for Catalysis. *J Phys Chem B* **2010,** *114* (48), 15985-15990.

140. Davis, C. M.; Xiao, S. F.; Raeigh, D. P.; Dyer, R. B., Raising the Speed Limit for Beta-Hairpin Formation. *Journal of the American Chemical Society* **2012,** *134* (35), 14476-14482.

141. Clarke, A. R.; Wilks, H. M.; Barstow, D. A.; Atkinson, T.; Chia, W. N.; Holbrook, J. J., An Investigation of the Contribution Made by the Carboxylate Group of an Active-Site Histidine Aspartate Couple to Binding and Catalysis in Lactate-Dehydrogenase. *Biochemistry* **1988,** *27* (5), 1617-1622.

142. Nie, B.; Deng, H.; Desamero, R.; Callender, R., Large Scale Dynamics of the Michaelis Complex in Bacillus Stearothermophilus Lactate Dehydrogenase Revealed by a Single-Tryptophan Mutant Study. *Biochemistry* **2013,** *52* (11), 1886-92.

143. Parker, D. M.; Jeckel, D.; Holbrook, J. J., Slow Structural Changes Shown by the 3-Nitrotyrosine-237 Residue in Pig Heart [Tyr(3no2)237] Lactate Dehydrogenase. *Biochem J* **1982,** *201* (3), 465-471.

144. Clarke, A. R.; Waldman, A. D. B.; Hart, K. W.; Holbrook, J. J., The Rates of Defined Changes in Protein Structure During the Catalytic Cycle of Lactate Dehydrogenase. *Biochim Biophys Acta* **1985,** *829*, 397-407.

145. Eigen, M.; DeMaeyer, L., In *Technique of Organic Chemistry*, Friess, S. L.; Lewis, E. S.; Weissberger, A., Eds. Wiley (Interscience): New York, 1963; Vol. VIII, p 895.

146. Eigen, M.; Demaeyer, L., In *Techniques of Chemistry*, Hammes, G. G., Ed. Wiley (Interscience): New York, 1973; Vol. VI, p 63.

147. Kustin, K.; Shear, D.; Kleitman, D., Theory of Relaxation Spectra; the Kinetics of Coupled Chemical Reactions. *J Theor Biol* **1965,** *9* (2), 186-212.

148. Hayman, H. J. G., Orthonormal Chemical Reactions and Chemical Relaxation .2. Reactions in Non-Ideal Solutions. *T Faraday Soc* **1970,** *66* (570), 1402-&.

149. Schwarz, G., Kinetic Analysis by Chemical Relaxation Methods. *Rev Mod Phys* **1968,** *40* (1), 206-&.

150. Clarke, A. R.; Waldman, A. D. B.; Hart, K. W.; Holbrook, J. J., The Rates of Defined Changes in Protein-Structure During the Catalytic Cycle of Lactate-Dehydrogenase. *Biochim Biophys Acta* **1985,** *829* (3), 397-407.

151. Dyer, R. B.; Woodruff, W. H., Vibrational Spectroscopy. In *Encyclopedia of Inorganic Chemistry*, John Wiley & Sons, Ltd: 2006.

152. Calder, G. V., The Time Evolution of Drugs in the Body. An Application of the Principles of Chemical Kinetics. *J Chem Educ* **1974,** *51* (1), 19.

153. Koshland, D. E., Application of a Theory of Enzyme Specificity to Protein Synthesis. *Proceedings of the National Academy of Sciences of the United States of America* **1958,** *44* (2), 98-104.

154. Hammes-Schiffer, S.; Benkovic, S. J., Relating Protein Motion to Catalysis. *Annual Review of Biochemistry* **2006,** *75*, 519-541.

155. Blakley, R., Eukaryotic Dihydrofolate Reductase. *Adv Enzymol Ramb* **1995,** *70,* 23-102.

156. Appleman, J. R.; Howell, E. E.; Kraut, J.; Blakley, R. L., Role of Aspartate 27 of Dihydrofolate Reductase from Escherichia Coli in Interconversion of Active and Inactive Enzyme Conformers and Binding of Nadph. *J Biol Chem* **1990,** *265* (10), 5579-84.

157. Appleman, J. R.; Howell, E. E.; Kraut, J.; Kuhl, M.; Blakley, R. L., Role of Aspartate-27 in the Binding of Methotrexate to Dihydrofolate-Reductase from Escherichia-Coli. *J Biol Chem* **1988,** *263* (19), 9187-9198.

158. Dunn, S. M. J.; Lanigan, T. M.; Howell, E. E., Dihydrofolate Reductase from Escherichia Coli: Probing the Role of Aspartate-27 and Phenylalanine-137 in Enzyme Conformation and the Binding of Nadph. *Biochemistry* **1990,** *29* (37), 8569-8576.

159. Fierke, C. A.; Johnson, K. A.; Benkovic, S. J., Construction and Evaluation of the Kinetic Scheme Associated with Dihydrofolate-Reductase from Escherichia-Coli. *Biochemistry* **1987,** *26* (13), 4085-4092.

160. Huennekens, F. M., In Search of Dihydrofolate Reductase. *Protein Sci* **1996,** *5* (6), 1201-1208.

161. Schnell, J. R.; Dyson, H. J.; Wright, P. E., Structure, Dynamics, and Catalytic Function of Dihydrofolate Reductase. *Annu. Rev. Biophys. Biomolec. Struct.* **2004,** *33,* 119-140.

162. Sawaya, M. R.; Kraut, J., Loop and Subdomain Movements in the Mechanism of Escherichia Coli Dihydrofolate Reductase: Crystallographic Evidence. *Biochemistry* **1997,** *36* (3), 586-603.

163. Swanwick, R. S.; Shrimpton, P. J.; Allemann, R. K., Pivotal Role of Gly 121 in Dihydrofolate Reductase from Escherichia Coli: The Altered Structure of a Mutant Enzyme May Form the Basis of Its Diminished Catalytic Performance. *Biochemistry* **2004,** *43* (14), 4119-4127.

164. Rajagopalan, P. T. R.; Lutz, S.; Benkovic, S. J., Coupling Interactions of Distal Residues Enhance Dihydrofolate Reductase Catalysis: Mutational Effects on Hydride Transfer Rates†. *Biochemistry* **2002,** *41* (42), 12618-12628.

165. Singh, P.; Sen, A.; Francis, K.; Kohen, A., Extension and Limits of the Network of Coupled Motions Correlated to Hydride Transfer in Dihydrofolate Reductase. *Journal of the American Chemical Society* **2014,** *136* (6), 2575-2582.

166. Ishima, R.; Torchia, D. A., Protein Dynamics from Nmr. *Nat Struct Biol* **2000,** *7* (9), 740-3.

167. Rajagopalan, P. T.; Benkovic, S. J., Preorganization and Protein Dynamics in Enzyme Catalysis. *Chem Rec* **2002,** *2* (1), 24-36.

168. Oyeyemi, O. A.; Sours, K. M.; Lee, T.; Resing, K. A.; Ahn, N. G.; Klinman, J. P., Temperature Dependence of Protein Motions in a Thermophilic Dihydrofolate Reductase

and Its Relationship to Catalytic Efficiency. *Proceedings of the National Academy of Sciences of the United States of America* **2010,** *107* (22), 10074-10079.

169. Evans, R. M.; Behiry, E. M.; Tey, L. H.; Guo, J. N.; Loveridge, E. J.; Allemann, R. K., Catalysis by Dihydrofolate Reductase from the Psychropiezophile Moritella Profunda. *ChemBioChem* **2010,** *11* (14), 2010-2017.

170. Kohen, A.; Cannio, R.; Bartolucci, S.; Klinman, J. P., Enzyme Dynamics and Hydrogen Tunnelling in a Thermophilic Alcohol Dehydrogenase. *Nature* **1999,** *399* (6735), 496-499.

171. Miller, G. P.; Wahnon, D. C.; Benkovic, S. J., Interloop Contacts Modulate Ligand Cycling During Catalysis by Escherichia Coli Dihydrofolate Reductase. *Biochemistry* **2001,** *40* (4), 867-875.

172. Boehr, D. D.; McElheny, D.; Dyson, H. J.; Wright, P. E., The Dynamic Energy Landscape of Dihydrofolate Reductase Catalysis. *Science* **2006,** *313* (5793), 1638-1642.

173. Bystroff, C.; Kraut, J., Crystal Structure of Unliganded Escherichia Coli Dihydrofolate Reductase. Ligand-Induced Conformational Changes and Cooperativity in Binding. *Biochemistry* **1991,** *30* (8), 2227-2239.

174. Fan, Y.; Cembran, A.; Ma, S. H.; Gao, J. L., Connecting Protein Conformational Dynamics with Catalytic Function as Illustrated in Dihydrofolate Reductase. *Biochemistry* **2013,** *52* (12), 2036-2049.

175. Osborne, M. J.; Venkitakrishnan, R. P.; Dyson, H. J.; Wright, P. E., Diagnostic Chemical Shift Markers for Loop Conformation and Substrate and Cofactor Binding in Dihydrofolate Reductase Complexes. *Protein Science : A Publication of the Protein Society* **2003,** *12* (10), 2230-2238.

176. Grubbs, J.; Rahmanian, S.; DeLuca, A.; Padmashali, C.; Jackson, M.; Duff, M. R.; Howell, E. E., Thermodynamics and Solvent Effects on Substrate and Cofactor Binding in Escherichia Coli Chromosomal Dihydrofolate Reductase. *Biochemistry* **2011,** *50* (18), 3673-3685.

177. Gekko, K.; Yamagami, K.; Kunori, Y.; Ichihara, S.; Kodama, M.; Iwakura, M., Effects of Point Mutation in a Flexible Loop on the Stability and Enzymatic Function of Escherichia Coli Dihydrofolate Reductase. *J. Biochem.* **1993,** *113* (1), 74-80.

178. Sasso, S.; Protasevich, I.; Gilli, R.; Makarov, A.; Briand, C., Thermal-Denaturation of Bacterial and Bovine Dihydrofolate Reductases and Their Complexes with Nadph, Trimethoprim and Methotrexate. *J. Biomol. Struct. Dyn.* **1995,** *12* (5), 1023-1032.

179. Davis, C. M.; Dyer, R. B., Ww Domain Folding Complexity Revealed by Infrared Spectroscopy. *Biochemistry* **2014,** *53* (34), 5476-5484.

180. Cayley, P. J.; Dunn, S. M. J.; King, R. W., Kinetics of Substrate, Coenzyme, and Inhibitor Binding to Escherichia-Coli Dihydrofolate-Reductase. *Biochemistry* **1981,** *20* (4), 874-879.

181. Chen, S.; Fahmi, N. E.; Wang, L.; Bhattacharya, C.; Benkovic, S. J.; Hecht, S. M., Detection of Dihydrofolate Reductase Conformational Change by Fret Using Two Fluorescent Amino Acids. *Journal of the American Chemical Society* **2013,** *135* (35), 12924-12927.

182. Chen, S.; Wang, L.; Fahmi, N. E.; Benkovic, S. J.; Hecht, S. M., Two Pyrenylalanines in Dihydrofolate Reductase Form an Excimer Enabling the Study of

Protein Dynamics. *Journal of the American Chemical Society* **2012,** *134* (46), 18883-18885.

183. Liu, C. T.; Layfield, J. P.; Stewart, R. J.; French, J. B.; Hanoian, P.; Asbury, J. B.; Hammes-Schiffer, S.; Benkovic, S. J., Probing the Electrostatics of Active Site Microenvironments Along the Catalytic Cycle for Escherichia Coli Dihydrofolate Reductase. *Journal of the American Chemical Society* **2014,** *136* (29), 10349-10360.

184. Williams, J. W.; Morrison, J. F.; Duggleby, R. G., Methotrexate, a High-Affinity Pseudosubstrate of Dihydrofolate-Reductase. *Biochemistry* **1979,** *18* (12), 2567-2573.

185. Kise, D. P.; Magana, D.; Reddish, M. J.; Dyer, R. B., Submillisecond Mixing in a Continuous-Flow, Microfluidic Mixer Utilizing Mid-Infrared Hyperspectral Imaging Detection. *Lab on a Chip* **2014,** *14* (3), 584-591.

186. Bzowska, A.; Kulikowska, E.; Shugar, D., Purine Nucleoside Phosphorylases: Properties, Functions, and Clinical Aspects. *Pharmacology & Therapeutics* **2000,** *88* (3), 349-425.

187. Giblett, E. R.; Ammann, A. J.; Wara, D. W.; Sandman, R.; Diamond, L. K., Nucleoside-Phosphorylase Deficiency in a Child with Severely Defective T-Cell Immunity and Normal B-Cell Immunity. *Lancet* **1975,** *1* (7914), 1010-3.

188. Rich, K. C.; Arnold, W. J.; Palella, T.; Fox, I. H., Cellular Immune Deficiency with Autoimmune Hemolytic Anemia in Purine Nucleoside Phosphorylase Deficiency. *Am J Med* **1979,** *67* (1), 172-6.

189. Stoop, J. W.; Zegers, B. J.; Hendrickx, G. F.; van Heukelom, L. H.; Staal, G. E.; de Bree, P. K.; Wadman, S. K.; Ballieux, R. E., Purine Nucleoside Phosphorylase

Deficiency Associated with Selective Cellular Immunodeficiency. *N Engl J Med* **1977,** *296* (12), 651-5.

190. Pugmire, M. J.; Ealick, S. E., Structural Analyses Reveal Two Distinct Families of Nucleoside Phosphorylases. *Biochem J* **2002,** *361*, 1-25.

191. Morris, J., Philip E; Montgomery, J. A., Inhibitors of the Enzyme Purine Nucleoside Phosphorylase. *Expert Opinion on Therapeutic Patents* **1998,** *8* (3), 283-299.

192. Sircar, J. C.; Kostlan, C. R.; Gilbertsen, R. B.; Bennett, M. K.; Dong, M. K.; Cetenko, W. J., Inhibitors of Human Purine Nucleoside Phosphorylase. Synthesis of Pyrrolo[3,2-D]Pyrimidines, a New Class of Purine Nucleoside Phosphorylase Inhibitors as Potentially T-Cell Selective Immunosuppressive Agents. Description of 2,6-Diamino-3,5-Dihydro-7-(3-Thienylmethyl)-4h-Pyrrolo[3,2-D]Pyrimidin-4-One (Ci-972). *J Med Chem* **1992,** *35* (9), 1605-1609.

193. Bennett, L. L., Jr.; Allan, P. W.; Noker, P. E.; Rose, L. M.; Niwas, S.; Montgomery, J. A.; Erion, M. D., Purine Nucleoside Phosphorylase Inhibitors: Biochemical and Pharmacological Studies with 9-Benzyl-9-Deazaguanine and Related Compounds. *J Pharmacol Exp Ther* **1993,** *266* (2), 707-14.

194. Stoeckler, J. D.; Ealick, S. E.; Bugg, C. E.; Parks, R. E., Jr., Design of Purine Nucleoside Phosphorylase Inhibitors. *Fed Proc* **1986,** *45* (12), 2773-8.

195. Ealick, S. E.; Babu, Y. S.; Bugg, C. E.; Erion, M. D.; Guida, W. C.; Montgomery, J. A.; Secrist, J. A., Application of Crystallographic and Modeling Methods in the Design of Purine Nucleoside Phosphorylase Inhibitors. *Proceedings of the National Academy of Sciences of the United States of America* **1991,** *88* (24), 11540-11544.

196. Kicska, G. A.; Long, L.; Hörig, H.; Fairchild, C.; Tyler, P. C.; Furneaux, R. H.; Schramm, V. L.; Kaufman, H. L., Immucillin H, a Powerful Transition-State Analog Inhibitor of Purine Nucleoside Phosphorylase, Selectively Inhibits Human T Lymphocytes. *Proceedings of the National Academy of Sciences* **2001,** *98* (8), 4593-4598.

197. Ho, M. C.; Shi, W. X.; Rinaldo-Matthis, A.; Tyler, P. C.; Evans, G. B.; Clinch, K.; Almo, S. C.; Schramm, V. L., Four Generations of Transition-State Analogues for Human Purine Nucleoside Phosphorylase. *Proceedings of the National Academy of Sciences of the United States of America* **2010,** *107* (11), 4805-4812.

198. Suarez, J.; Haapalainen, A. M.; Cahill, S. M.; Ho, M. C.; Yan, F.; Almo, S. C.; Schramm, V. L., Catalytic Site Conformations in Human Pnp by 19f-Nmr and Crystallography. *Chemistry & biology* **2013,** *20* (2), 212-22.

199. Ghanem, M.; Saen-Oon, S.; Zhadin, N.; Wing, C.; Cahill, S. M.; Schwartz, S. D.; Callender, R.; Schramm, V. L., Tryptophan-Free Human Pnp Reveals Catalytic Site Interactions. *Biochemistry* **2008,** *47* (10), 3202-3215.

200. Lakowicz, J. R., Quenching of Tryptophan Residues in Proteins. In *Principles of Fluorescence Spectroscopy*, 3rd edition. ed.; Springer: New York, 2006; pp 546-551.

201. Vivian, J. T.; Callis, P. R., Mechanisms of Tryptophan Fluorescence Shifts in Proteins. *Biophys J* **2001,** *80* (5), 2093-2109.

202. Eftink, M. R., Fluorescence Techniques for Studying Protein Structure. In *Methods of Biochemical Analysis*, John Wiley & Sons, Inc.: 2006; pp 127-205.

203. Beechem, J. M.; Brand, L., Time-Resolved Fluorescence of Proteins. *Annu Rev Biochem* **1985,** *54*, 43-71.